SURFACE STUDIES OF URANIUM AND ZIRCONIUM ON TUNGSTEN

by

R.A.Collins B.Sc.,Grad.Inst.P.

Department of Physics
University of Southampton

August 1968

FACULTY OF SCIENCE

PHYSICS

Doctor of Philosophy

SURFACE STUDIES OF URANIUM AND ZIRCONIUM ON TUNGSTEN

by Richard Arnold Collins

Field emission microscopy and mass spectrometry have been used to study the electronic and structural properties of submonolayer and multilayer films of uranium and zirconium evaporated in ultra-high vacuum onto tungsten. The variation in the field emission average work function has been determined during uranium adsorption,and has been studied as a function of coverage,heat treatment,pressure and degassing of the uranium.Irreversible work function changes have been observed at temperatures at which crystallographic changes occur in bulk uranium.Mass spectrometry has been employed to determine the purity of the evaporant flux and the constancy of the evaporation rate.Multilayer adsorption has indicated preferential growth regions where the bulk uranium structure can be accommodated with relatively little misfit.Measurements on zirconium adsorption have shown nucleation on the high index planes in the temperature region 500 - 1000°K and monolayer growth on the (100) planes.This is in contrast to uranium for which nucleation was not observed.Zirconium nucleation has been studied as a function of heat treatment,pressure and degassing of the zirconium source.Mass spectrometry has again been used

to determine the content of the evaporant flux. Work function measurements for both uranium and zirconium adsorption on single crystal planes have been made by the use of a probe-hole technique.Dipole moments and effective polarizabilities have been calculated for certain planes.A direct comparison has been made between the field emission work function values obtained in the present work and those obtained in this laboratory on the same adsorption system using the retarding field technique.

CONTENTS

Page No.

CHAPTER 5 THE FIELD EMISSION TECHNIQUE

5.2 Field Emission Theory

5.3 Field emission microscopy

CHAPTER 6 PROPERTIES OF URANIUM AND REVIEW OF PREVIOUS MEASUREMENTS

6.5 Previous measurements of uranium surface properties

Page No.

CHAPTER 9 RESULTS AND DISCUSSION-URANIUM

CHAPTER 10 RESULTS AND DISCUSSION-ZIRCONIUM

CHAPTER I

GENERAL INTRODUCTION

Chemisorption of electropositive elements on refractory metal substrates causes a reduction in the electronic work function due to the formation of a dipole layer. This phenomenon has been utilized for many years in thermionic devices and has led to numerous investigations of such systems in the study of adsorption mechanisms, metallic bonding and surface catalysis. Early work by de Boer[1] and others led to improved experimental techniques and added interest in adsorption and emission phenomena. Aside from the purely technological aspect of enhanced electron emission came the realisation that the work function was associated with other surface parameters and was directly relevant to studies of the electronic structure of solids, Much of the subsequent work was concerned with alkali and alkaline earth adsorbates, in particular caesium on tungsten[2] which is of direct importance in thermionic energy conversion. Other metals have also been studied, one of the earliest to be used being thorium, originally studied by Langmuir[3] and used initially in the thoriated tungsten thermionic cathode. However, whilst there is now extensive literature concerning thorium and its compounds, the other actinide elements have received less attention. Protactinium is one of the rarest of the naturally occurring elements and is therefore not available for study, and uranium, although readily available was little investigated prior to the interest in it as a nuclear fuel. In recent years, however, interest in uranium has increased for several reasons. Firstly, its properties are of some interest in view of its position as the heaviest naturally occurring element in the periodic table. Secondly, uranium and its compounds, particularly uranium carbide, have been studied with regard to their applicability as thermionic electron sources in thermionic energy converters[4,5]. Thirdly, uranium undergoes two crystallographic phase transformations and is therefore of considerable interest in surface studies of adsorption and epitaxial growth and of phase transitions in thin films.

Recent measurements of the work function of uranium on tungsten[5-10] have shown large discrepancies in the values obtained. Further, both contact potential difference[9] and photoelectric[10] measurements have indicated discontinuities in the work function/heat treatment curves for monolayer deposits of uranium on tungsten heated to progressively higher temperatures. These discontinuities occur at the bulk metal phase transition temperatures and are in direct contrast to the results for bulk uranium metal for which the phase transition effects are completely reversible.

Many of the reasons for the interest in uranium also apply to zirconium, which, although showing little correspondence with uranium in its position in the periodic table has many similar properties. In thermionic energy conversion alloys of uranium and zirconium carbides have been of considerable interest[11]. Furthermore, as with uranium, zirconium undergoes a crystallographic phase transition which is reversible in the bulk metal. The most outstanding property of zirconium is its resistance to chemical corrosion, and this had led to widespread applications in electronics, neurosurgery, getters and in various types of chemical and nuclear power equipment. Despite the importance of the chemical and physical surface properties of zirconium, however, little work has been done in this realm. Measurements of the zirconium work function and observations of the initial growth of thin films[12-16] have again shown wide discrepancies due to poor experimental conditions.

The purpose of the present work was to study the adsorption, migration and growth properties of uranium and zirconium on tungsten, using field emission and mass spectrometric techniques.

The initial work concerned the work function variation of uranium on tungsten as a function of coverage and heat treatment. On the basis of the irreversible work function changes observed on heating monolayer deposits to the phase transition temperatures Barry et al[9] had proposed a tentative adsorption model involving the formation of a discontinuous island structure in which the bulk uranium properties prevailed. The present work was started to confirm these work function changes and to observe the adsorption of uranium using field emission microscopy.

The field emission microscope is well suited to measurements of this type. Adsorbates may be deposited in ultra-high vacuum onto atomically smooth defect-free clean tungsten substrates.

Adsorption and nucleation sites can be readily identified and surface migration kinetics observed. Further, the effects of both temperature and residual gases may be examined over a wide range of temperature and pressure.

The initial work on uranium was extended by observing the work function and growth kinetics up to coverages of about 12 monolayers. The effects of hydrogen contamination were also investigated. Subsequent experiments employed a current probe to examine similar properties of the individual crystal planes of the emitter.

Similar measurements were made for zirconium on tungsten up to coverages of about 2 monolayers and various aspects of the nucleation properties were also studied.

For both uranium and zirconium mass spectrometric analyses were made of the residual gases in the experimental tubes at all stages of experimentation. The content of the evaporant fluxes from the evaporation sources were examined to determine impurity content. The constancy of the evaporation rate from these sources was also observed.

A comparison has also been made of the work function values derived from the field emission measurements with those determined using macroscopic methods, field emission work function values being calculated using a least-squares fit method programmed in ALGOL.

CHAPTER 2

THE WORK FUNCTION AND ASSOCIATED SURFACE PROPERTIES

2.1 Introduction

The concept of the electronic work function emerged more than fifty years ago with the work of Richardson and Langmuir. The term 'work function' was first used in its present sense by Lester[17] in 1916. Since then much experimental work has been carried out to determine the work functions of a wide range of substances[18]. However, as a result of the experimental difficulties encountered in preparing reproducible well-defined clean surfaces, only a few metals have well established work functions. The best known is tungsten[19] which has been extensively studied in the form of polycrystalline foil and as single crystals, and also, as in the present work, as the emitter substrate in field emission measurements.

2.2 The Electron Work Function

According to the Sommerfeld free electron theory the electrical conductivity of a metal is largely due to the conduction electrons which are free to move through the crystal lattice. The ion cores (non-conduction electrons and nuclei) may be approximated to by a smoothed out background positive charge. The conduction electrons may then be considered as lying in a potential well of depth W. The observation that electrons do not escape from the metal at room temperature led to the suggestion of a surface potential barrier at the surface, the well depth rising to zero, as shown in fig. 1.

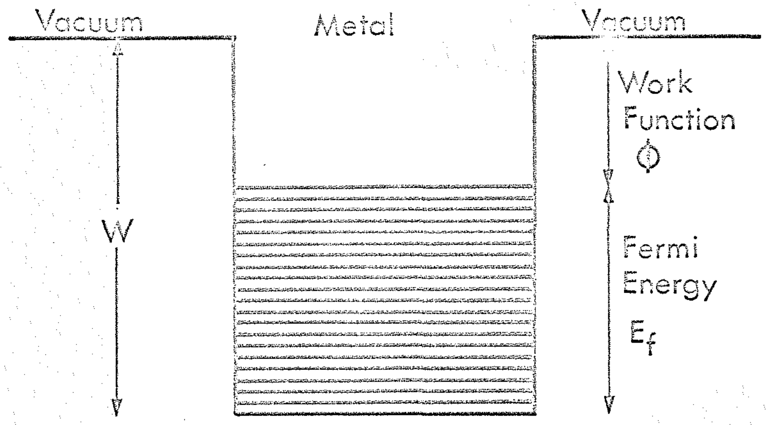

Fig. 1 The Sommerfeld Metal.

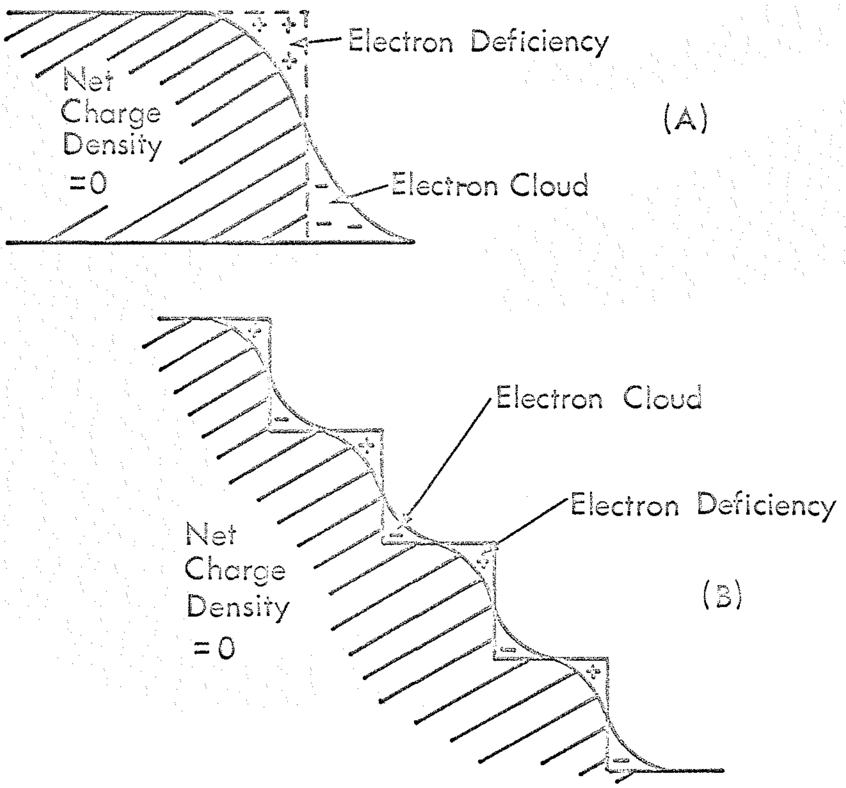

Fig. 2 Schematic charge distribution at a metal surface for (A) atomically smooth surface and (B) an atomically stepped surface.

This surface barrier has generally been attributed to the formation of a surface dipole layer arising from the unsymmetrical electronic charge distribution at the discontinuity in lattice structure at the surface. This double layer is discussed in section 2.4 and is shown in fig. 2A. The potential step across the surface double layer is given by

$$V = \frac{M_t}{\varepsilon_o} \qquad (1)$$

where M_t is the total dipole moment per unit area and ε_o is the permittivity of free space.

Herring and Nichols[20] defined the work function ϕ as the energy difference between the Fermi level E_F inside the conductor and the energy of an electron at rest just outside the metal. Thus, from fig. 1

$$\phi = W - E_F \text{ electron volts} \qquad (2)$$

An alternative definition of the work function arises from consideration of the Fermi-Dirac distribution function

$$f(E) = (1 + \exp\left[(E - E_F)/ KT \right])^{-1} \qquad (3)$$

where f(E) is the probability that a state of energy E will be filled at temperature T^oK. It is seen that at 0^oK the electrons occupy the lowest possible energy states. Thus the work function may be defined as the difference in energy of a lattice formed from equal numbers of electrons and ion cores at 0^oK and the same lattice with one electron removed.

The work function may also be defined from thermodynamic considerations of the electrochemical potential $\bar{\mu}$ [20,21]. Thus, for an isolated body, volume V', containing n electrons,

$$\bar{\mu} = \left(\frac{\delta F}{\delta n}\right)_{T,V'} \qquad (4)$$

where F is the Helmholtz free energy of the system at temperature T. F is defined by F = U - TS, U being the total internal energy of the system, and S its entropy. Thus, $\bar{\mu}$ is equivalent to the work done in bringing an electron from infinity and adding it isothermally to the system. Suppose now we have a system of several gaseous or solid phases in equilibrium. Then for the i th phase, containing n_i electrons,

$$\bar{\mu}_i = (\delta F'/\delta n_i)_{T,V,n_{k \neq i}} \qquad (5)$$

where $F' = U - \sum T_k S_k$ and n_k is the number of electrons in the other phases. Now, for a body to which electrons are added, the electrostatic potential V_E will change by ΔV_E resulting in a change in $\bar{\mu}$ of $-e\,\Delta V_E$. Also, as the electrostatic potential inside a conductor can be varied by moving external charges, then $\bar{\mu}$ will depend not only on the internal state, but also on the surface and external conditions. It is therefore convenient to define[20] the chemical potential μ by

$$\mu = \bar{\mu} + e\,V_{E\ \text{inner}} \qquad (6)$$

where $V_{E\ \text{inner}}$ is the electrostatic potential (in volts) inside the body, and e = 1 electron volt/volt. μ is thus a function of the internal state only, and is independent of external and surface conditions. The work function is defined as the difference between the electrochemical potential energy of an electron in the conductor and its electrostatic potential energy $-e\ V_{E\ \text{outer}}$ at a point just outside the surface (at a distance of about 10^{-4}cm where it is regarded as out of range of significant surface interactions).

$$\phi = -e\ V_{E\ \text{outer}} - \bar{\mu} = e\ V_{E\ \text{inner}} - e\ V_{E\ \text{outer}} - \mu \qquad (7)$$

Thus the work function comprises an 'inner work function' μ, and a surface potential X_{sp} given by

$$X_{sp} = e\ V_{E\ \text{outer}} - e\ V_{E\ \text{inner}} \qquad (8)$$

Now $-e\ V_{E\ \text{inner}}$ is clearly equal to W in fig. 1 and if $e\ V_{E\ \text{outer}} = 0$, then

$$\phi = W - \mu \qquad (9)$$

Now it can be shown[21,22] that $\mu = E_F$, whence

$$\phi = W - E_F$$

in agreement with equation (2). Thus the definitions of work function are consistent.

2.3 Contact Potential Difference

A quantity closely related to the work function is the Volta potential or contact potential difference. If two isolated electrically neutral conductors A and B have electrochemical potentials $\bar{\mu}_A$ and $\bar{\mu}_B$ and are placed in contact, then $\bar{\mu}_A$ and $\bar{\mu}_B$ change in value so that $\bar{\mu}_A = \bar{\mu}_B$ at equilibrium. This is brought about by a transfer of electrons from the conductor with the higher electrochemical potential until $(V_{E_A} - V_{E_B})_{\text{outer}}$ is equal to the initial difference $\mu_A - \mu_B$, μ being independent of electron density variations. Then, from equation (7) the potential difference V_{AB}, equal to $(V_{E_A} - V_{E_B})_{\text{outer}}$ which appears between points just outside the surfaces of the conductors is

$$V_{AB} = (V_{E_A} - V_{E_B})_{\text{outer}} = \phi_B - \phi_A \qquad (10)$$

i.e. the contact potential difference is equal to the difference in the two work functions.

2.4 Anisotropy in the Work Function

As mentioned in section 2.2 a contribution to the work function arises due to electrostatic effects at the surface. These effects vary with surface structure and result in a crystallographic anisotropy in the work function. The first quantitative evidence of this effect came from field emission[23] and thermionic emission microscope[24] experiments. In both cases, emitted electron distribution patterns dependent upon the crystallographic symmetry of the emitter were obtained as a result of the variation in emission intensity with surface structure. Since then much work on single crystal surfaces has been done using field emitters and macroscopic single crystals[18].

Smoluchowski[25] attempted a quantitative explanation of this effect by consideration of the double layer effects at the surface. Suppose that a metal has a clean planar surface. The electron cloud will not terminate abruptly at the surface as this would correspond to an infinite gradient of the wave function. Instead there will be a gradual decay causing an electron deficiency on the metal side of the interface as shown in fig. 2a. This gives rise to a double layer with the negative end outwards, effectively forming a parallel-plate capacitor, the potential of which is included in the work function. Furthermore, for an atomically rough surface a second type of overspill occurs. This consists of a smoothing of the electron cloud as electrons flow from the 'hills' into the 'valleys', as in fig. 2b. The double layer produced has its positive end outwards. It is therefore to be expected that atomically close-packed (smooth) crystal faces will have high work functions and loosely-packed planes low work functions.

Smoluchowski calculated expressions for the smoothing out of the electron clouds for body-centred cubic low index planes. Reductions in work function are given by

$$V_{(hkl)} = \frac{n'}{b'} K_{(hkl)} \text{ eV} \qquad (11)$$

where n' is the number of electrons per unit cell of the lattice, b' is the lattice parameter measured in atomic units and $K_{(hkl)}$ has values 1.3, 4.1, 4.22 and 8.15 for the (110), (112), (100) and (111) planes respectively. Comparing his values with the then available experimental values[26] Smoluchowski found good agreement for the predicted order of work function values (110) > (112) > (100) > (111). However, agreement between the absolute values could only be obtained by assuming an electron density of only a fraction of an electron per unit cell, rather than the two per cell as he had previously assumed. Also, as Smoluchowski pointed out, his calculations were only approximate as he had assumed a uniform electronic charge distribution i.e. the ion cores were assumed to be small. This is a good approximation for sodium for example, but not for tungsten.

2.5 Correlation of work function with other physical quantities

Attempts to predict work functions by indirect means have resulted in the search for correlations with other physical properties. Langmuir[27] observed a correspondence between thermionic work function and electrode potential for nine metals. Later, Rother and Bomke[28] examined the relationship between work function, atomic weight, valence and density. Other correlations were also made with ionization energy[29], lattice energy[30] and reciprocal atomic volume[31]. The relationship between work function, atomic number and ionization potential has been given by Michaelson[32] and is shown in fig. 3.

Hermann and Wagener[33] deduced an approximate relationship between work function and reciprocal lattice spacing d_e^{-1}, thus,

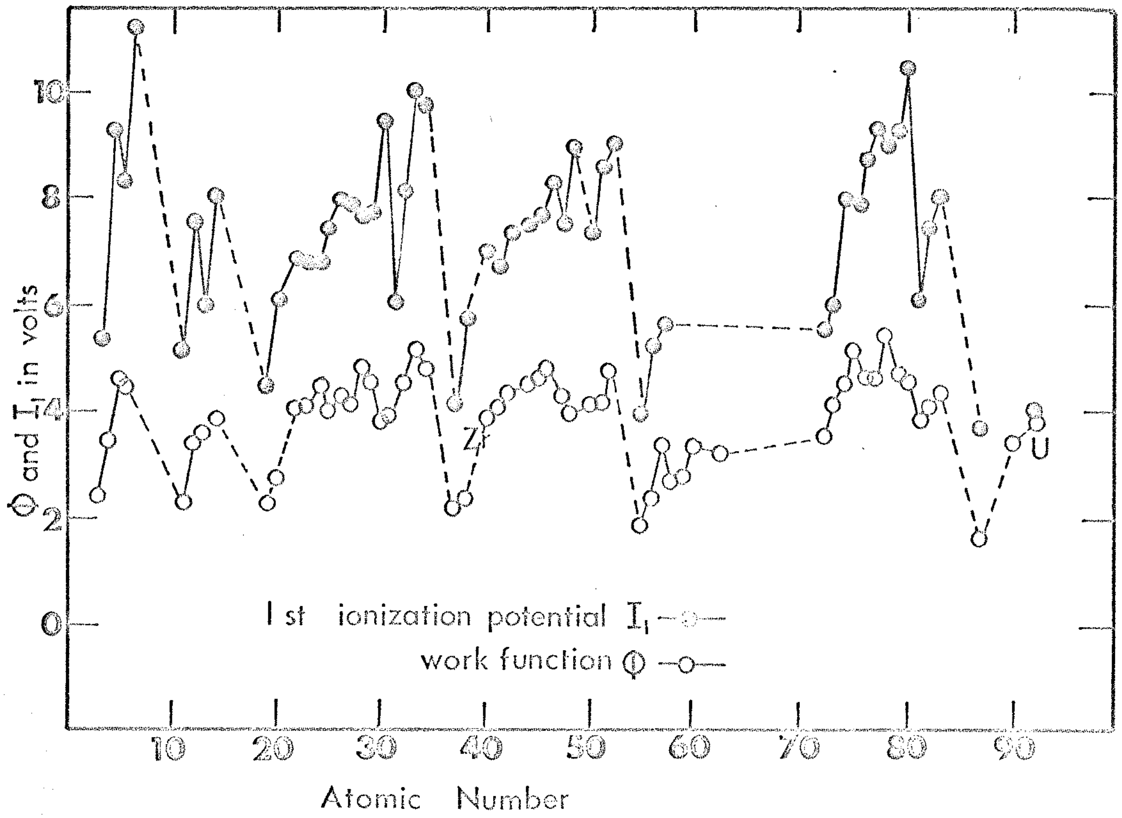

Fig. 3 Variation of work function and first ionization potential with atomic number.

$$\phi = 7.2 \times 10^{-8} d_e^{-1} \text{ eV} \qquad (12)$$

This relationship is **partially** satisfactory for the alkali metals only.

Sachtler[34] showed that for most metals crystallizing in bcc, fcc or hcp form the following relationship holds,

$$\phi = 2.47 I_1\delta + 1.58 \qquad (13)$$

where I_1 is the first ionization potential and δ the surface density of atoms on the most stable face. Deviations are generally within ± 0.1 eV. Sachtler used this expression to derive the work function of Sc, La, Y and Nd and the ionization potentials of Ir, Th, Nb, Ta, Hf and Re.

Using Michaelson's work function values, Gordy and Thomas[35] plotted electronegativity X_N against work function as shown in fig.4. They found the relation

$$X_N = 0.44 \phi - 0.15 \qquad (14)$$

Also shown in fig. 4 is their graph of electronegativity (and hence work function) against atomic number.

Varley[36] has made a semi-empirical estimate of the Fermi energy of the free electrons in a metal, calculated from the free electron band width, the heat of sublimation and the ionization energy, and has shown an approximate correlation with the work function for a number of metals. He predicted that the work function should be of the order of 0.5 of the Fermi energy. His results show this to be approximately true for a number of elements.

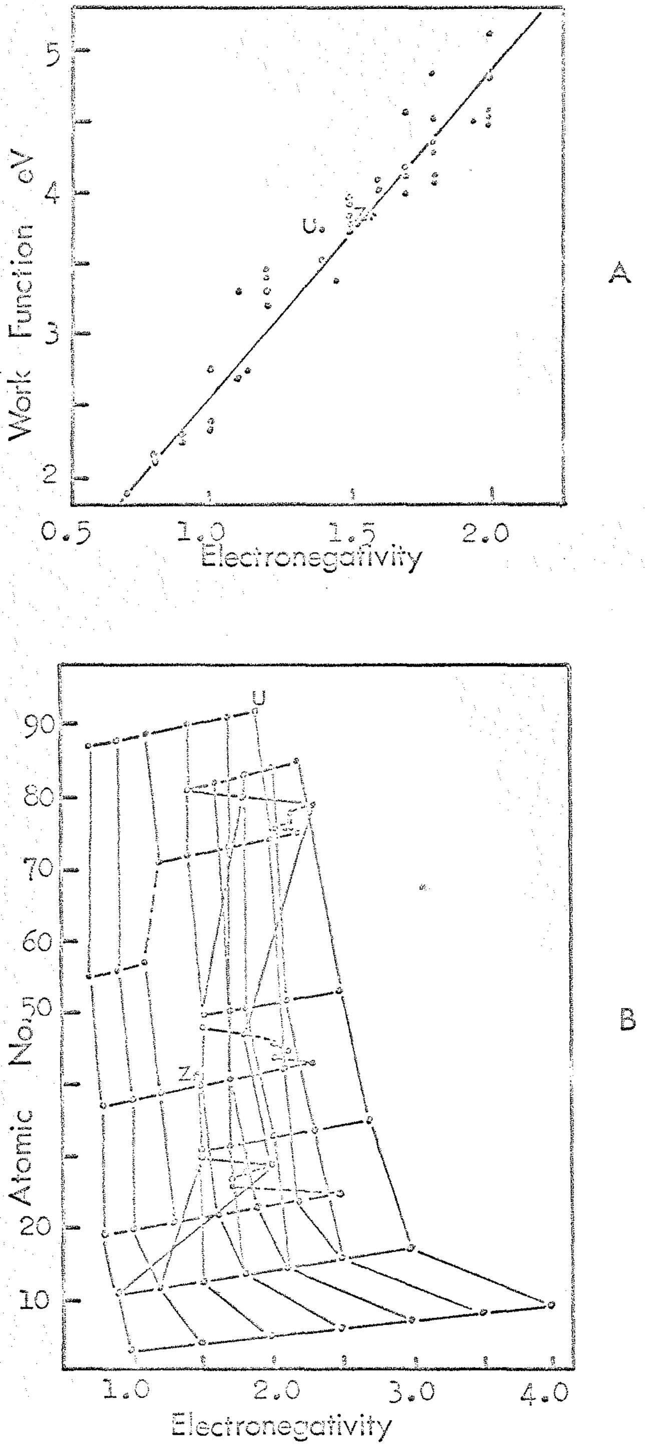

Fig. 4 Relationship between work function and (A)electronegativity and (B)atomic number.

The most significant feature of these correlations is that whilst the work function is basically a surface property, there is a close relationship with the properties of the bulk metal.

2.6 Theoretical predictions of the work function

The first quantum mechanical calculations of the work function of a metal were carried out by Wigner and Bardeen[37]. By calculating the energy of a lattice of n_i and n_e electrons they obtained a formula for the work function of monovalent metals in terms of the heats of sublimation. This formula was very approximate as the surface double layer had been ignored. Bardeen[38] subsequently improved this model by including a term to represent the energy required to transverse the electrostatic double layer. The charge distribution at the surface was calculated using the Hartree-Fock self-consistent field method. The expression was further extended to include the effect of correlation forces on the double layer. Comparison of this theory with the experimental value for sodium showed a good agreement. Bardeen concluded that the surface barrier is due primarily to exchange and correlation forces, and that ordinary electrostatic forces play a minor role.

The general features of the Bardeen theory were verified by Juretschke[39] and were refined by Loucks and Cutler[40], who used the Bohm-Pines formalism to take approximate account of Coulomb correlations in a recalculation of the exchange part of the surface potential.

Recently, Bardeen[41] has estimated the work function of a metal by utilising Ziman's pseudo-potential method of evaluating the metal electronic structure. This essentially involves calculating the electronic wave functions as plane waves moving in a constant potential, and then taking the effect of the ion cores into account as a weak pseudo-potential. Bardeen obtained

$$\phi = 13.6 \left[\frac{-3.68}{r_s^2} + \frac{1.22}{r_s} + \frac{0.59r_s + 6.9}{(r_s + 7.8)^2} - \langle V_{ps} \rangle + eD \right] eV \qquad (15)$$

The terms in the expression represent, in order, the kinetic energy, exchange energy, correlation energy, average pseudo-potential, and the potential of the surface double layer relative to a point just outside the surface. To calculate the work function values it is necessary to calculate the V_p's for each metal and eD for each crystal plane

Leivo et al[43] have extended an expression originally given by Seitz[44] to obtain the following expression

$$\phi = \frac{1}{Z} \left[E_c + I(Z) \right] + \left(- \frac{2}{3} E_F - 0.6\frac{e^2}{r_{sp}} + \frac{0.458e^2}{3r_{sp}} + \frac{r_{sp}g^1(r_{sp})}{3} - 4\pi ePn \right) \qquad (16)$$

where Z is the number of valence electrons per atom, E_c is the cohesive energy per atom, I(Z) is the ionization potential of the free atom, r_{sp} is the radius of the sphere replacing the unit cell in the calculation, the second term in brackets is the Coulomb energy, the third term is the exchange energy and the fourth term the correlation energy for the uppermost electron in the filled band. $4\pi ePn$ is the surface dipole term.

This equation demonstrates the dependence of work function on cohesive energy. Close agreement between the observed values of ϕ for some metals with one valence electron and the computed values of $\phi + 4\pi ePn$ shows that the surface dipole moment is very small for clean metal surfaces in these cases[43].

2.7 Effects of adsorbates on the work function

It has been shown that the work function is a surface dependent property, and will therefore be affected by the presence of adsorbed atoms or ions on the surface.

A free atom approaching a metal surface experiences a perturbation of the discrete energies of its outer electrons. In order to determine the effects of the subsequent adsorption process, we must firstly consider the electronic interactions between the adsorbing atom and surface. Described below are the three limiting cases for the possible adsorbate-substrate interactions.

(i) Physisorption

If the outer electron shell of the adatom is filled, then there will be no electron exchange between adatom and substrate. The binding forces will then be of the van der Waals type. These forces are of three types, those depending on orienting electric dipoles (the directional effect), on electrostatic induction (resulting in polarization of the adsorbate), and on the interaction between transient dipoles. These forces have been described by Kaminsky[45]. They are of fairly long range, but only weakly attractive, physisorption being non-specific with regard to substrate. In general adsorption energies are only slightly higher than the corresponding heats of liquefaction, hence appreciable physisorption only occurs in the temperature-pressure range near condensation. Multiply adsorbed layers may be formed reversibly. Adsorption isotherms generally show an inflexion point followed by a steep rise. Brunauer, Emmett and Teller[46] explain this in terms of the inflexion corresponding to the completion of the first layer. Further rise is due to build-up of successive layers and finally liquefaction. Fig. 5 shows the dipole length for a physisorbed adatom and the potential energy diagram for an atom such as helium approaching a metal surface. The heat of adsorption is shown by $-\Delta Hp$.

(ii) Covalent Chemisorption (Homopolar bonding)

A covalent bond is formed when exchange forces between the adatom and the substrate result in the sharing of electrons to produce

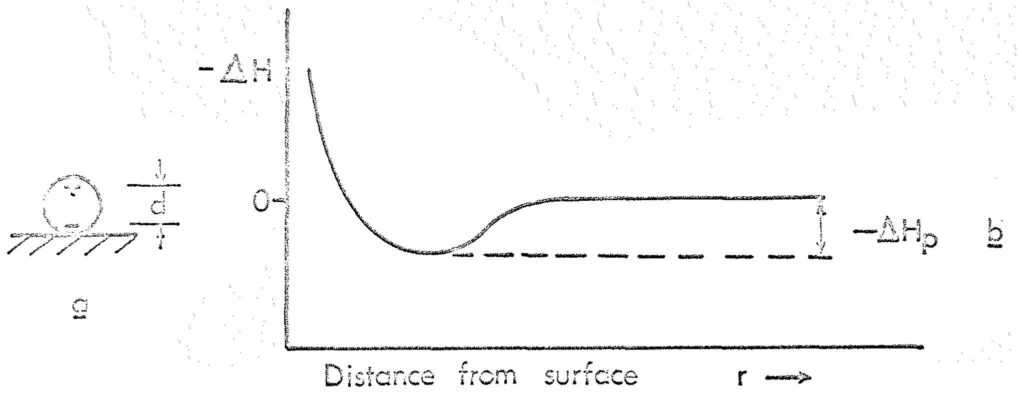

Fig. 5 Physisorption. (a) Dipole length (b) Potential energy curve.

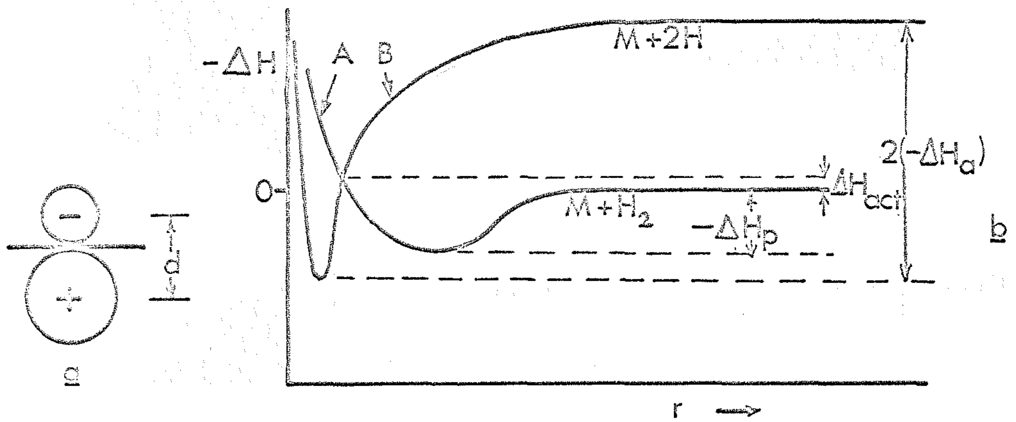

Fig. 6 Covalent chemisorption. (a) Dipole length (b) Potential energy curves.

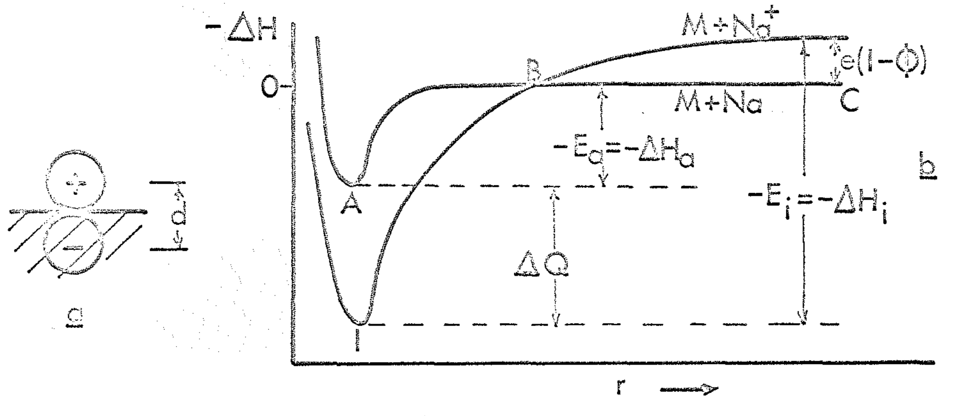

Fig. 7 Ionic bonding. (a) Dipole length (b) Potential energy curve.

a stable configuration. Fig. 6a shows the dipole length for such an interaction. Fig. 6B shows the potential energy curve for the interaction of a hydrogen molecule with a metal surface as illustration of covalent bonding. In curve A the hydrogen molecule is physically adsorbed with heat of adsorption ΔHp. In curve B the molecule, after acquiring an activation energy ΔH_{act}, can dissociate into two H atoms prior to chemisorption. The difference ΔHa is the heat of chemisorption for the hydrogen atom.

In general, chemisorption is more specific than physisorption with regard to the substrate. Adsorption energies vary from one to several electron volts. Chemisorption does not occur beyond the second adsorbed layer.

(iii) Ionic Bonding (Heteropolar forces)

Whereas covalent forces involve only interpenetration of the electron shells of the metal and adatom, heteropolar binding forces are associated with electron transfer from the adatom to the metal or vice versa. Fig. 7a shows the dipole length for ionic bonding and fig. 7b the potential energy diagram for the adsorption of sodium atoms and ions on a metal surface. A sodium atom approaching the surface will traverse the curve CBI, and will be adsorbed as an ion, since the potential energy minimum on the 'ionic curve' is below that on the 'atomic curve'. Ionic heats of adsorption are larger than for covalent bonding or physisorption. For electron transfer from adatom to metal we must have

$$e\phi > eI \qquad (17)$$

where I is the ionization potential of the adatom. However, for adsorbing ions the relation becomes

$$E_i + e\phi > eI + E_a \qquad (18)$$

where E_i and E_a are the adsorption energies of the adatom in ionic and atomic form respectively.

It is clear that each type of binding results in a modification of the inherent dipole structure of the surface, and hence gives rise to a change in the work function. It should be noted however, that the above types of binding represent only the limiting cases of the electronic interactions which occur in practice. It has been pointed out by Pauling[47] that a resonance or continuous interchange can occur between the different states of adsorption. The situation is further complicated by the interactions between the individual surface dipoles as the surface coverage increases. Thus, prediction of the effects of adsorbates on the work function requires certain assumptions:-

(a) The type of adatom-substrate electronic interactions involved.

(b) The density of the atoms at the surface must be known.

(c) The location and types of adsorption site must be known.

(d) The effects of the mutual dipole interactions must be estimated.

A further point remains to be made. Use of equations (17) and (18) to determine the state of binding for metallic atoms is inadequate. Gurney[48] showed that as an atom approaches the surface of a metal energy levels in the atom corresponding to allowed energy levels in the metal become broadened. This may be explained as follows. If electron resonance can occur between the atomic and metallic states then neither state is a stationary state of the system. As a consequence of the uncertainty principle, the finite lifetime results in a broadening of the originally discrete level. Note that none of the levels concerned need to be occupied; what is implied is that if one of the states is occupied then it has a finite bandwidth. Furthermore, as the adatom interacts with the substrate, the metallic energy level is perturbed and shifts relative to the Fermi level[49]. The amount that the shifted and broadened level overlaps the conduction band determines the form of the bonding. This is shown in fig. 8 for three cases of chemisorptive broadening. In fig. 8a the broadened level lies entirely below the Fermi level. For a metallic adsorbate the conduction electrons will spread around the ion cores and the bonding will become metallic. For an electronegative adsorbate, such as chlorine, the broadened level would be the lowest unoccupied level, and an electron would be transferred to the adsorbate forming a negative ion. Fig. 8c shows the broadened level completely above the Fermi level, a

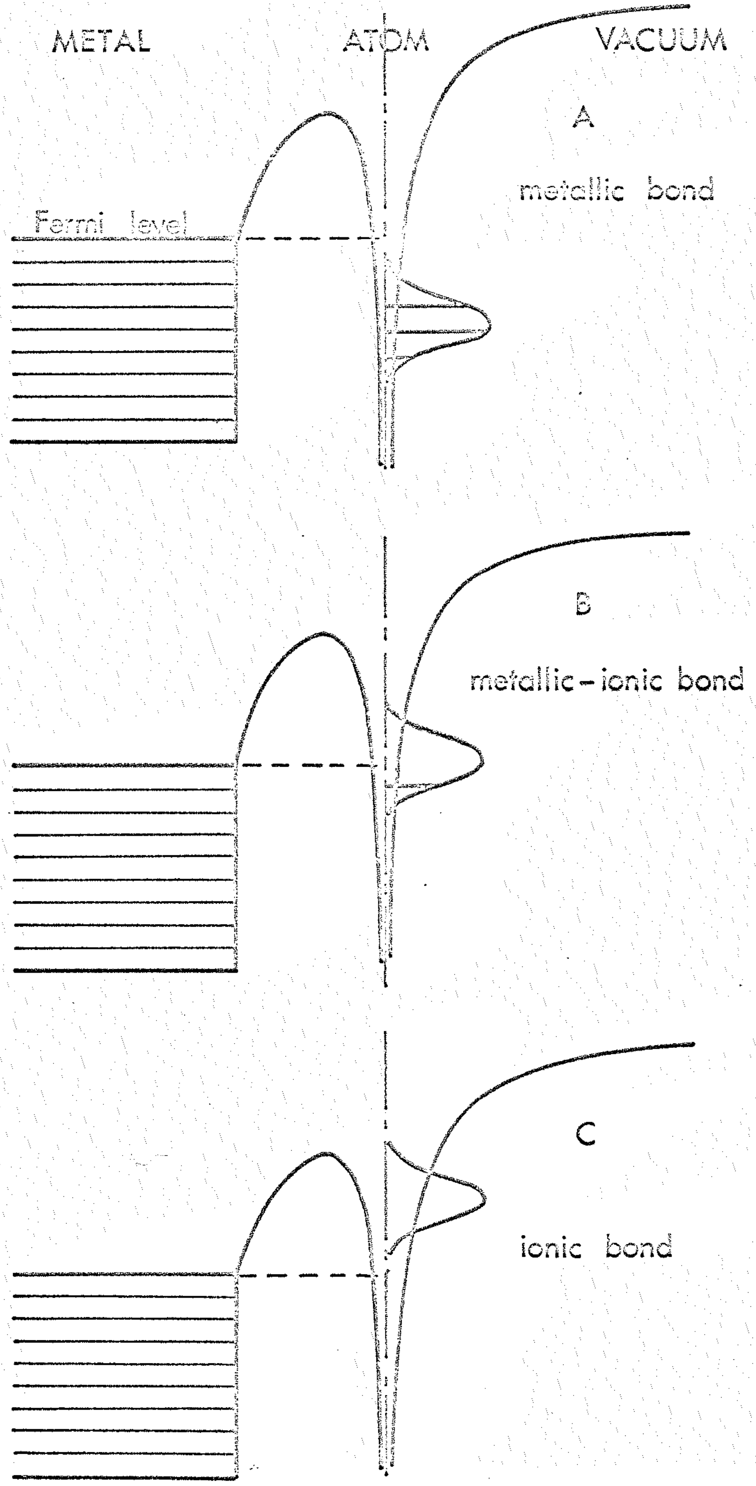

Fig. 8 Three cases of the metal-atom interaction.

metal adatom in this case being adsorbed as a positive ion. The intermediate case (fig. 8b) has part of the broadened and shifted level above the Fermi level and part below. In this case the bond is partly covalent, partly ionic. The importance of this shift and broadening of the valence level makes it necessary for these parameters to be accurately known if any prediction concerning the bonding is to be made.

2.8 Adsorption effects - Theoretical Predictions

Attempts to evaluate the effects of adsorbed layers on the work function have generally been based on considerations of the surface dipoles. Early predictions ignored dipole-dipole interactions. Thus, if a metal surface contains $N = \theta N_t$ adsorbed atoms per sq. cm. where N_t is the total number of sites available and θ is the fraction filled, then a dipole layer will exist in the surface. Then, the work function change, dependent upon the sense of the dipole layer is given[50] by

$$\Delta\phi = \pm \frac{N_t \theta M}{\varepsilon o} \qquad (19)$$

where M is the dipole moment per dipole.

Early measurements by Becker[51], Langmuir et al[52] and others[53] did not show this linear dependence of ϕ on θ at coverages > 0.2. De Boer[1] subsequently interpreted Langmuir's results for caesium on tungsten as indicating initial adsorption as ions followed by adsorption as polarized atoms. The atomic adatoms were assumed to be polarized to form dipoles of the opposite sense to the ionic dipole layer, resulting in the final rise in work function observed by Langmuir.

Measurements of hydrogen and nitrogen adsorption on tungsten by Bosworth[54] indicated a linear dependence of $\emptyset$ on θ up to $\theta = 0.7$, but for oxygen on tungsten departure from linearity occurred at about $\theta = 0.5$. Comparison with alkali metal adsorption indicated that the dipole interaction is less significant for gaseous adsorption.

Equation (19) was extended by Miller[55] by applying Toppings[56] calculations on the mutual depolarization of surface dipoles. For a plane array of dipoles he obtained

$$\Delta \emptyset = \pm \frac{eMN_t(\theta/\varepsilon_o)}{1 + \frac{9\alpha\theta}{4\pi a^3 \varepsilon_o}} \qquad (20)$$

where α is the polarizability of the adsorbate and a is the dipole separation at $\theta = 1$. Thus, Bosworth's results showing linearity for hydrogen and nitrogen were probably due to these low α values for these gases.

According to Boudart[57] equation (20) is applicable for Langmuir's Cs on W results for $\theta < 0.4$. However, this model is still not satisfactory at higher coverages. Boudart also suggested that the hydrogen-metal bond is essentially metallic in nature, of the resonating Pauling type. That is, it is essentially covalent but with a certain degree of ionicity dependent upon the relative electronegativities of hydrogen and the metal. He also suggested that oxygen-tungsten bonding was partly covalent and partly ionic, and that the dipole interaction should be greater for oxygen than for hydrogen on tungsten because of the greater polarizability of the oxygen.

A different expression for the variation of work function with coverage was obtained by Sachtler et al[58] by adopting the Pauling model of the homopolar bond. Their wave mechanical treatment yielded the expression

$$\Delta\phi = \pm \frac{(300 \times 10^{-18})}{3.15\,\varepsilon_o} N_t\, \theta\, e\, (\phi - X) \qquad (21)$$

where X is the absolute electronegativity of the adsorbate defined[59] as the arithmetic mean of the ionization potential and the electron affinity of the adsorbed material. However, whilst this equation gives the correct sign for the work function change quantitative agreement is not obtained.

An expression similar to (20) was obtained by Higuchi et al[60] by application of the laws of electrodynamics:-

$$\Delta\phi = \pm \frac{e\, N_t\, d\theta}{\left(\varepsilon_o + \frac{N_t \alpha\theta}{d}\right)} \qquad (22)$$

where d is the bond dipole length. Fitting this equation to the experimental results for K, C_s, Na and Ba on W gives a good fit for $\theta \lesssim 0.6$, from which Higuchi et al were able to deduce θ and α (for C_s on W). This allowed them to distinguish between the types of bonding occurring in the various systems. However, whilst their quantum mechanical treatment was applicable to all types of bonding, agreement with experiment was still very poor at higher coverage.

Recent theories have proved more successful in this respect. Gyftopoulos and Levine[61] realised that at higher coverages the adatom wave functions would overlap producing an electronic band structure. At present, wave mechanical methods are inadequate to evaluate this structure. They therefore utilized a phenomenological model whereby the work functions at zero and monolayer coverage are related directly to the electronegativities of the substrate and adsorbate respectively. The work function is then considered as the sum of two θ-dependent terms:

$$\phi(\theta) = e(\theta) + d(\theta) \tag{23}$$

where $d(\theta)$ includes the classical dipole function and $e(\theta)$ is the electronegativity component. Further, $e(\theta) \to 0$ as $\theta \to 0$ and $d(\theta) \to 0$ as $\theta \to 1$. By applying the experimentally observed boundary conditions

$$\left(\frac{de(\theta)}{d\theta}\right)_{\theta = 0,1} = 0 \tag{24}$$

and $\phi_{\theta=1} = \phi$ adsorbate, and using the Pauling-Malone relationship[62] between electronegativity and dipole moment, the following expression was obtained:-

$$\Delta\phi = (\phi_m - \phi_f)\left\{1 - G(\theta)\left[1 - \frac{0.765 \times 10^{-18}\delta_F \theta \cos\beta}{\left(1 + \frac{\alpha}{4\pi\varepsilon_o R^3}\right)\left(1 + \frac{9\alpha\delta_F^{3/2}\theta^{3/2}}{4\pi\varepsilon_o}\right)}\right]\right\} \quad (25)$$

where $G(\theta)$ is the simplest polynominal chosen to fit the boundary conditions, ϕ_m is the metal substrate work function, ϕ_f is the final work function and R and β are geometrical factors. The polarizability X is obtained from the approximate formula

$$\alpha = 4\pi\varepsilon_o n r_f^3 \quad (26)$$

where r_f is the covalent radius and n is a number to account for the electronic shell structure effects on polarizability.

Excellent agreement has been obtained with equation (25) for several systems, in particular caesium and strontium on tungsten[2]. The main weakness of the theory appears to be the arbitrary choice of the polynomial $G(\theta)$. It should be pointed out however, that the choice of this polynomial does not greatly affect the shape of the theoretical curve.

The boundary condition requirements of the theory of Gyftopoulos and Levine preclude its use for cases of gaseous adsorption on metal substrates. The shape of the $\phi - \theta$ curves for the adsorption of

CO, N_2, H_2 and O_2 as measured by Eisinger[63-66] have been considered by Crowell and Norberg[67]. They extended equation (19) to include adsorption at two types of adsorption site, as on the (113) face of tungsten[66]. According to their model, if two types of adsorption site exist on the surface, denoted by A and B, and there are N_s sites of each type, then if N_A and N_B are the numbers of adatoms in each type of site the work function change is given by

$$\Delta\emptyset = \frac{N_s}{\varepsilon_o} (\pm M_A\theta_A \pm M_B\theta_B) \tag{27}$$

where

$$\theta_A = \frac{N_A}{N_S} \quad \text{and} \quad \theta_B = \frac{N_B}{N_s}$$

and M_A and M_B are the dipole moments produced by adatoms in sites A and B respectively. By assuming that the adsorption on each type of site simultaneously follows a Langmuir isotherm the equilibrium pressure is given by

$$p = \frac{\theta_A}{b_A(1 - \theta_A)} = \frac{\theta_B}{b_B(1 - \theta_B)} \tag{28}$$

where b_A and b_B are the adsorption coefficients for sites A and B respectively. By combining equations (27) and (28) good agreement was obtained with Eisingers data for CO and N_2 on the W (113) planes. Crowell and Norbergs theory is somewhat questionable in view of their use of an equilibrium model with results based on flash filament data. Further, whilst a good fit with experimental data is obtained it is only by manipulation of three experimentally inexact constants.

Criticism of the Gyftopoulos and Levine theory has come from Rasor and Warner[68] who have derived an expression for the adsorption of alkali metals on metallic substrates. Their equation contains only terms related to physical quantities which can be calculated for certain systems. Included is a temperature-dependent term. The work function change is again attributed to a dipole layer, the dipoles being formed by ionic and atomic adsorbates. By considering the relative probabilities of atomic and ionic adsorption on approaching monolayer coverage they obtain:

$$\Delta\phi = \pm \frac{e^2\delta \left(1 - \left[\alpha_i (1 - f)/2e^2 r_i\right] \Delta\phi\right)\theta}{\varepsilon_o \left(1 + q \exp\left(-E/KT\right)\right)} \left(1 + \frac{M_a \theta_a}{M_i \theta_i} \right) \qquad (29)$$

The subscripts a and i refer to atomic and ionic values respectively, and f is the fraction of the dipole potential difference penetrated by the nucleus of the adsorbed ion. q and E are given by the following, relating the probability of ionic or atomic states occurring:

$$\theta_a/\phi_i = q \exp\left(-E/KT\right) \qquad (30)$$

E is the mean energy difference between the atomic and ionic states at the surface.

A good fit with equation (29) is obtained for C_s on Nb, W, Ta, Re and Ir for coverages up to $\theta = 0.8$. At the present time, however, insufficient experimental data is available to rigorously test the theory.

The most recent treatment of the work function change during adsorption is that of Macdonald and Barlow[69]. Their treatment includes the effects of a non-zero average adsorbent surface charge, orientable permanent dipoles, induced and image dipoles and effects of interactions in the plane between discrete adsorbed elements. The most significant feature of their calculations is the use of a depolarizing field, E_d, comprising five separate additive components, thus

$$E_d = \sum_{i=1}^{5} E_{d_i} \qquad (31)$$

The first contributions arise from the image charge E_{d_1} and image dipoles E_{d_2} of a single removed adion. Next comes the contribution from all the other surrounding, real induced and permanent (ideal) dipoles, E_{d_3}. The field terms E_{d_4} and E_{d_5} arise, respectively, from all surrounding nonideal dipoles formed by the adion charges and their images, and from the images of all surrounding ideal dipoles.

This treatment, although based on a crude model, is the most sophisticated yet in including the effects of the many depolarization interactions. However, agreement with experiment is poor for coverages > 0.6 when fitted to the results of Taylor and Langmuir[52] for C_s on W, and Schmidt and Gomer[70] for potassium on tungsten.

It should be pointed out at this stage that theories such as those of Gyftopoulos and Levine are not generally applicable to field emission measurements. With regard to average emitter work function measurements the patch surface with a work function weighted towards the highly emitting planes is not consistent with the assumptions in the above theories. Probe-hole techniques allowing measurements to be made on individual crystal planes are more suitable, but here again the assumptions regarding depolarization require considerable modification. This is due to the fact, pointed out by Jones[71], that field emission work functions are heavily weighted in favour of regions which ion microscopy show to be so rough that the surface dipoles can hardly be considered as coplanar.

A number of simple theoretical models have been put forward by Gomer and co-workers[70, 72, 73] in an attempt to explain experimental results for the specific systems studied. In particular, Schmidt and Gomer[73] have found good agreement between their measurements of the adsorption of potassium on individual planes of a tungsten field emitter, and a simple depolarization (Topping[56]) model applicable to alkali metal adsorption. Gomer and Swanson[72] have presented a generalized model of chemisorption on metals in a discussion of field desorption. However, whilst these models are applicable to the particular adsorption systems discussed by the authors, they have not, as yet, proved to be of general application.

CHAPTER 3

Adsorption, Migration and Growth on Solid Surfaces

3.1 Introduction

The initial problems in this study of uranium and zirconium on tungsten were essentially to determine the variations in the work function with coverage, and heat treatment and to explain the changes taking place on the surface at the phase transformation temperatures. A further problem was the difference in work functions found for uranium on tungsten between measurements using deposits of a few monolayers[9,10] and several hundred monolayers[8]. At the outset, this variation with coverage could possibly be explained in terms of the adsorption mechanisms prevailing and the subsequent growth or recrystallization resulting in changes in the surface structure with increasing deposit thickness. Further, a possible explanation for the surface 'phase transformations' was that gross thermal migration and rearrangement of the adsorbate was taking place, possibly involving nucleation or growth. In any event such changes would vary with, and be dependent upon, the surface structure of the substrate. It was therefore logical to use field emission microscopy to examine these systems. Specificity of adsorption sites, the kinetics of surface migration, nucleation and in some respects epitaxial or crystal growth could all be observed. Furthermore, work function measurements could be easily made.

As will be described in subsequent chapters nucleation, migration and growth were all observed at different stages during the work, and it is therefore pertinent to consider briefly the theories and experimental results previously determined for adsorption and growth mechanisms on solid surfaces in ultra-high vacuum. Particular emphasis is given to field emission measurements.

3.2 Adsorption and surface migration

The three basic types of adsorption bond have already been described.

Ashworth[74] has listed the following factors which may influence adsorption processes on clean metals:

1) The specific surface energy of the particular crystal face which will influence the degree of binding between the surface and the adsorbed atoms.

2) Whether the adsorbed layer of atoms is coherent or incoherent.

3) The nature of the binding forces between the adsorbed atoms among themselves, and between adsorbed atoms and the surface atoms.

4) The relative sizes of the adsorbate atoms and those of the adsorbent.

5) The crystal structure of the adsorbent.

The two techniques by which the above factors may be qualitatively observed most easily are field emission and electron diffraction, both of which indicate the adsorbate distribution and in some cases, structure. However, whereas low- and high-energy electron diffraction are 'macroscopic' techniques, usually requiring large single crystals as substrates, field emission substrates are submicroscopic ($\sim 10^{-9}$ cm^2) and are multi-faced such that comparison of adsorption kinetics on various planes is possible. Thus, preferential adsorption and growth regions may be observed.

According to Ashworth, the first criterion for preferential adsorption is that the adsorbed foreign atom shall fit structurally to the adsorbent surface with the minimum of lattice strain. He has discussed the various relative parameters of bcc and fcc adsorbates on tungsten single crystal faces and has compared his predicted preferred adsorption regions with those experimentally observed. Good agreement is found for Ba, Cs, Th, Na and Cu on single crystal tungsten substrates.

With regard to the present work, this type of analysis proves to be applicable both to the adsorption of uranium and zirconium on tungsten, as described in subsequent chapters.

A mechanism closely associated with adsorption is that of surface diffusion. The motion of a particle diffusing across a crystal surface is dependent upon the variations in the potential field acting on the particle. Thus, observation of migration kinetics allows a map of the potential at the surface to be constructed. The barrier to surface migration on any given substrate can be deduced from the temperature dependence of the diffusion coefficient, thus the variation of atomic binding energy for different surface sites can be examined. This barrier to migration is shown schematically in fig. 9.

As in adsorption studies, field emission and to a lesser extent, field ion microscopy are ideal for surface diffusion studies. The usual procedure has been to shadow the emitter with adsorbate from the side and then to examine the migration kinetics by observing the adsorbate boundary diffusion rate as a function of temperature[70,71,74-80].

The distance x traversed by the boundary in time t is approximately

$$x = (Dt)^{\frac{1}{2}} \tag{32}$$

where D is the diffusion coefficient given by

$$D = a^2 \nu \exp\left(-Ed/KT\right) \tag{33}$$

ν is a frequency of the order of $10^{12}\,\mathrm{sec}^{-1}$, a is a jumplength ($\sim 3$Å) and Ed is the surface diffusion activation energy. Typical of this type of measurement are those for the diffusion of oxygen and hydrogen on tungsten[75,76,80]. The results for oxygen have subsequently been found to be qualitatively similar to those for many adsorbates. Three types of diffusion occur, thus

a) For deposits of greater than one monolayer and at temperatures ~ 27°K a sharp boundary moves uniformly over the emitter, forming an immobile layer. The proposed[80] mechanism is as follows.

At low temperatures the chemisorbed layer is immobile. However, physisorbed gas on top of this layer can migrate over the chemisorbed layer, and be precipitated at the edges, thus extending the layer. For oxygen Ed is 0.039 eV/molecule.

b) For initial deposits of 0.8 to 1 monolayer a moving boundary is observed between 500 and 530°K. The activation energy is 1.11 eV/molecule. The boundary does not move uniformly but spreads radially outward from the central (110) face proceeding more rapidly along some zones than others. A precipitation mechanism can again account for the sharp boundary but the temperature and activation energy indicate migration of chemisorbed atoms. The anisotropy in migration is associated with the variation in binding energy with substrate topography.

c) At low coverage a boundary-free diffusion (Ed = 1.3 eV/molecule) occurs where there is insufficient adsorbate to permit type (b) diffusion. This is simply migration randomly from one trapping site to an adjacent one.

One or more of these types of diffusion have generally been used to describe the migration of most of the adsorbates which have been studied to date. Summaries of experimentally determined surface diffusion parameters have been given by Gomer[80] and Ehrlich[81].

More recently, Ehrlich and Hudda[82] have used field ion microscopy to observe the motion of individual tungsten adatoms on atomically smooth tungsten surfaces. Their results were somewhat unexpected. Previously, Drechsler[83] had shown that, at least for a potential obeying a $^1/_{R^6}$ attraction, the size of the migrating adatom influences the diffusion behaviour. For adatoms with a radius of the order of 1.5 times the crystal radius of the lattice atoms, the highest potential barrier exists in moving toward the (100) plane. Motion over the crystal planes occurs in order of diminishing activation energies, thus, (210) > (211) > (221) > (100) > (111) > (110) . As the size of the adatom approaches that of the lattice, the sequence of diminishing activation barriers becomes (221) > (111) > (210) > (211) > (100) > (110) . Ehrlich and Hudda found that the mobility of tungsten adatoms at room temperature increased in the order (211) > (321) ~ (110) > (310) ~ (111). Also migrating atoms are reflected at the boundaries of the (110), (211), and (321) planes, on the latter two planes motion along atomic rows being favoured over diffusion across lattice steps. Field evaporation has also been employed in two other recent determinations of binding energy. Tamaki and Kuroda[84] have observed the temperature variation of the field evaporation end form of tungsten field emitters. They find the cohesive energy of the surface atoms in the net planes to be greatest for the (100) planes, decreasing progressively in the order (100) > (111) > (110) > (112). They point out that this is inconsistent both with atomic density and work function considerations. Rhodin[85] has observed the field evaporation of Hf, Ta, W, Re, Os, Ir, Pt and Au from tungsten observing an increase in binding energy in the order (111) < (112) < (100) < (110). He explains his results by considering the pairwise - additive interactions used previously in activation barrier estimations and modifying this model to include the electron cloud distribution at the surface. By applying a cosine distribution his experimental findings can be explained. Further disagreement arises from the theoretical predictions of Neustadter and Bacigalupi[86]. Applying the Lennard-Jones 6:12 atom interaction potential to the calculation of adsorption and diffusion energies on bcc substrates, they find a dependence on the adatom/lattice relative parameters in the order of diffusion activation energies. For self-diffusion they obtain the following order for decreasing activation energies (411) > (100) > (111) > (211) > (321) > (310) > (210) > (110).

In view of the migration and nucleation phenomena observed in the present work (described in subsequent chapters) the relative surface diffusion activation energies for the various planes are of some consequence. Clearly, however, there is a need for more experimental work in this realm if the discrepencies between the above results are to be resolved.

3.3 Nucleation and growth

Initiation of a physical or chemical phase transformation on a solid surface usually involves, among other molecular processes, those of nucleation and growth[87]. The heterogeneous condensation

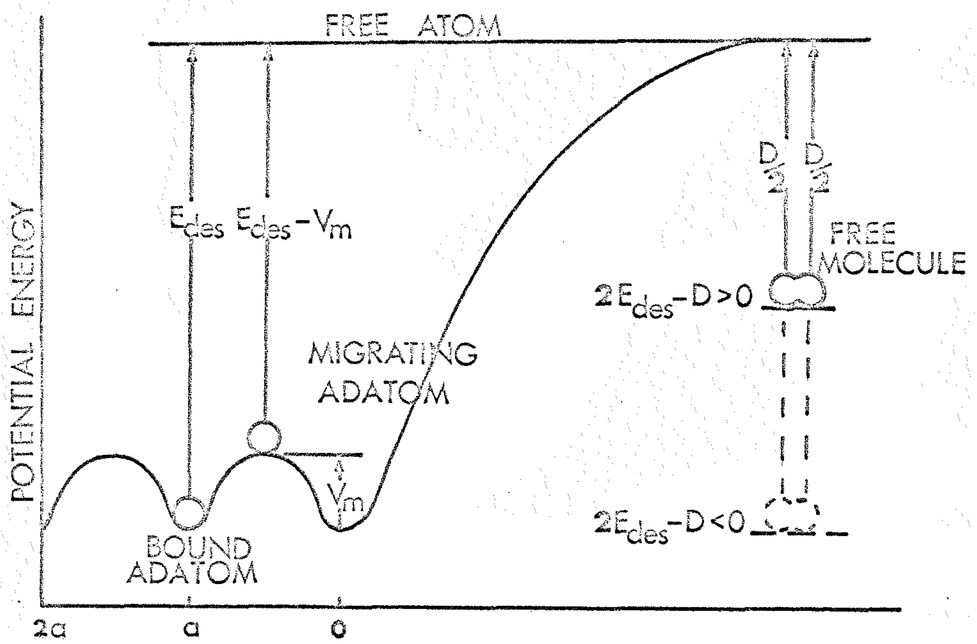

Fig. 9 Variation of potential energy of atoms at a metal surface; a = surface spacing; E_{des} =desorption energy; V_m = barrier to migration; D = dissociation energy of free molecule. (ref. 81)

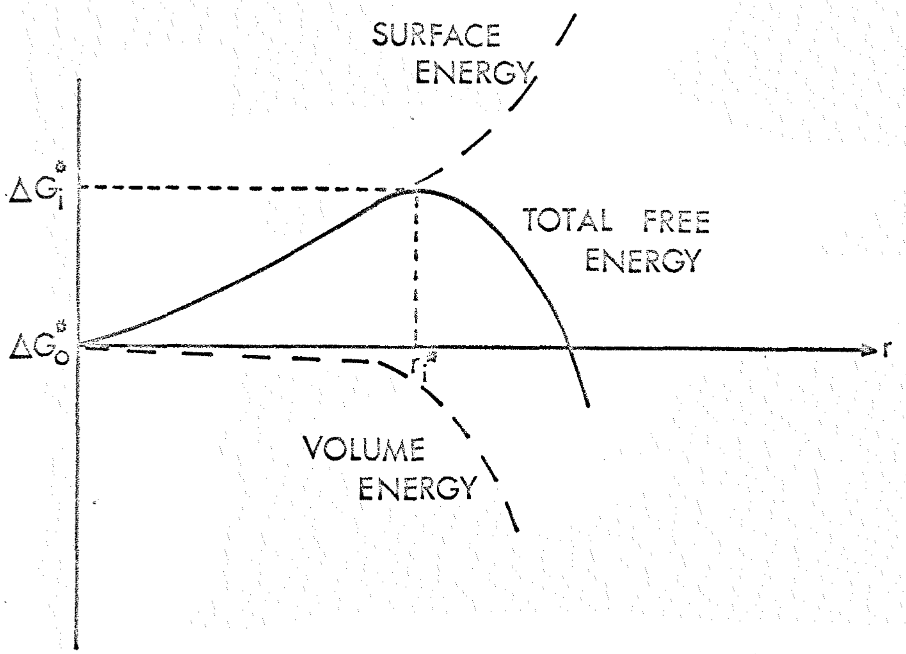

Fig. 10 Dependence of Gibbs free energy of a metastable vapour on the distribution of cluster size.

of a vapour is dependent upon the nature and **temperature** of the surface and upon the nature and incidence rate of the vapour phase itself. These factors are considered briefly below.

3.3.1 Nucleation theories

Nucleation theory is at present based upon either of two basic models; the so-called capillarity model and the atomistic model.

The capillarity model is based on the thermodynamic considerations of the free energy requirements of heterogeneous vapour-solid nucleation. Clusters forming in a supersaturated vapour by the sequential addition of single atoms grow initially with an increase in free energy until a critical size (radius $r_i{}^*$) is reached when growth continues with an overall decrease in the free energy of the system. This is shown in fig. 10[88].

The nucleation rate I is the product of the critical nucleus concentration $n_i{}^*$ and the impingement rate w,

$$I = A^* w n_i{}^* \qquad (34)$$

where A* is the surface area of a spherical drop given in a vapour by

$$A^* = 4\pi r_i{}^{*2} \qquad (35)$$

w is given by the kinetic theory of gases as

$$w = \frac{a_c p}{(2\pi mkT)^{\frac{1}{2}}} \qquad (36)$$

where a_c is the condensation coefficient and the other symbols have their usual significance.

For a surface population of atoms n_1, n_i^* is given by

$$n_i^* = n_1 \exp\left(-\frac{\Delta G_i^*}{kT}\right) \qquad (37)$$

where ΔG_i^* is the critical nucleus Gibbs free energy. (34) (35), (36) and (37) give the Volmer-Weber-Becker-Doring[89] equation for homogeneous nucleation.

$$I = \frac{(a_c p)\ (4\pi r_i^{*2})}{(2\pi mkT)^{\frac{1}{2}}}\ n_1 \exp\left(\frac{-\Delta G_i^*}{kT}\right) \qquad (38)$$

This has been expressed in a more general form by Hirth and Pound[90] as

$$I = wZ\ \Psi(t)\beta n_i^* \qquad (39)$$

where Z is the Zeldovich factor to correct for departure from equilibrium amongst the clusters, $\Psi(t)$ corrects for non-accommodation if impinging atoms, and β is a statistical factor.

An expression analogous to (39) for the nucleation rate on a solid surface is given by Hirth and Pound, thus,

$$I = Cp \exp\left(\frac{\Delta G_{des}^* - \Delta G_{diff}^* - \Delta G_i^*}{kT} \right) \qquad (40)$$

according to the schematic model depicted in fig. 11 where

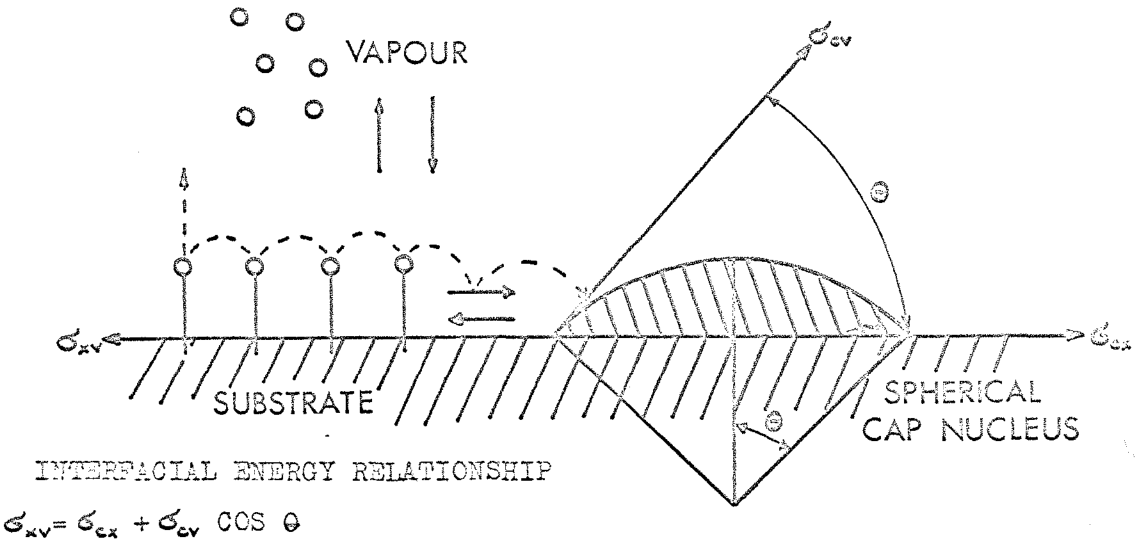

Fig. 11 Schematic description of the simple hemispherical cap model for heterogeneous nucleation.

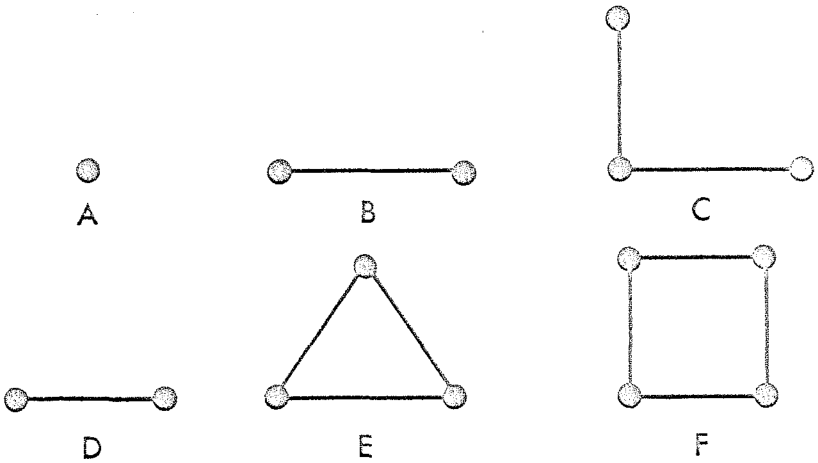

Fig. 12 Schematic atomistic diagrams of smallest stable clusters (D,E,F) and corresponding critical nuclei (A,B,C) for very small clusters on a fcc metal (Walton et al. ref 93)

$$C = \frac{2\pi r Z r_i^* \ a \sin\theta \ n_o}{(2\pi mkT)^{\frac{1}{2}}} \qquad (41)$$

ΔG_{des}^* and ΔG_{diff}^* are the Gibbs free energies of activation of desorption and diffusion of adsorbed atoms respectively, and n_o is the surface density of adsorption sites.

The above approach, in which the free energy of nucleation is expressed directly in terms of the relative changes in specific interfacial energies has proved a useful model in the description of heterogeneous nucleation in many systems. It should be pointed out, however, that the use of bulk thermodynamic properties in an atomic system and the further assumptions concerning the shape of the nuclei can be justified only in certain circumstances. In particular, the theory will not be applicable for systems where the critical nuclei comprise only a few atoms.

Rhodin[88] has discussed some additional considerations relevant to this theory. In particular, it is found that the assumption regarding thermal accommodation of vapour atoms by the surface, and of adatoms by the clusters is justified if the incident energy of the vapour atom is less than 25 times the energy of desorption from the surface. For a monatomic metal this corresponds to complete adsorption for $T < 10^6$ °K [91].

Whilst the capillarity model is satisfactory for systems where $n_i^* \geqslant 100$ atoms, there are many cases where the critical nucleus contains only a few atoms. By considering the clusters as simple macromolecules Rhodin and Walton[87] and Walton[92] have extended the theory to include these small nuclei. The metastable equilibrium concentration of critical nuclei is given by

$$\Delta G_i^* = \Delta E_{oi}^* + i^* \, Kt \ln \left(\frac{n_o}{n_1}\right) \qquad (42)$$

where ΔE_{oi}^* is the potential energy of decomposition of a critical nucleus containing i* atoms at 0^oK, and ${}^{n_o}/n_1$ is the ratio of adsorption sites to adatoms on the surface.

The nucleation rate is given by

$$I = Ra_o^2 n_o \left(\frac{R}{\nu n_o}\right)^{i^*} \exp\left[\left\{ (c^* + 1)\, \Delta G_{des}^* - \Delta G_{diff}^* + E_{o_{i^*}} \right\} /KT \right] \qquad (43)$$

where R is the adatom impingement rate, a_o is the adatom characteristic jump distance during diffusion, and $\nu^{-1} = h/KT$. The nucleation rate is thus expressed in terms of measurable parameters. The disadvantage is that i* and $\Delta E_{o_{i^*}}$ cannot be calculated from first principles. However, i* and $\Delta E_{o_{i^*}}$ can often be determined from the best fits to the experimental data[93]. Fig. 12 shows schematically the atomistic diagrams given by Walton et al[93] of the smallest stable clusters and corresponding nuclei for clusters on a fcc metal.

From the above it is clear that at present there is no generally applicable theory of heterogenous nucleation. The capillarity model is useful provided that the limitations regarding the use of bulk thermodynamic properties are observed. The atomistic approach would provide a more comprehensive theory if the nucleus could be described in terms of the geometry and atomic binding. However, the partition functions and potential energy factors cannot, at present, be evaluated from first principles. The Rhodin-Walton simplification has proved particularly useful however, where nucleation involves very small clusters or imperfections of atomic dimensions which affect the process.

Various aspects of the above theories have been examined experimentally and theoretically by Gretz. He has considered the roles of both adsorption[94] and surface diffusion[95] in heterogeneous vapour-solid nucleation. This has led to the suggestion of a new mechanism for nucleus growth involving the random creation of nuclei which are promoted to critical nuclei by direct impingement of molecules from the vapour. The predicted nucleation rate equation agrees reasonably well with Waltons data for Ag on NaCl. Gretz has also examined the critical adpopulations for appreciable nucleation[96], thermal accommodation coefficients[97], determination of nucleus-substrate contact angles[98], and the line-tension effect[99]. However, his attempts to derive information concerning the size, geometry and growth of the critical nuclei[100] seem to be based on a misinterpretation of the field emission technique, as pointed out by Melmed and Hardy[101].

The relationship between nucleation and epitaxial growth has been summarised by Rhodin[88]. Thus, the occurrence of a large number of nuclei characterized by some specific structural feature may result in the formation of an oriented film. Alternatively, if many types of nuclei occur then the film structure may be dependent upon the relative growth rates of the various types of nuclei. Further, after initial nucleation and growth recrystallization may occur to a structure at lower free energy. The importance of nucleation in the formation of oriented overgrowths has been reviewed by a number of authors[102,103].

3.3.2 Experimental studies of nucleation

The parameters of interest in studies of heterogeneous nucleation may be listed as follows: 1) the size of the critical nucleus 2) the critical adatom concentration required for nucleation 3) the required supersaturation 4) the temperature dependence 5) the nucleation rate 6) the contact angle and 7) the shape of the nuclei. Also of interest is the specificity of adsorption sites, the growth processes occurring, the eventual growth of the film (polycrystalline or oriented single crystal) and the effects of contamination or foreign atomic species on the diffusion and growth. The techniques which have been predominantly utilised in nucleation studies have been electron microscopy (typically in the 10^{-5} torr pressure range), and more recently field emission microscopy in ultra-high vacuum. The electron microscope results are of lesser interest in the present work, the majority of the results being concerned with the effects of surface defects and imperfections and with multilayer deposits on insulating substrates. These results have been reviewed and summarised by a number of authors[103-106].

The field emission measurements are less numerous and include a number already mentioned[94-100]. Moazed and Pound[107] observed the nucleation of silver on tungsten and molybdenum together with the effects of residual gases. Duell and Moss[108] have also studied Ag on W finding preferential nucleation on the higher index planes. Gretz[109] has observed nucleation in multilayer deposits of zinc on tungsten, his results (critical adpopulation equal to 2.7 monolayers) being inexplicable by any of the existing theories of nucleation. Melmed[110] has studied Cu on W observing nucleation and oriented crystal growth. He has further studied the effects of adsorbed gas on the diffusion and nucleation rates[111].

Despite the above measurements, much work requires to be done before nucleation kinetics can be satisfactorily explained in genaral terms. In particular, the field emission technique has not yet been utilised to its full extent in this connection, and a number of problems in interpretation of the results still remain[100,101].

CHAPTER 4

Techniques applicable to the study of Surface Phenomena

4.1 Introduction

Described in this chapter are the methods most commonly used for studying the surface phenomena relevant to the present work, i.e. work function, adsorption, nucleation and growth. The description of the methods is necessarily brief, the techniques which have been used by others for the study of uranium and zirconium being treated at slightly greater length. A somewhat more comprehensive account of the field emission technique used in the present work is given in the following chapter.

4.2 Methods of measuring the work function

The basic methods of work function measurement have been reviewed recently by Rivière[18]. These may be divided into three types of method, direct electron emission measurements, contact potential difference determinations, and surface ionization techniques.

4.2.1 Electron emission methods.

a) Thermionic emission.

The saturated current density j across a uniform surface at temperature T in the absence of an applied field is given by the Richardson-Dushman equation

$$j = A(1 - \bar{r})T^2 \exp(-e\phi/KT) \qquad (44)$$

where $\bar{r}$ is the mean reflection coefficient for incident electrons and A is a universal constant equal to 120 amp/cm^2/deg^2. Thus the work function of such a surface may be obtained from the slope of a Richardson plot of $\ln(j/T^2)$ against $1/T$. However, as has been pointed out by a number of workers[18,20] the assumptions inherent in the derivation of equation (44) are not generally obeyed in practice. It is firstly assumed that the surface is uniform and secondly that the applied field necessary to produce saturation is negligible. In practice most thermionic measurements have been made on polycrystalline substrates. Whilst equation (44) is valid for each of the individual surface patches, the total current depends on the relative magnitudes of the patch fields and the collecting field as well as on the work function. Hence the average work function measured may differ from the true average. Thus, as pointed out by Rivière[18] the surface parameters obtained by thermionic means, whilst related to the true work function and the constant A, are not easily interpretable[112] especially in the cases where a polycrystalline or semiconductor substrate is used.

Thermionic-emission has been used by a number of workers to measure the work functions of uranium[5,6,113] and zirconium[14]. These results have suffered from another disadvantage of this method, namely, that an operating temperature in excess of 1000°K is usually required. This may result in some desorption of the adsorbate, and in the case of uranium means that only the high temperature γ-phase can be studied.

b) Photoelectric Emission

Fry and Cardwell[7] and Lea and Mee[10] have measured the work function of uranium on tungsten by means of photoelectric emission.

If a surface at temperature T is illuminated with light of photon energy $h\nu$, then the zero-field photocurrent near the threshold $h\nu_0 = e\phi$ is given by the Fowler[114]. expression

$$i = B(KT)^2 \, f \left\{ (h\nu - h\nu_0)/KT \right\} \qquad (45)$$

For photon energies near the threshold B is constant and f is a universal function of $(h\nu - h\nu_0)/KT$. If $\ln ({}^{i}/{}_{T^2})$ is plotted against $h\nu/KT$ near the threshold, then the shift along the $h\nu/KT$ axis of this curve from the theoretical curve gives $h\nu_0/KT$ and hence an absolute value for ϕ. As in the thermionic case, problems in interpretation arise for patchy surfaces.

Since photoemission occurs at room temperature, the studies on uranium-coated tungsten photocathodes have not been limited to the high temperature phase. However, measurements on zirconium have not proved practicable as the appropriate photon energies necessitate working in the vacuum ultraviolet region.

c) Field Emission

The field emission technique is described in chapter 5.

Apart from the present work, field emission has been used by a number of workers to study uranium[115,116] and zirconium[15, 16,117,118] although few quantitative work function measurements have been made.

4.2.2 Contact potential difference methods

a) The Kelvin method

In this method, used by a number of workers to study uranium [8,9] and zirconium[119], the surface (A) to be studied forms a parallel plate capacitor of value C, with a reference surface (B) of known work function. These are connected externally in series with an applied potential V_E. The charge on the capacitor is given by

$$Q = C(V_{AB} + V_E)$$

where V_{AB} is the contact potential difference between A and B. If one of the plates is moved, causing a capacity change ΔC, then the charge displacement is given by

$$\Delta Q = \Delta C(V_{AB} + V_E)$$

If now, V_E is varied until $\Delta Q = 0$ when one of the plates is moved, then provided that $\Delta C \neq 0$

$$V_{AB} = -V_E$$

The usual procedure is to vibrate one of the capacitor plates and detect and amplify the charge flow in the form of an a.c. current in the external circuit. This method has been used extensively in this laboratory using sophisticated detection techniques[120] to study uranium and zirconium on both polycrystalline and single crystal tungsten surfaces.

b) Delchar's static capacitor method[121] is similar in principle to the Kelvin technique but instead of vibrating an electrode a compensating potential is applied to reduce the charge flow to zero.

Oatley[122] has described a magnetron method for determining V_{AB}. This suffers from a number of disadvantages concerned with stray magnetic fields and misalignment of electrodes.

Two other methods are Shelton's saturated diode method[128], where the contact potential difference is determined from log (anode current) against retarding potential plots for anode emission in a simple diode, and the breakdown field method where the breakdown potentials for two conductors, between which a thin insulating film is sandwiched, are compared.

Whilst these methods have found general application they have not yet been applied to uranium or zirconium.

c) Anderson's electron beam method[124]

This technique has been used extensively in this laboratory to study uranium and zirconium[9,119].

In this method a collimated narrow beam of slow electrons strikes a surface A at normal incidence. The area struck by the beam should be large on an atomic scale but small compared to the total surface area of A. A characteristic plot of incident current against the potential applied to A is taken. The value of the work function is then changed either by replacing A by another surface B, or by treating the surface A in some way. Another plot is taken, the displacement of this curve from the first along the voltage axis giving the c.p.d. between A and B. The primary source of error is non-parallelism of the characteristic plots caused by collection of electrons by other surfaces, misalignment of A or B or surface patchiness.

A critical comparison of this technique with the Kelvin method has recently been given by Hopkins and Smith[125].

d) The space-charge-limited diode method is similar to the Anderson technique in theory, but differs in experimental arrangement[126]. The anode current-voltage characteristics are measured in the region where the emission is limited by space charge. This method has not, as yet, been applied to uranium or zirconium.

4.2.3 Surface Ionization

The production of positive ions at a hot surface was discovered by Kingdon and Langmuir[127] and has been discussed by Zandberg and Ionov[128]. For a homogeneous surface the ratio of emitted ions to emitted neutral atoms is given by the Saha-Langmuir equation

$$n_+/n_o = A^* \exp \left[e(\phi^* - V_1^*)/KT \right] \qquad (46)$$

where A* is the statistical weight ratio of the ionic and atomic states of an adsorbed atom, V_1* is the ionization potential of the emitted ions, and $\emptyset$* is the substrate work function. Thus, plots of ln (n_+/n_o) against 1/T have slopes proportional to $\emptyset^* - V_1^*$.

Werning[129] obtained a value of $V_1^* = 6.25$ eV for uranium ionized at a polycrystalline tungsten surface, assuming $\emptyset^* = 4.58$ eV. Using a comparison technique based on V_1^* (lithium) = 5.40 eV Bakulina and Ionov[130] obtained a value of 6.08 eV for V_1* for uranium. More recently Hertel[131] has obtained a value of 6.22 eV.

4.3 Techniques for observing adsorption and growth

a) Electron diffraction.

Low- and high-energy electron diffraction have now become standard techniques, used either individually or in conjunction with other methods[132], in studies of the structure of clean or contaminated surfaces and of the early stages of epitaxial growth. The experimental techniques are well described in the literature[133,134].

Whilst these techniques are ideally suited to studies of the adsorption and growth of both uranium and zirconium on tungsten no work in this field has yet been done.

b) Field ion microscopy

The field ion microscope is unique in that the position and behaviour of individual atoms may be observed[135]. This makes it an invaluable tool in the study of adsorption, migration and growth phenomena, and in studies of vacancies, dislocations, radiation damage, cohesive energies and surface site binding energies. A recent modification[136] permits the determination of individual atomic species, thus increasing its uses to studies of impurities and alloy systems.

The microscope does, however, have a number of disadvantages and limitations, and these have so far precluded its use in studying uranium, although zirconium has been observed[16]. The first problem is that a field ion emitter must be smoothed by field evaporation if an atomically smooth surface is to be obtained. As pointed out by Muller[137] the applicability of field ion microscopy to non-refractory metals is dependent upon whether field evaporation or yield to the field stress $\delta = F^2/8\pi$ (F = field at tip surface) occurs first. For a typical evaporation field of 4.75 volt Å^{-1} this stress amounts to 1 ton mm^{-2}. According to Muller[135,137] only W, Ta, Ir, Pt, Rh and Au have sufficient strength at their respective evaporation fields to develop a perfect field evaporation end form without yielding to the field stress. Re, Mo, Nb, V, Pd, Fe, Ni and Co yield to form dislocation networks or slip bands in restricted crystallographic areas[138].

A number of expressions have been put forward for calculating the evaporation field[135,139,140]. The most recent is

$$F = n^{-3}e^{-3}\left[\Lambda + V_n^* - n\phi + \tfrac{1}{2}(\alpha_o - \alpha_i)F^2 - KT\ln \frac{t}{to} \right]^2 \qquad (47)$$

where F is the field strength for evaporation, ne is the simple or multiple charge of the ion (n = 1 or 2), Λ is the vaporization energy of the metal atom, V_n^* is the nth ionization energy, ϕ is the work function of the specific crystal plane, α_o is the polarizability of the metal atom at the surface site, α_i is the polarizability of the free metal atom, t is the desorption time and to is the reciprocal vibrational frequency of the bond atom. For zirconium the evaporation fields for singly and doubly charged ions are respectively 7.00 and 3.45 V/Å. In a previous calculation[135] Muller has given the evaporation field for uranium as 4.24 V/Å. For helium ion microscopy the required image field is 4.50 V/Å. Thus neither uranium nor zirconium could be imaged. In order to overcome this, it would be necessary to use another gas, such as hydrogen (image field 2.28 V/Å) to image the tip. A number of problems arise in the use of other image gases, however. Firstly the resolution is poorer[140]. Secondly, with helium the presence of contaminant gases is of little consequence, these being ionised further from the emitter surface and simply resulting in a diffuse background to the picture. Further, provided that the field is maintained at above about 4 V/Å, the tip will remain uncontaminated. However, hydrogen, krypton, argon and nitrogen all have similar ionization potentials, thus when using any of these gases, contamination by other gases, or by helium or neon is possible. Further, the efficiency of ZnS or $ZnSiO_4$ screen phosphors is lower by an order of magnitude for, say, neon ions compared with helium. This results in longer photographic exposures, or the use of faster (but poorer resolution) film, or requires the use of some means of image intensification.

Shrednik[16] has observed zirconium on tungsten in a field ion microscope, and found it necessary to use hydrogen and deuterium for the imaging gases.

A further problem regarding the use of field ion microscopy to study uranium in particular, is that the interesting phase transition effects occur at $934^{\circ}K$ and $1042^{\circ}K$ respectively. Thus the tip would have to be heated, at least briefly, to these temperatures. This would result in partial blunting[115,141] of the emitter, the tip shape tending to change so as to minimise the free surface energy. Further, it would result in the evolution of gas from the tip and support wire. To prevent this, the emitter assembly would have to be degassed at temperatures in excess of $2000^{\circ}K$. This would result in excessive blunting of the emitter requiring the use of unmanageable voltages.

The use of field ion microscopy to study uranium would therefore appear to be impractical at the present time.

c) Other methods

As mentioned previously, field emission is discussed in the following chapter. Two other techniques, electron microscopy and X-ray diffraction, although in common use have not yet been applied to the uranium or zirconium on tungsten systems.

4.4 Techniques for quantitative measurements

a) Mass spectrometry

The mass spectrometer[142] is now almost a standard requirement in ultra-high vacuum work. Its primary use is to monitor the types and abundances of the residual gases present during all stages of experimentation, also to analyse and determine the purity of artificially introduced gases. A further use, as in the present work, is the determination of the purity of the evaporant from a vapour source, and also to monitor the constancy of the evaporation rate.

Mass spectrometers also provide a convenient means of leak detection.

b) Flash filament experiments

The flash filament method, used in conjunction with mass spectrometry, is of some use in determining sticking coefficients, measuring surface contamination and identifying possible binding states. A study of the technique has recently been given by Yarwood and Close[143].

CHAPTER 5

The Field Emission Technique

5.1 Introduction

The emission of electrons from a solid surface into vacuum resulting from a high field at the surface was first observed by Wood[144] in 1897. Schottky[145] attempted an explanation in terms of thermionic emission over a potential barrier, the height of which had been lowered by the external field. However, Gossling's [146] measurements of field emission current/voltage characteristics failed to confirm Schottky's predictions and he came to the conclusion that the application of quantum theory to the problem was necessary. This was done in 1928 by Fowler and Nordheim[147] who applied Fermi-Dirac statistics to the metal electrons to calculate the energy distribution. They then calculated the number of electrons arriving at the inside of the potential barrier for each energy range. Solution of the Schroedinger equation gave the fraction of electrons penetrating the barrier. By multiplying the number of electrons arriving at the barrier by the probability of quantum mechanical tunnelling through the barrier and integrating over all energies a formula for the emission current was obtained. Nordheim[148] later modified the expression to include the image force deformation of the barrier. His calculations, however, included some errors and these were subsequently corrected by

Burgess, Kroemer and Houston[148].

The Fowler-Nordheim theory is still accepted as the best description of the field emission process. It has been discussed recently by van Oostrom[149] and Itskovich[150].

5.2 Field emission theory

5.2.1 General

Whereas in thermionic and photoelectric emission electrons with sufficient energy pass over the surface potential barrier, in field emission the barrier is deformed and the electrons pass through by quantum mechanical tunnelling. Fig. 13 shows a potential energy diagram for an electron at a metal surface in the presence of an applied field, with the image potential included[80]. The image force is the Coulomb attraction between an electron outside the surface and its induced charge in the metal.

Derivations of the emission equation have been given by a number of authors[80,115,147,149] the procedure being to calculate the penetration coefficients for the one-dimensional barrier by the WKB method[151] and to multiply these by the arrival rate of electrons at the barrier. The result is the Fowler-Nordheim equation

$$i = 1.54 \times 10^{-6} \frac{\beta^2 V^2 S}{\phi t^2(y)} \exp\left(-6.83 \times 10^7 \frac{\phi^{3/2}}{\beta V} f(y)\right) \qquad (48)$$

where i is the emission current at applied voltage V, S is the emitting surface area, β is a geometrical factor relating the

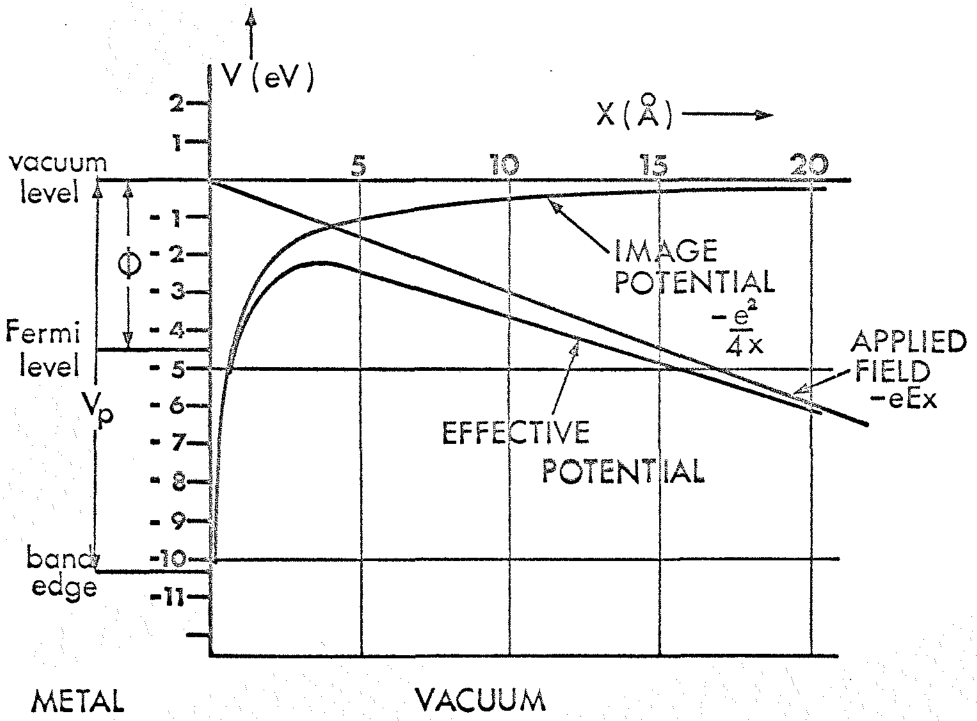

Fig. 13 The potential energy (eV) of an electron as a function of its distance X (Å) to the surface of a metal. ϕ is the work function, V_p the potential energy of the electron in the metal and E the electric field strength (0.3 v.$Å^{-1}$)

surface field to the applied voltage, and t and f are image correction terms. To a first approximation equation (48) may be written

$$i = AV^2 \exp \left(\frac{\phi^{3/2}}{CV} \right) \qquad (49)$$

where A and C are constants.

The curve obtained by plotting $\ln(i/V^2)$ against $10^4/V$ is called a Fowler-Nordheim plot. If the image force terms are neglected and ϕ and β are independent of V, then the curve is a straight line of slope.

$$m = \phi^{3/2}/C$$

The Fowler-Nordheim model is based on four assumptions.

1) The free-electron approximation is applicable in the metal
2) The temperature of the metal is 0°K
3) The surface is smooth and plane
4) The potential close to the surface in the vacuum region consists of an image-force potential and a potential due to the applied field

The validity of the model based on these assumptions has recently been critically reviewed by van Oostrom[149]. He came to the general conclusion that the Fowler-Nordheim model provided a satisfactory description of the field emission process. All four of the basic assumptions were found to be in good agreement with the experimental results. Total-energy distribution measurements at low temperature, however, indicated that somewhat better agreement is obtained using a corrected image force potential.

5.2.2 The field emission work function

Determination of absolute work functions from equation (48) requires a knowledge of the emitter geometry in order to establish the values of S and β. The work function values obtained in this way are not generally reliable to better than ± 15%. The more usual procedure is to measure the change in work function during adsorption by means of Fowler-Nordheim plots, the ratio of the slopes of such plots being the $^3/_2$ power of the ratio of the corresponding work functions. Whilst this method has been widely used it is not entirely clear how the work functions obtained relate to those determined by other methods. Firstly, a supposition inherent in the above method is that β does not change on adsorption and that there is no change in the relative emission anisotropy of the emitter during adsorption[80]. Secondly, the measurements are taken at fields of the order of 0.4 V/Å, and the work function obtained, ϕ_{FN}, is a value extrapolated to zero field. Thirdly, the emitter is necessarily microscopic in size ($\sim 10^{-9} cm^2$), and whilst its surface topography is reproducible, the distributions of crystal planes on the surface are unlikely to correspond to those present on macroscopic substrates such as polycrystalline foil. Some mention must also be made of the disagreement amongst previous workers[152,153] concerning the effects of the predominant emitter orientation. Gorbaty and Gofman[153] have measured the average work functions of (110), (111) and (100) oriented tungsten emitters, finding values of 4.55, 3.40-3.45 and 3.55-3.65 eV respectively. On the other hand Little et al[152] have measured the ratio of the slopes of Fowler-Nordheim plots for clean and CO-covered emitters, finding no difference between (110) and (100) oriented tips. It is thus clearly necessary to clarify the effects of the emitter orientation in order to correctly interpret the field emission work function. Lastly, field emission work functions determined in this way are calculated assuming the clean value for the emitter average work function. In no case is this exactly known; the most common value used being 4.50 eV for clean (110) oriented tungsten. However, there is no experimental or theoretical justification for using this in preference to the polycrystalline value of 4.55 eV[19].

An alternative method of measuring the work function arises from a modification of the Fowler-Nordheim equation suggested by Klein[154]. Combining the Fowler-Nordheim equations for the clean and adsorbate covered surfaces gives

$$\phi^{*3/2} = \phi^{3/2} \left(\frac{V^*}{V}\right) + \frac{\beta V^*}{6.83\text{x}10^7} \left(\ln \frac{V^{*2}\phi}{V^2\phi^*} + \ln \frac{S^*}{S} \right) \qquad (50)$$

where the asterisks indicate the parameters for the adsorbate covered emitter. The first logarithmic term is relatively small[70] and if we assume that there is no change in the emitting area during adsorption then the second logarithmic term may be disregarded, whence

$$\phi^* = \phi \left(\frac{V^*}{V}\right)^{2/3} \qquad (51)$$

where ϕ, ϕ^*, V and V* are the work functions and voltages required to draw a given emission current form the clean and adsorbate-covered emitter respectively. The assumptions inherent in deriving this equation are clearly that β and the pre-exponential term in equation (48) do not change during adsorption. Schmidt and Gomer[70] have shown that equation (51) is obeyed for the system K on W and suggest that it holds for electropositive adsorption in general. However, considerable errors may be introduced due to changes in S during adsorption of electronegative adsorbates. This equation has been used by a number of workers particularly for measurements on single crystal planes and for systems where the measurements have to be taken rapidly[155-160].

It must suffice however, to point out that the concept of the field emission work function is not well defined and that the effects of variations in the preexponential term in particular require some clarification. An example of these problems is given by Ehrlich and Hudda[161] concerning the adsorption of nitrogen on tungsten.

5.2.3 Recent theories

Duke and Alferieff[162] have pointed out that the Fowler-

Nordheim model, which assumes that adsorption alters the emission only via a work function modification is inadequate. This is because the adsorbate changes the shape of the electrostatic potential seen by the tunnelling electrons, and also because the adatoms can act as "energy-momentum sinks" for these electrons. They therefore consider the adsorbate potential to be atomistic in nature consisting of a square well outside the metal surface. This effectively forms a double potential barrier the shape of which results in either an increase or a decrease in the transmission probability compared with that derived in the usual Fowler-Nordheim theory. Using this modified theory, they have attempted to explain the unusual effects (simultaneous lowering of ϕ_{FN} and the emission current on the (100) and (411) planes) observed[161] for nitrogen on tungsten. Experimental evidence to support their model has been given by Ermrich and Van Oostrom[163].

Cutler and Nagy[164] have modified the surface potential barrier in the Fowler-Nordheim theory. Their new potential represents a modification to the classical image-force and is based on quantum mechanical calculations of the electronic potential in the surface region of the metal. They find improved agreement with experimental observations of emission characteristics using their model.

More recently Nowicki[165] has examined the influence of space-charge on the potential barrier. He obtained an expression for the increase in effective work function as a function of applied field and cathode radius using an electrical image method. The deviation from linearity of Fowler-Nordheim plots predicted by this theory are in good agreement with experimental results. He further showed that the influence of space charge on the applied field at the cathode is of less importance than its influence on the potential barrier.

5.3 Field emission microscopy

5.3.1 General

The field emission microscope in its first form[166] comprised a metal filament mounted along the axis of a cylindrical evacuated glass tube as shown in fig. 14. The inner wall of the tube was coated with a conducting fluorescent screen and by application of several thousand volts between screen and filament a pattern of electrons emitted normally from the wire could be obtained. However, the magnification obtained was only of the order of 10^3, and the resolution was poor.

The advent of Müller's spherical microscope[23] in 1936 marked the beginning of field emission microscopy as a useful technique in surface studies. By etching a fine tungsten wire in molten sodium nitrate Müller was able to produce a pointed emitter with an end radius of ~ 1 micron. This emitter, approximately 1 mm in length was spotwelded to a tungsten hairpin and mounted at the centre of a spherical tube. A fluorescent screen was coated on the inside of the bulb and an anode ring mounted in front of the

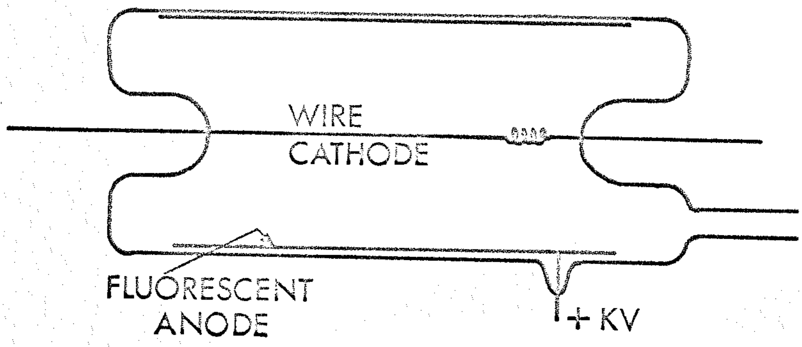

Fig. 14 Cylindrical form of field emission microscope.

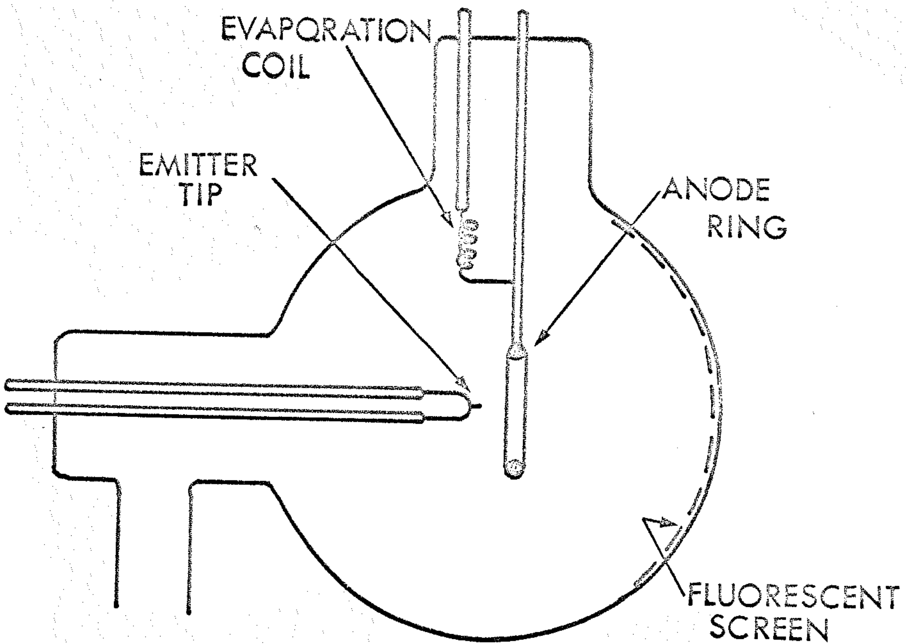

Fig. 15 Spherical form of field emission microscope.

emitter, as shown in fig. 15. The most important discovery was that by heating the emitter in ultrahigh vacuum at temperatures in excess of 2000°K (for tungsten) a hemispherical surface, smoothed down to atomic dimensions could be obtained, and further that the emission pattern obtained was both reproducible and the individual planes identifiable (fig. 16). Magnifications of 10^5 - 10^6 are obtainable with a resolution of about 20 Å, the limit of resolution being set by the statistical distribution of momenta transverse to to the emission direction[80,167], rather than by diffraction effects.

Modern microscopes are essentially the same as in fig. 15, except that the anode ring is generally replaced by a conducting coating of stannous oxide under the fluorescent screen.

5.3.2 The field emitter

The techniques employed in preparing emitters have been summarised by a number of authors[80,115,135]. In general, only metals with high melting points have been used by previous workers, oxides and surface contamination being removed by heating. Heater loops are generally made of the same material as the emitter to prevent alloying. In the present work, tungsten has been used as the emitter material. This is mounted on the heater loop prior to initial shaping. The emitter is then roughly shaped by chemical or electrochemical etching in molten $NaNO_2$ or NaOH, or in aqueous solutions of NaOH, KOH or KCN. In the present work this was performed by placing the emitter in a 0.5 N solution of NaOH

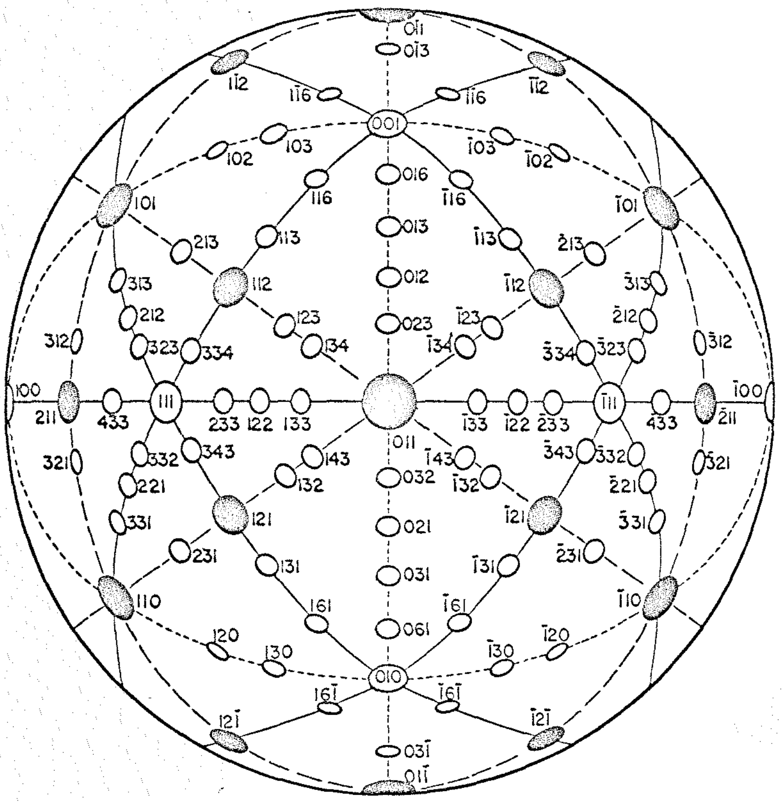

Fig. 16

Orthographic projection of hemispherical cubic crystal with (011) along the axis. The planes shown are those predominating in bcc crystals.

and applying 1 - 10 volts a.c. between the tip and a nickel electrode. With practice, little difficulty is encountered in preparing emitters with tip radii of a few hundred angstroms.

A number of alternative etching procedures have been described by various workers. A common method is to float a layer of about 2 mm of KCN[168] or NaOH[149] on the surface of carbon tetrachloride. The emitter material is then lowered so as to project through the electrolyte and an a.c. voltage applied. The emitter material then necks in the electrolyte region and the lower portion falls away. Problems are encountered occasionally[168] due to stress-induced defects in the surface, but these can usually be removed by etching backwards along the tip to remove the deformed layer. A more sophisticated etching procedure whereby the specimen cone angle can be controlled has been described by Melmed[169]. In this method, the electrolyte is held in the form of a bead of liquid in a wire loop and is observed in a microscope at 100 X magnification. The tip is inserted into the bead of solution and several volts a.c. applied. The gas bubbles produced coalesce to form a larger bubble and the wall of this bubble is then used (at reduced voltage to prevent further gas evolution) to 'hone' the emitter as it is moved back and forth. A further etching procedure using an aqueous solution of 20% potassium sulphite containing 0.5% hydroquinone has been described by Fasth et al[170]. They claim that this produces contamination free emitters of optimum tip radii and cone angles.

After the initial etching, the emitter is placed in the microscope which is evacuated. The final shaping and smoothing of the emitter is then performed in ultra-high vacuum by heat treatment. According to Good and Muller[115] perfect smoothness in achieved after heating for a few minutes at $^2/_3$ of the absolute emitter melting temperature. The smoothing arises due to the migration of surface atoms which rearrange themselves to minimise the free surface energy. The fabrication, surface migration and blunting of tungsten emitters have been described by Dolan et al[171-173].

Two methods have been described by Muller for sharpening emitters in situ. These are oxidation of a pre-etched tip at reduced oxygen pressure followed by evaporation of the oxide layer in ultra-high vacuum[174] and cathode sputtering[175] using the heavier noble gases or mercury.

Drawn tungsten wires usually have a (110) orientation along the axis, other orientations occasionally appearing as a result of disoriented grains in the crystal structure. Grain boundaries are also infrequently observed, such emitters being discarded as they are of little practical use in work function determinations.

5.3.3 Applications of the emission microscope

The general applications of field emission microscopy have been summarised by Gomer (ref. 80, chapters 2, 4 and 5) and some of these have already been mentioned in the present text. The principle applications are in studies of adsorption, migration and nucleation parameters, and also to the measurement of work function. A number of subsidiary uses may also be mentioned. One of these is the study of large molecules, the most widely known being Mullers work on copper phthalocyanine[176]. Two-fold and four-fold molecular images are observed although the mechanism of the image formation is not entirely clear. The kinetics of whisker growth can be followed using emission microscopy as the whiskers are often suitable for use as field emitters without further sharpening or smoothing[177,178]. This technique allows the study of a large number of materials, such as Hg, which could not otherwise be observed using field emission. Field emission can be extended to surface tension studies by applying a field just sufficient to prevent blunting of a heated emitter. Thus, by balancing the electrostatic and surface tension forces, the surface tension can be calculated[179,180]. A certain amount of work has been done using emission microscopy in the study of surface phases and overgrowths. In particular, carbide, oxide and silicide[80,115,154,181] overgrowths have been investigated. Emission microscopy is particularly suitable for the study of oxidation and corrosion.

A property of the field emission microscope which is often useful is its ability to detect small amounts of contamination, and also to differentiate between different contaminant species by their respective emission patterns. Thus, the microscope can be used as a pressure gauge by observation of emitter contamination times and also the contents of gas mixtures can often be determined.

Further uses of the emission microscope are in polarizability measurements[115] and in applications of the unusual electron-optic properties of emitters[179,182]. A recent modification by Melmed[183] is the field emission shadow microscope. In this device, the emitter is used as a point source of electrons producing magnified profile images of small electrically conducting objects placed immediately in front of the emitter. Melmed claims that magnifications of better than 20,000X with a resolution to between 10 and 30 Å should be possible.

CHAPTER 6

Properties of Uranium and Review of Previous Measurements

6.1 General

Interest in uranium arose as a consequence of the development of the chain-reacting nuclear pile and the atomic bomb. Extensive investigations have resulted in a comprehensive knowledge of the physical and chemical properties of uranium[184].

Uranium is the heaviest naturally occurring element (atomic number 92), natural uranium containing three isotopes, U^{238} (99.276%) U^{235} (0.718%) and U^{234} (0.0056%). The atomic weight is 238.07 amu.

Uranium is a member of the actinide transition series in the periodic table in which the 5f shell is being filled. The 6 valence electrons in a free neutral uranium atom in the ground state are in a configuration $5f^3 6d7s^2$. Uranium chemistry is extremely complex and has been dealt with fully by Katz and Rabinowitch[184].

6.2 Chemical Analysis

The uranium used in the present work was natural uranium supplied by U.K.A.E.A., Harwell. A detailed chemical analysis is unfortunately not available. However, given below is a typical analysis in p.p.m. for natural uranium.[185]

C	700	O	200	Si	50	N	25	Al	20	Cu	20
Zn	< 20	Mg	10	Mn	10	Zr	< 10	Ba	< 10	P	< 10
V	< 10	Ca	5	Sn	< 5	Cr	< 3	Bi	< 2		
Be	< 1	Co	< 1	Pb	< 1	B	0.2	Cd	0.1	Ag	< 0.1

It should be noted however, that the above applies to a clean untarnished sample. In practice, in air at room temperature massive uranium metal oxidizes slowly, firstly assuming a golden-yellow colour and then becoming darker. After several days the metal is completely covered with a black oxide layer, this layer however, does not prevent further oxidation. This means that the samples used in the present work were initially heavily oxidised. These were cleaned prior to mounting in the tube by electro-etching in a solution of 85% H_3PO_4 and 15% H_2SO_4. However, partial oxidation was bound to occur prior to evacuation and also during bakeout, the monoxide UO being formed at low pressure (10^{-5} torr). Thus, whilst the above analysis indicates the impurities in the bulk of the sample; the samples actually used would have a much higher oxygen content.

6.3 Crystallographic properties

Below its melting point (1403°K) uranium exists in three distinct allotropic forms[186,187]. It is enantiotropic, each form being stable only in its own temperature range. The phase transition temperatures are 934°K and 1042°K, but these vary, dependent upon the purity of the sample and whether the sample is being heated or cooled. The effect of the rate of cooling on the transformation temperatures has been investigated by Duwez[188] who used cooling rates up to 8000°C/sec. He found that the transformation temperatures are lowered when the cooling rate in increased, but that the conversion of gamma to alpha uranium is very improbable, and further that it was not possible to 'freeze in' either of the high temperature phases, the alpha phase always recurring at room temperature.

6.3.1 Alpha uranium (stable below 934°K)

The accepted structure of alpha uranium is orthorhombic with room temperature lattice constants[189]

$$a_o = 2.852 \text{ Å}, \ b_o = 5.865 \text{ Å}, \ c_o = 4.945 \text{ Å}$$

As shown in fig. 17[186] the structure is like hexagonal metals except that successive layers of atoms in the basal plane are skewed back and forth in the (010) directions. The important features of the structure of alpha uranium have been reviewed by Tucker[190]. Pauling[47] has pointed out that the four nearest neighbours to any uranium atom in the ac plane strongly resemble the trigonal bipyramid structure of strongly covalent compounds such as PCl_5. The similarity is shown in fig. 18[186]. As pointed out by Holden[186] one of the uranium atoms is missing and is replaced by a pair of unshared electrons. The high degree of covalent binding and the effects on the physical

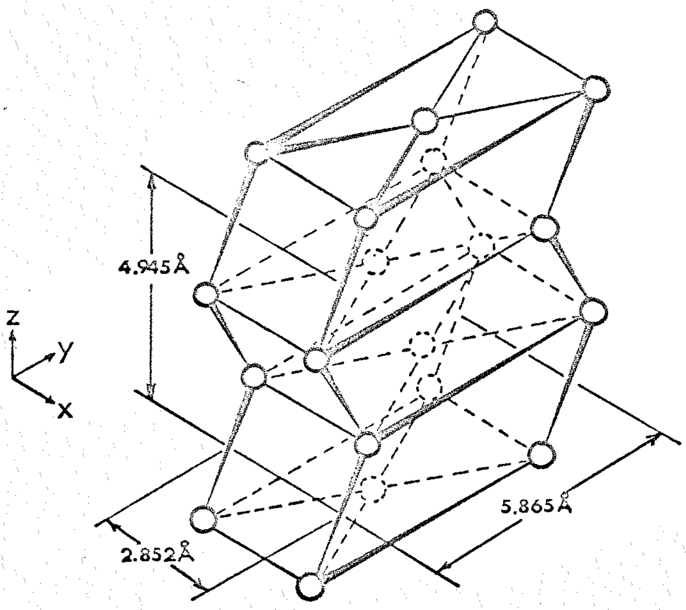

Fig. 17 Crystal structure of alpha uranium.

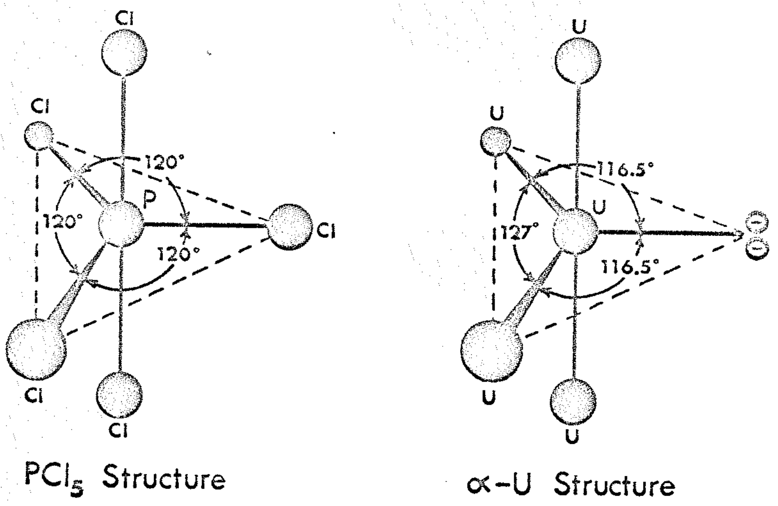

PCl_5 Structure

α-U Structure

Fig. 18 Similarity of alpha uranium to typically covalent PCl_5 structure showing trigonal bipyramid in each.

properties of alpha uranium have been discussed by Friedel[191].

6.3.2. Beta uranium (stable range 934 - 1042°K)

Beta uranium has a complex tetragonal structure containing 30 atoms per unit cell[192]. The atomic stacking arrangements have been given by Holden. Beta uranium has a layer structure with two types of layer perpendicular to the c-axis. The layers are densely populated (interatomic distances as small as 2.59 Å) with geometric configurations similar to hexagonal packing. There is no clear evidence for a particular bond arrangement as in alpha uranium.

At the present time there is some disagreement between the work of Tucker[192] and Thewlis[193] concerning the detailed structure of beta uranium. These problems appear to arise due to experimental difficulties in obtaining pure uranium samples and the necessity of using alloys.

6.3.3 Gamma uranium (stable above 1042°K)

Gamma uranium has a b.c.c. structure, the most reliable value for the lattice constant being $a_o = 3.538$ Å given by Klepfer et al[194].

6.3.4. The metallic radius

The size of the uranium atom is not well known. The most reliable value for the metallic radius appears to be 1.426 Å, given by Pauling[47], calculated empirically from the bond lengths.

6.4. Uranium-Tungsten alloys

As the substrate used in the present work was a tungsten field emitter, and further, the evaporation sources comprised uranium globules mounted on tungsten filaments, consideration of the uranium-tungsten alloy system is in order. As pointed out by Barry et al[9] the transition metals of group IV, V and VIA have favourable size factors with respect to uranium and generally continuous body centred cubic solid solutions are formed. Tungsten however, appears to be an exception. Schramm et al[195] have measured the solubilities of tungsten in uranium and uranium in tungsten at elevated temperatures, finding values of less than 1 at % in each case. No intermediate phases are formed and the tungsten has little effect on the α-β and β-γ transformation temperatures. Summers-Smith[196] has made similar measurements at 1273°K, finding the solubility of tungsten in α-uranium about 0.9 ± 0.3 at %, and of uranium in tungsten about 0.1 at %.

6.5. Previous measurements of uranium surface properties

6.5.1 Work function

Table 1 lists the values published to date for the work function of uranium. The measurements prior to 1959 are unfortunately not satisfactory with regard to the vacuum requirements necessary for work function measurements. The more recent measurements are generally in good agreement, particularly for the high temperature phase, considering that several different

Date	Reference	Method	α-U	β-U	γ-U	System	Comment
			Work function (eV)				
1923	Dushman[197]	T			3.28	U on W filament	poor vacuum conditions
1932	Rentschler[12]	P	3.63			U sputtered on N_i	"
1938	Klein et al[198]	C	4.32±0.05			U foil in Ar	"
1939	Hole et al[199]	T			*3.56±0.05	U wire	"
1959	Rauh et al[6]	T			*3.47±0.03	U on W foil	up to 200 monolayer deposits
1962	Fry et al[7]	P	3.47±0.01	3.52±0.01	3.39±0.01	U foil	U insufficiently outgassed
1962	Rivière[8]	C	3.188±0.013			U on W foil	100 monolayer deposits
			2.93±0.005			U foil	
1963	Haas et al[5]	T			3.45	U on W wire	
1967	Barry et al[9]	C	3.63±0.01	3.58±0.01	3.53±0.01	U on W foil	monolayer deposits
1967	Lea et al[10]	P	3.65±0.01	3.59±0.01	3.45±0.01	U on W foil	monolayer deposits

* corrected to effective[112] work function

C: contact potential difference; P: photoelectric emission; T: thermionic emission.

TABLE 1

measurement techniques have been used. The most obvious discrepency is Rivières values for α-uranium, the values obtained being sufficiently lower than the other values to be inexplicable in terms of differences in measurement technique. A possible explanation is that whilst several of the other authors were observing slowly deposited monolayer films of uranium, Rivière's work was on thick (~ 100 monolayer) films deposited quickly.

6.5.2 Ionization potential

The recent values have been mentioned in section 4.2.3. Of these, Hertels[131] value of 6.22 ± 0.06 eV is probably the most reliable.

6.5.3 Structural properties

Very little work on the adsorption or growth properties of uranium has been performed to date. Müller, using field emission microscopy has observed UO_2 adsorption on tungsten; an epitaxial layer forming on the (112) planes[200]. He has also observed the adsorption of uranium metal, microcrystallites forming on the (112)'s. However, this work was only of an exploratory nature and no further publication has been made[201].

Kolomiets[202] has attempted to produce β-U in thin films condensed at pressures of 10^{-4} torr on collodian substrates. His work was an attempt to resolve the indecisive measurements of Chatterjee[203] and Donohue[204] concerning the structure of the films formed under these conditions. His results indicated that the films contained a significant proportion of uranium monoxide, no β-uranium being observed.

6.5.4 Gas contamination studies.

Vedula et al[205] have observed the effect of electron bombardment on the adsorption properties of tungsten surfaces. By observing the variation of work function with heat treatment for the U - W system, they came to the conclusion that the difference in the work function dependences observed for surfaces that have and have not been subjected to electron bombardment cannot be related to a combined adsorption of residual gas molecules with the U atoms. This followed work of Zingerman et al[206] who had attempted to explain work function variations after electron bombardment in terms of adsorption of gaseous contamination.

The effects of hydrogen contamination on the work function of uranium have been investigated by Rivière[207] and by Hopkins and Sargood[208]. Whilst both authors observe an increase in the work function, their values differ by an order of magnitude. These results are discussed by Appendix 1.

The surface potential of oxygen on uranium has also been studied by Rivière[209]. A positive surface potential is found and Rivière has postulated a model involving initially ionic bonding, followed by penetration of oxygen atoms into the uranium lattice.

Ackermann et al[210] have studied the effect of oxygen on the vapour pressure of uranium. With regard to the present work, their most important result is the fact that dissolved oxygen cannot be completely removed from a uranium sample without heating to above 2000°K.

CHAPTER 7

Properties of zirconium and review of previous measurements

7.1 General Properties and Uses

Zirconium (atomic number 40, atomic weight 91.2) is a group 4 element which has been widely used since large scale zirconium production commenced in 1953[211]. It finds uses in nuclear power installations due to its low thermal neutron cross section combined with its exceptional corrosion resistance, a property which makes it useful in chemical equipment applications. Further, zirconium is an excellent getter and its advantages as such have been described by Espe[212]. For example, zirconium will absorb 62.4 torr litres of oxygen, or 23.35 torr litres of nitrogen per gram at room temperature. Zirconium will not alloy or amalgamate with mercury and can thus be used in mercury arc or vapour vacuum tubes. The corrosion resistance of zirconium results also in its use in neurosurgery. According to Cauchoix and Lavarde[213] the two most suitable metals for such applications are tantalum and zirconium, zirconium being somewhat less toxic.

The general physical and chemical properties of zirconium have been described by Miller[211]. The melting point is 2128 ± 15°K.

7.2 Chemical Analysis

The zirconium used in the present work was 99.5% purity wire supplied by Koch Light Laboratories Ltd. A typical analysis in p.p.m. is given below:-

O_2	410	Fe	240	Hf	< 200	C	170	Cl	150
Al	65	Cr	65	Na	< 50	H_2	< 50	Ca	< 25
Mn	22	Ti	< 20	N_2	16	Mo	10	Co	< 10
Pb	< 10	Mg	< 10	Si	< 10	V	< 10	Cu	6
N_i	5	U	< 3.5	B	< 0.5	Li	< 0.5	Cd	< 0.4

The same problem is encountered with zirconium as with uranium, namely that whilst the above analysis represents a bulk sample, the specimens used in practice are initially highly oxidized. Some difficulty was encountered in cleaning the wire. A 10% HF solution removed the outer oxide layer but as with the uranium, further oxidiation occurred prior to mounting in the tube and evacuating. Thus oxygen was again the most important contaminant in the present work.

7.3 Crystallographic properties

Zirconium undergoes an allotropic modification at 1135°K. Below this temperature the hexagonal close packed alpha form is stable and above it the bcc beta phase is stable up to the melting point. The lattice constants are 3.230 Å and 5.133 Å for the alpha phase, and 3.62 Å for the beta phase. Mechanical treatment has little effect on the transition temperature but absorption of oxygen, nitrogen and hydrogen do. Oxygen and nitrogen raise the temperature while hydrogen lowers it. The effects of a large number of other elements on the phase transformation have been described by Miller.

7.4 Zirconium-tungsten alloys

The zirconium-tungsten system has been investigated by Domagala et al[214]. They found that less than 10% zirconium is soluble in tungsten, that the solubility of tungsten in α-zirconium is less than 0.5% at all temperatures, and that the limit of solubility of tungsten in β-zirconium is about 8% at about 1925°K.

7.5 Previous measurements of zirconium surface properties

7.5.1 Work Function

There are at present few reliable values for the work function of zirconium. Early measurements by Dushman[197] (3.28 eV), Zwikker[13] (4.12 eV) and Rentschler et al[12] (3.73 eV) are unsatisfactory with regard to degassing and vacuum conditions. Wright[14] has given a value of 3.1 eV for zirconium coated tungsten thermionic emitters, but the experimental conditions are not clear.

Shrednik[15,16] using field emission microscopy has given values from 3.84 - 2.62 eV for various coverages and experimental conditions. Many of his measurements however, are of little value, in particular those made on emitters showing grain boundaries[16] and at pressures in the 10^{-8} torr range. His most reliable value appears to be 3.84 eV.

Good agreement with Shredniks value of 3.84 eV[15] is found with measurements in this laboratory[215] using contact potential difference techniques. For monolayer deposits of zirconium on polycrystalline tungsten a value of 3.87 eV is obtained.

7.5.2 Ionization potential

Vedeneyev et al[216] give a value for the first ionization potential of zirconium of 6.84 eV. This is in good agreement with Michaelson's earlier value[32] of 7 eV.

7.5.3 Structural properties

Very little work has been done on the adsorption and growth properties of thin zirconium films. Muller[116] observed unusual migration properties using emission microscopy, but his deposits probably contained oxide contamination. Further field emission investigations by Shrednik[15,16] indicated growth on the (100) tungsten planes under heat treatment and Fursei and Shakirova[117] have attempted to utilise this phenomenon to produce high current density semi-collimated electron sources. Much of this work, however, was performed under poor or ill-defined experimental conditions.

Rhodin[118] has studied nucleation of zirconium on tungsten, but his results have not been published.

CHAPTER 8

General Experimental Techniques

8.1 Introduction

In this chapter the general vacuum and measurement techniques are presented together with details of general tube, emitter and evaporator assemblies and their modes of operation. The design and development of the experimental tubes is deferred until the following two chapters as the results obtained are best presented in conjunction with the individual tubes from which they were obtained.

8.2 Ultra-high Vacuum. System and Techniques

8.2.1 The Vacuum System.

Three separate glass vacuum systems were used at different stages of the work. These were identical apart from the inclusion of a Vacuum Generators bakeable metal tap in the first system. The systems were constructed of pyrex glass and were mounted on rigid tubular metal frames. A schematic diagram of the general layout of the systems is shown in fig. 19.

Each system was evacuated initially by means of a Speedivac two-stage model 2SC 20A rotary pump mounted on a rubber pad to minimise vibration. This was joined to a glass oil trap by a short length of rubber tubing. Two greased ground-glass stop-cocks were incorporated at this point, one to isolate the

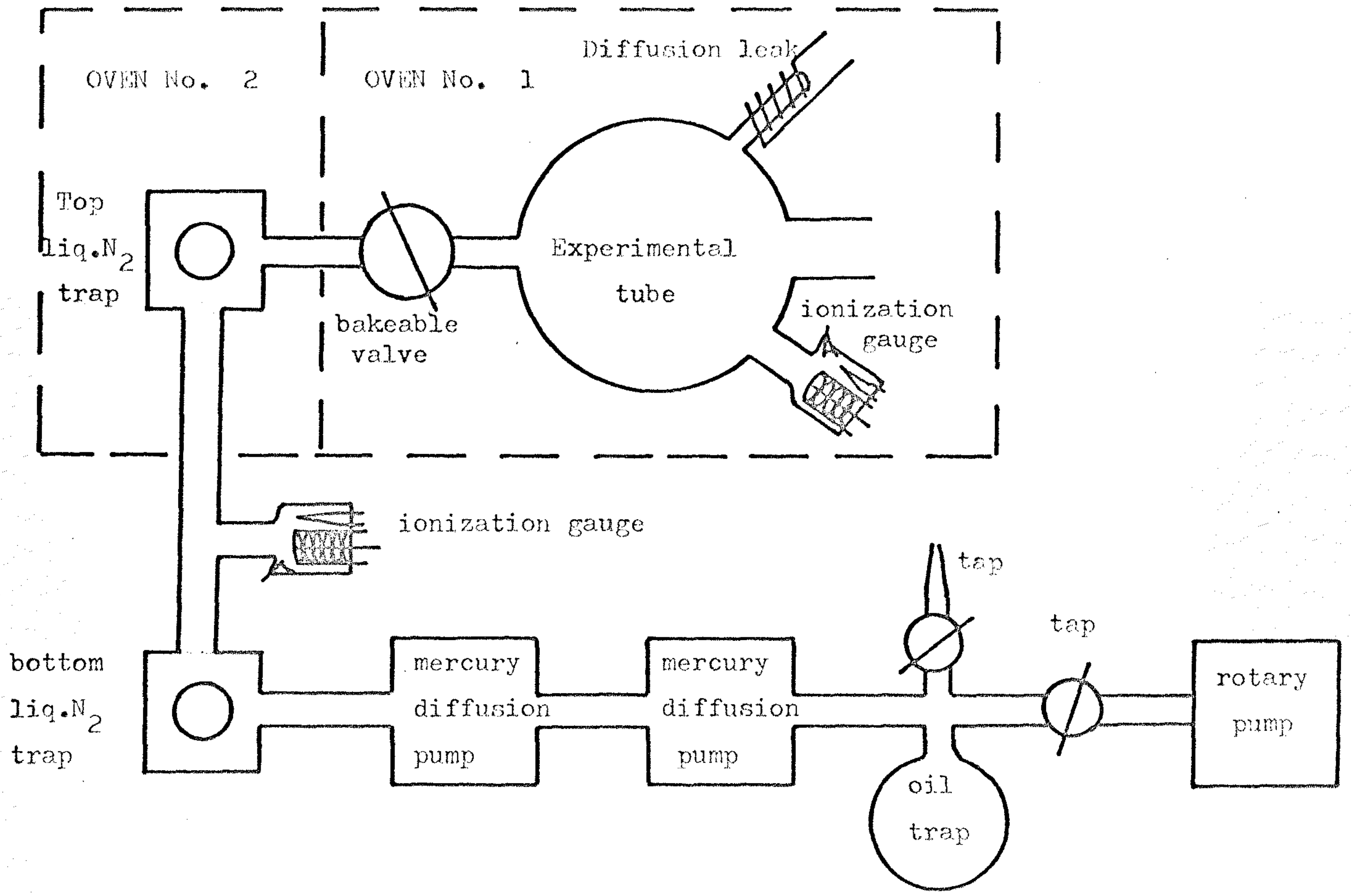

Fig. 19 Schematic diagram of the vacuum systems.

rotary pump and the other as an air inlet valve. The two two-stage water-cooled mercury diffusion pumps were mounted in series above the oil trap and a finger-type liquid nitrogen-cooled trap was mounted above the top pump. This trap was kept permanently cold to prevent mercury contamination of the experimental tubes (and the copper pad of the metal tap). Cooling was by means of liquid nitrogen held in 3-litre spherical dewars which stayed cold for 20-50 hours. The system above this trap was bakeable, apart from an ionization gauge mounted at this point to allow pressure measurements whilst baking the upper part of the system. The second cold trap was bakeable separately by means of a small oven. The larger oven was used for baking the experimental tubes and in the case of the first system the metal tap. The ovens were constructed of 'Viceroy' $\frac{3}{4}''$ 5-ply aluminium and asbestos insulating material[217] supported on lightweight metal frames. The large oven was heated by four 800 watt heater elements and the small oven by one element. Both ovens were able to maintain temperatures of about $350^{\circ}K$.

The use of the metal tap on the first system had a number of advantages. Firstly, the tube could be temporarily isolated from the pumping system during gas adsorption experiments, or during repairs to the rest of the system. Secondly, by observing the tube pressure change on closing the tap, the presence of leaks in the tube could be readily detected. Thirdly, by closing the tap, gases evolved during temporary removal of the top dewar (see sec. 8.2.2) could be prevented from entering the tube. The main disadvantage of the tap was that it reduced the pumping speed of the system. Tubes were connected to the tap by means of a 'Conflat' flange using OFHC copper gaskets. These were found to be very reliable, only one leak occuring across the knife edges, this being for a gasket which had been in use for over fifty bakeouts. Minor scratches and abrasions on the knife edges were found to have no effect on the sealing properties.

8.2.2 Evacuation procedures

Conventional u.h.v. techniques, as reviewed recently by Hopkins[218], were employed during this work. Initial roughing out by the rotary pump resulted in a reduction of the pressure to about 10^{-2} torr after 10 minutes pumping. At this stage, both diffusion pump heaters were switched on and 5 - 10 minutes allowed for the pumps to come into operation. The water cooling systems were left on permanently even when the system was not in operation. After about 10 minutes the pressure fell to $\sim 10^{-4}$ torr and the bottom trap was cooled by raising the liquid nitrogen dewar. One of the ionization gauges was then switched on to monitor the pressure. The rate at which the pressure fell at this stage was dependent upon the initial state of the system. For a 'wet' system (i.e. one which had been open to the atmosphere for several days) the pressure would be reduced to below 10^{-5} torr only after several hours of pumping. For a 'dry' system (one which had been open to the atmosphere for only a short period (hours) since previous evacuation) the pressure would be reduced to as low as 10^{-6} torr within an hour. For either case, when the pressure had been reduced to below 10^{-5} torr the large oven was put in place and switched on, followed, after 15 minutes by switching on the small oven. The pressure during bakeout was monitored by the ionization gauge between the two traps. A pressure rise to as high as 10^{-3} torr (for a wet system) was observed within 30 minutes of switching on the ovens and this fell over a period of hours to below 10^{-6} torr. The duration of the bakeout varied according to the initial state of the system (wet or dry) but was generally about 12 hours. After reduction of the pressure to 10^{-6} torr or lower, the small oven was removed and the top dewar immediately placed in position. Although this involved cooling the glass by some 500°C in a matter of seconds, no fracture of the glass was ever observed. After cooling the top trap the large oven was switched off and removed. The reason for cooling the top trap whilst still hot was that a section of glass between the two traps, (including a gauge) was unbaked. If the ovens were switched off and left for an hour to cool before raising the top dewar experience showed that water vapour from the unbaked section would enter the tube and prevent attainment of the ultimate vacua required. After cooling the tube the pressure fell to about 10^{-8} - 10^{-9} torr. It was then necessary to degas the ionization gauge and all the heatable metal parts of the tube. For tungsten wire electrodes, heater loops, etc., this involved heating to temperatures in excess of 2700^{o}K for periods of up to 2 weeks. During this period, the pressure often remained at 10^{-8}torr due to slowly evolving CO_2 from the liquid nitrogen trap,[219] the vapour pressure of CO_2 at 77^{o}K being about 10^{-8} torr. The CO_2 and other gases accumulated in the top trap were therefore periodically dispersed by dropping the top dewar for periods of 30 seconds to 2 minutes so that the gases could be pumped away[220]. For the system with the metal tap, this was closed during trap warming. For the other systems the electrodes were kept at 2500^{o}K and the tube hot to prevent excessive collection of the evolved gas in the tube. This process often has to be repeated up to a dozen times and it was occasionally necessary to bake the system a second or even a third time to attain pressures of 10^{-10} torr and below.

8.2.3 Pressure measurement and leak detection

Mullard Bayard-Alpert ionization gauges were used for total pressure measurements. IOG-1 gauges (X-ray limit 1×10^{-10}torr) containing two filaments were used for pressure measurements during bakeout. Tube pressures were measured by means of UKG-1 gauges (X-ray limit 5×10^{-11} torr), these gauges having wide-tubulation necks to reduce the degassing time and to prevent the gauges 'ion-pumping' themselves. The gauges were controlled by means of a Vacuum Generators IGP-1 gauge control unit, containing built-in degassing facilities.

Partial pressures were measured by means of mass spectrometry (see sec. 8.2.4)

A number of different methods of leak detection were used. A 'Tesla' discharge coil was used to locate leaks which resulted in a pressure in the system high enough ($\geqslant 10^{-3}$ torr) to support a discharge, the pin-hole being indicated by a concentration of the discharge at this point. At lower pressures the usual procedure was to coat the area suspected of containing the leak with an organic solvent such as acetone or methylated spirit, at the same time observing the pressure. Any sudden change in the pressure, rise or fall, indicated a leak.

The mass spectrometers provided another means of leak detection. The spectrometer was set to register say, argon, and argon was then introduced through a fine nozzle around the system.

On the system with the metal tap, the presence of a leak was generally shown by a steady rise in pressure on closing the tap.

The most common sources of leaks were the tungsten lead-throughs. These were constructed by oxidizing the tungsten to form the black monoxide followed by melting on a pyrex tube, care being taken to eliminate gas bubbles. This was then sealed into a large tubulation on the tube. Leakage paths were often left during these sealing processes and the seals also occasionally leaked due to fractures introduced by meachanical shock or by excessive heating or rapid cooling.

8.2.4 Mass Spectrometry

Two types of mass spectrometer were used during this work.

8.2.4.1 The Varian partial pressure gauge

This instrument, shown schematically in Fig. 20 was of the magnetic deflection type, scanning up to mass 70 a.m.u. in two ranges (1 - 10, 10 - 70). The resolution was sufficient to allow identification of the commonly occurring gases, whilst the sensitivity (10^{-2} amp. torr^{-1}) allowed measurement of partial pressures 10^{-13} torr. Scan times were 30, 100 or 300 seconds and manual operation was possible (as during leak testing). Total pressure measurements could be made by operating the instrument as a simple ionization gauge (X-ray limit 2×10^{-11} torr). The emission currents for total and partial pressure measurements were 1 mA and 6 mA respectively. Facilities for electron bombardment of the grid and collector aided degassing. The head was connected to the system via a $1\frac{1}{2}''$ diameter metal-glass seal, and the whole instrument and magnet were bakeable to 425°C.

8.2.4.2. The E.A.I. 250 quadrupole residual gas analyser

This was a more sophisticated instrument than the Varian spectrometer. As shown schematically in Fig.21 it comprised an ionizer, quadrupole filter and electron multiplier detection system. The atoms or molecules enter the ionizing chamber via a part in the side of the head, and are ionized by low energy (0 - 90 eV) electrons emitted by the filament. The ions then

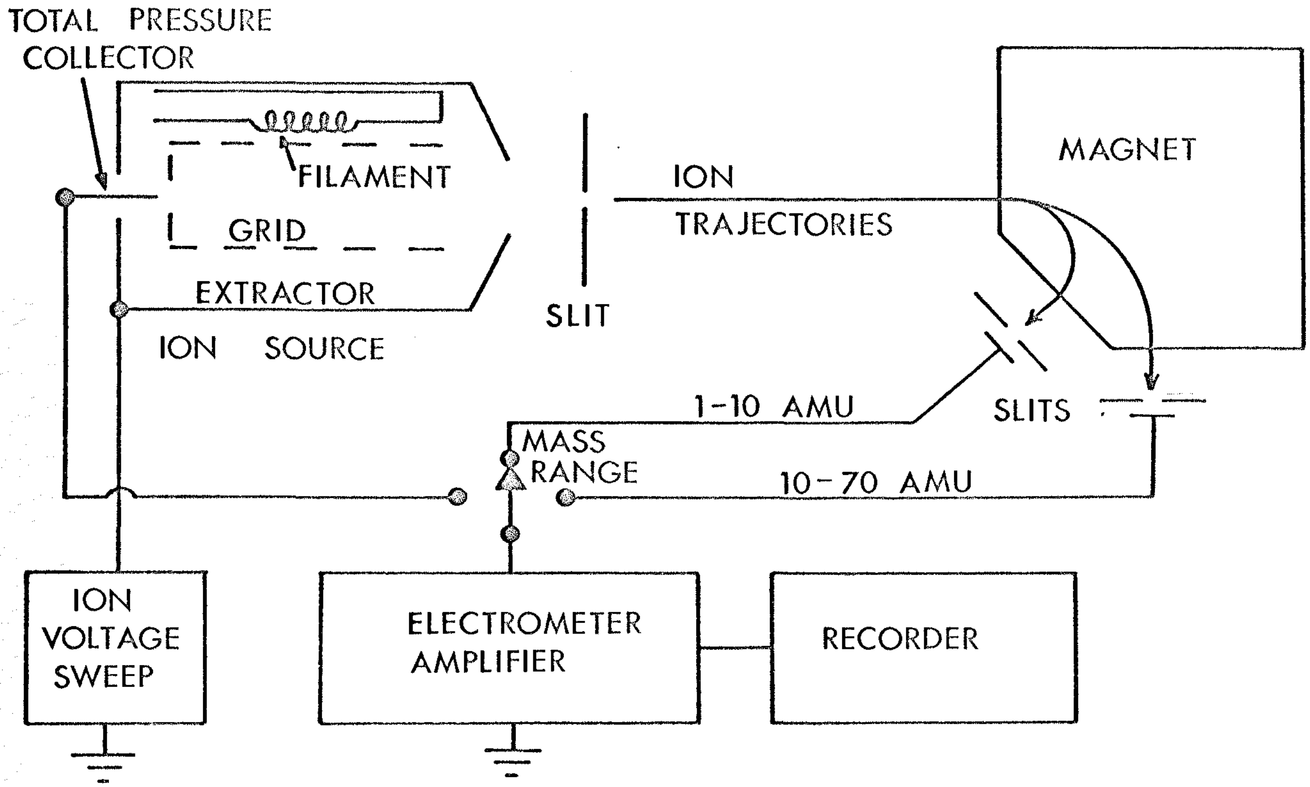

Fig. 20 Schematic diagram of the Varian partial pressure gauge assembly.

pass through three lenses for ion extraction and focussing, and into the quadrupole section. This was composed of four stainless steel filter rods precision mounted on alumina insulators. Ion detection was by means of an electron multiplier comprising 14 copper-beryllium dynodes, the gain being 10^6, and a Faraday cup collector. The collected current was then registered on a Keithley 417 high speed picoammeter and the output fed to an Advance X-Y recorder. The sensitivity was sufficient for detection of partial pressures of 10^{-6} times the total pressure. On the low and medium mass ranges, the resolution[221] was better than 2 times the mass number (100 at mass 50, 300 at mass 150) and on the high mass range better than unity (500 at mass 500). This resolution was controllable, for say mass 85, from 0 to 170. The scan rate was continuously variable from 50 m secs to 30 minutes for each mass range.

Whilst this instrument had the advantages of versatility and excellent resolution and sensitivity, it also had a number of disadvantages. The ionizer construction and electrical connections were unreliable and poorly designed, resulting in constant dismantling of the head. No degassing facilities were incorporated and the pumping speed through the head was very low. Also, some trouble was encountered due to mercury contamination of the multiplier dynodes with a resultant loss in gain.

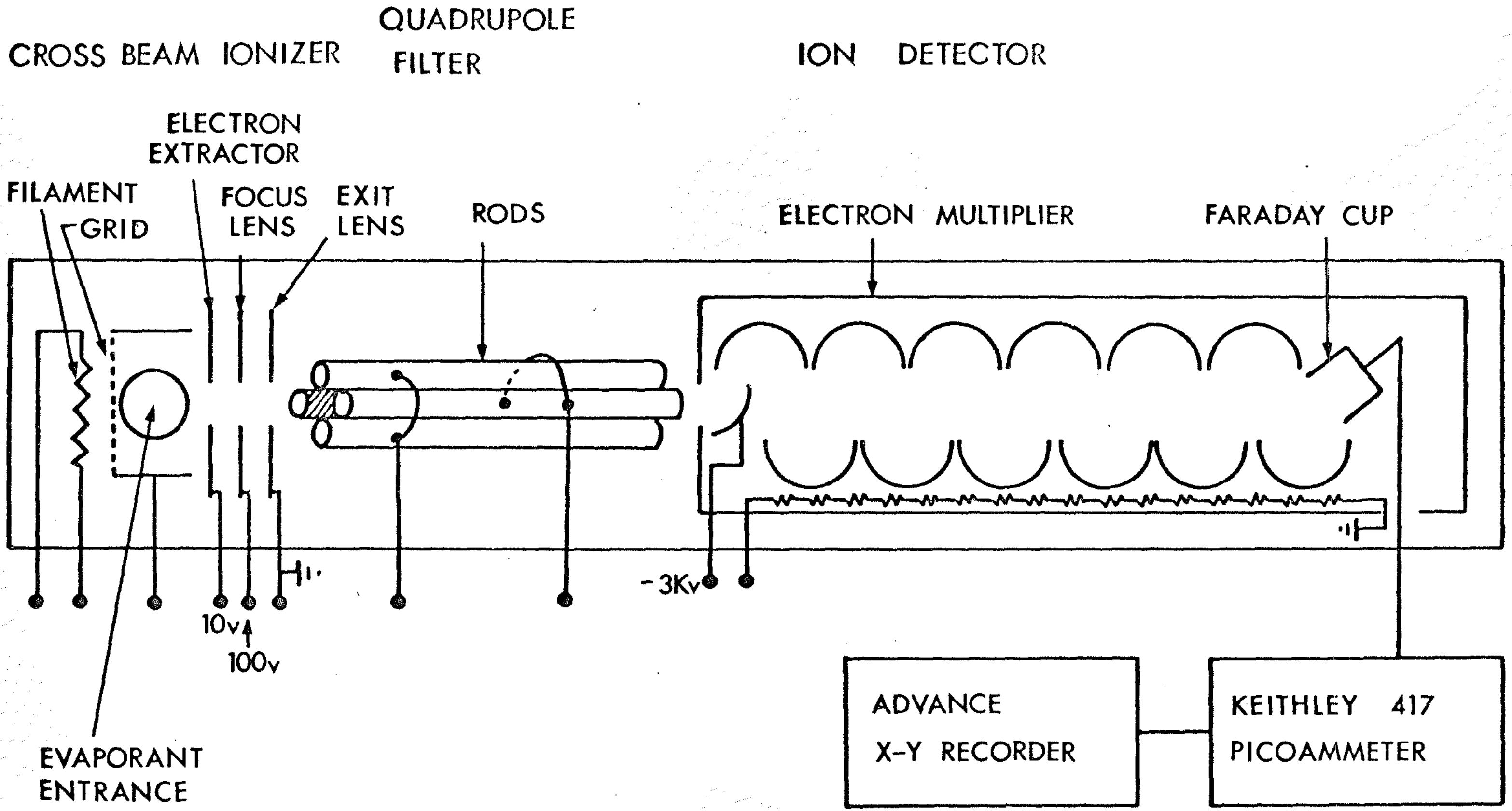

Fig. 21 Schematic diagram of the E.A.I. 250 quadrupole mass spectrometer showing ionizer, filter and detection systems.

8.3 The Experimental Tubes

8.3.1 Tube design (general)

In general the tubes comprised an emitter assembly and a conducting phosphor screen, and an evaporation assembly in the same or a separate bulb, together with the associated shutters, connections and gauge.

The emitter tips were prepared from electro-etched 50 µm dia. Mullard-Blackburn tungsten wire, mounted on a 0.18 mm. dia. tungsten heater loop. Two 50 µm dia. tungsten wires were spot-welded either side of the emitter on this loop for resistivity temperature measurements. The emitter assembly was mounted on a sidearm containing four tungsten lead-throughs (with the exception of tube type A) thus allowing easy emitter replacement.

The stannous oxide conducting screen was deposited by a method described by Gomer[80]. Stannous chloride fumes were blown into the tube which was heated to about 450°C, resulting in oxidation of the stannous chloride on the glass. Typical screen resistances were $10^3 - 10^5 \ \Omega \ m.^{-1}$. The screens had the advantages of being transparent and chemically inert. The screen connections took the form of tungsten coils sprung against the screen and mounted on tungsten lead-throughs. 'Aquadag' colloidal graphite was occasionally applied to ensure a reliable connection.

The fluorescent phosphor screens were deposited on the conducting screen by a method again described by Gomer[80]. A few drops of a solution of 1 part orthophosphoric acid in 20 parts acetone (solvent) were spread on the glass by rolling a dozen 3 mm. diameter glass spheres around in the tube. After removing the spheres the tube was left several minutes for the acetone to evaporate. The thin layer of phosphoric acid left acted as a sticking base for the phosphor which was puffed on using a scent spray. Typical screens were 10 - 50% transparent. The phosphor used was manganese activated zinc orthosilicate (type W204A supplied by Derby Luminescents Ltd.) with an average grain size of 8 µm. The emitted light was emerald green in colour. Screens deposited in this way (the alternative methods being settling in solution and decantation or by eletrophoresis) were completely satisfactory provided that chemical contamination was avoided. Contaminated screens occasionally resulted in the emission of blue or orange light.

Evaporator assemblies comprised a filament of 0.89 mm. dia. tungsten wire mounted on two 'degassing' loops of the same material. These were supported on four 1½ or 2 mm. dia. tungsten rods. The purpose of the 'degassing' loops was to aid the outgassing of the assembly and to prevent heating of the support rods during evaporation. The outgassing procedure was to heat the 'degassing' loops to a temperature in excess of 2700°K for several days. This also resulted in partial degassing of the evaporator filament and the ends of the tungsten rods. The evaporator filament was then degassed using half of each degassing loop (interchanging occasionally). The evaporator could then be operated by using both sides of each degassing loop together so that the temperature of these would be considerably lower than the evaporator filament (which was taking twice the current).

The uranium (or zirconium) was contained in the form of a wire in an adjacent side-arm, mounted on glass supports and having a nickel coil or iron slug mounted at the rear end. The wire was positioned such that it could be moved forward by an external magnet so as to touch the evaporator filament. Heating the filament then resulted in a globule of uranium melting onto the evaporator. The remainder of the uranium was then slid back to be used for subsequent evaporator charges.

It was frequently necessary to shield the emitter or screen or both from the evaporator. This was done by mounting a tungsten shield on a tungsten rod, again with a nickel coil or iron slug on the end, in an appropriately placed sidearm. Such shutters could be slid back and forth or rotated.

An ionization gauge was always mounted close to the evaporation source to monitor any pressure change during evaporation. The glass tubulation to this gauge was kinked to prevent deposition of uranium or zirconium in the gauge, and subsequent shorting-out of the electrodes.

8.3.2 Operation of the tubes and experimental procedure

A tube was considered to be fully outgassed when all electrodes could be raised to above their operating temperatures (2100°K for the evaporator filament) for 30 minutes without the pressure rising to above 2×10^{-10} torr. This often involved 2 - 3 weeks degassing for a new evaporator assembly or for degassing the Varian mass spectrometer. Tip assemblies could generally be degassed in less than an hour. The ionization gauge was left degassing (with the grid and collector raised to ~ 1200°K) throughout the period of degassing the other electrodes.

Prior to this extended period of degassing the emitter was tested for emission symmetry and suitability. After baking, when the pressure had fallen to 10^{-8} - 10^{-9} torr the emitter was heated briefly (~5 minutes at 2300°K) to smooth the surface. A positive potential was then slowly applied to the screen with the emitter earthed via a 10^8 Ω protective resistance. A suitable emitter showed the (110) oriented symmetric pattern shown schematically in Fig. 16 and had an emitter radius of 2000 - 5000 Å, resulting in working potentials of 2 - 7 KV. Tip radii were calculated by measuring the potential required for 10^{-5} amp. emission and using Drechsler and Henkels equation[222].

The emitter temperature was then calibrated in terms of d.c. heater loop current. The heater current was supplied by an International Electronics 30/30/5 power supply. The potential across the two 50µm 'sensing' leads was measured with a Solartron 1440 digital voltmeter (input impedance 20,000 MΩ). The room temperature resistance was determined by passing a d.c. heater current 50 mA. The variation in resistance of the monitored section of heater loop was then determined for temperatures up to 2700°K (typically 4 amps heater current). The temperatures were determined from the resistance by consideration of the temperature coefficient of resistance of tungsten[223]. Van Oostrom[149] has discussed the accuracy of this method of temperature measurement. The error in the calculated values is thought to be ± 20°C in the present case.

After thorough outgassing the uranium (or zirconium) was melted onto the evaporator filament. This was then degassed by heating briefly (~ minutes) to temperatures in excess of 2400°K (for both uranium and zirconium), followed by prolonged degassing at 2000°K until the pressure (hot) fell to 10^{-10}torr. Reduction of the pressure was aided to some extent by the gettering action of these metals, particularly the zirconium which sorbs all common non-inert gases.

After complete degassing of the uranium or zirconium and the emitter, the tube was ready for measurements to be made. For measurements of the total emission characteristics the circuit shown in Fig. 22 was used. The high voltage supply was operated by a remote control 10-turn helipot, the output voltage being measured by a Solartron 1440 digital voltmeter tapped across a 10^4 Ω resistor in series with a 10^8 Ω resistance. Emission currents were measured with a Vibron 33B or 33B-2 electrometer, in series with a 10^8 Ω protective resistance. Details of the circuit used with tube type G (for measurements on single crystal planes) are given in the following chapter.

Work function/coverage measurements were preceded by thermally cleaning the emitter (1 minute at 2500°K), the criterion for cleanliness being reproducibility in the current-voltage characteristics. After heating, the emitter was allowed to cool for 30 seconds before applying a potential. A set of Fowler-Nordheim data was then taken for the clean emitter by measuring the voltages required to draw about 6 emission currents in the 10^{-9} - 10^{-7} amp range. In general, only one current range was used for a given set of readings. The emission pattern was also photographed (see sec. 8.4). Uranium (or zirconium) was then evaporated onto the emitter for a period of from 5 seconds to 2 minutes, the most suitable evaporation time being found by trial and error. The voltages required to draw the same emission currents were then redetermined and the emission pattern photographed. This procedure was repeated as required. During heat-treatment

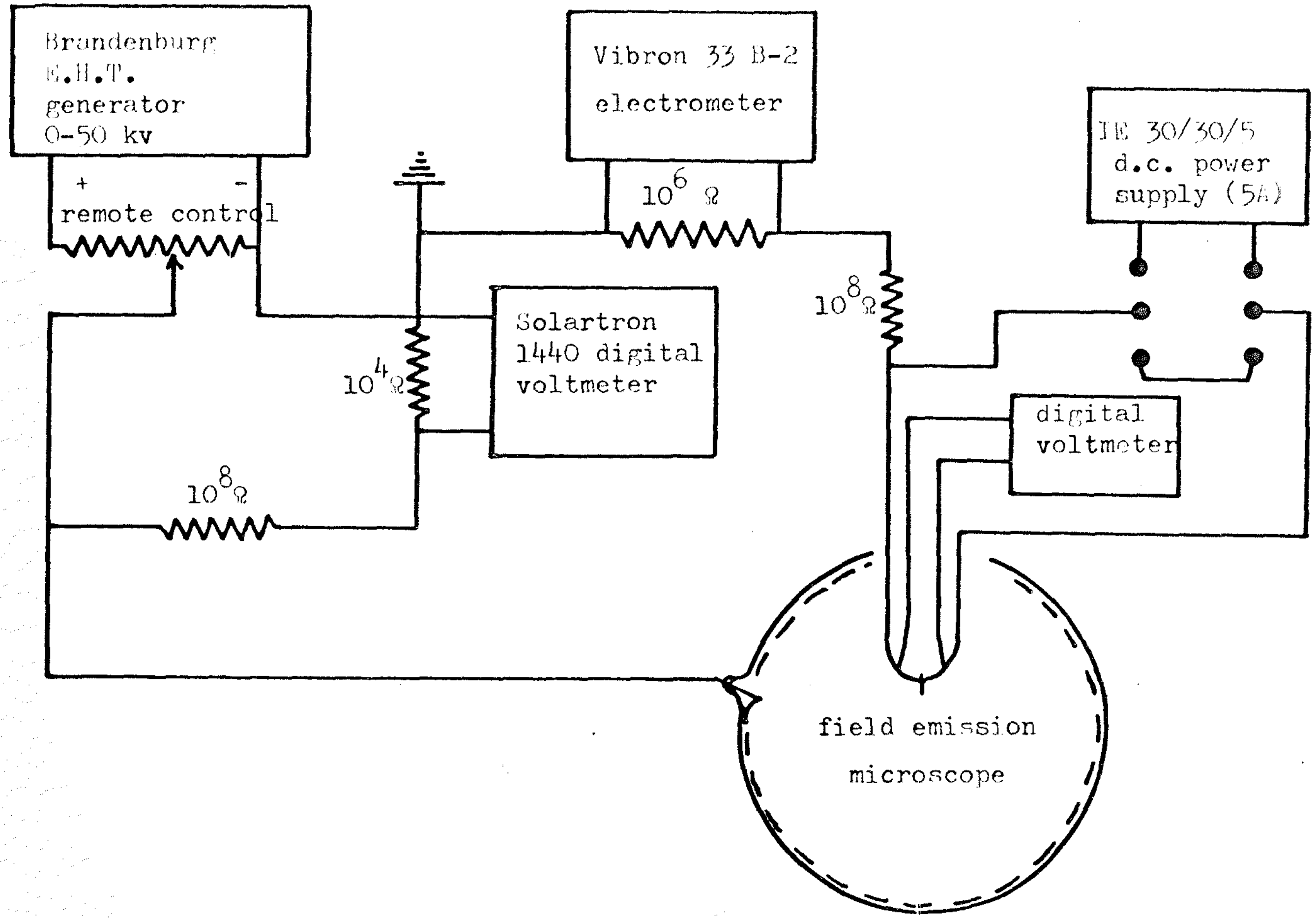

Fig. 22 Schematic diagram of the circuit used for total emission measurements.

measurements the emitter was heated to a given temperature, usually for a period of 60 seconds, then left to cool for 30-60 seconds prior to recording a set of Fowler-Nordheim data and photographing the emission pattern. The ionization gauge was switched off during all emission measurements.

Experimentation could usually be continued until the evaporator filament burnt out. This was generally after evaporating 3 or 4 uranium or zirconium charges and as many as 60 experimental runs were performed with a given evaporator filament.

8.4 Photography

Recording of the emission patterns was by the use of a Canon FP f 1.2 35 mm. SLR camera mounted for rigidity on an optical bench or a tripod. Various films were tried, in particular Gaevert Scopix G (H.D. and I.S.), Kodak Tri-X and Ilford Mark V motion picture film were all found to be satisfactory. However, the majority of the work was performed using Ilford FP3 (125 A.S.A.) this being entirely suitable with regard to speed, resolution and sensitivity to green light. Exposure times varied from $\frac{1}{2}$ second to 3 seconds at f 1.2.

CHAPTER 9

Results and Discussion - Uranium

9.1 Introduction

As discussed in previous chapters the initial experiments were concerned with the measurement of the average work function as a function of coverage (up to $\theta = 2$) and heat-treatment with a view to verifying the existence of and explaining the mechanisms of the irreversible changes observed by previous workers. Described below are the experimental tubes constructed for this purpose and the results obtained from them. Also described are the subsequent tubes used for measurements on thicker layers, single crystal planes and mass spectrometric analyses, together with the results obtained.

A summary and discussion of these results is given at the end of the chapter.

9.2 Monolayer and sub-monolayer films

9.2.1 Preliminary results - Type A tubes

The first design of tube used was of a type described by Montagu-Pollock and Rhodin[224] but with a modified evaporation source. These microscopes were constructed initially by T.W. Wingent Ltd. A schematic diagram is shown in Fig. 23. The instrument was originally designed as a field-ion microscope

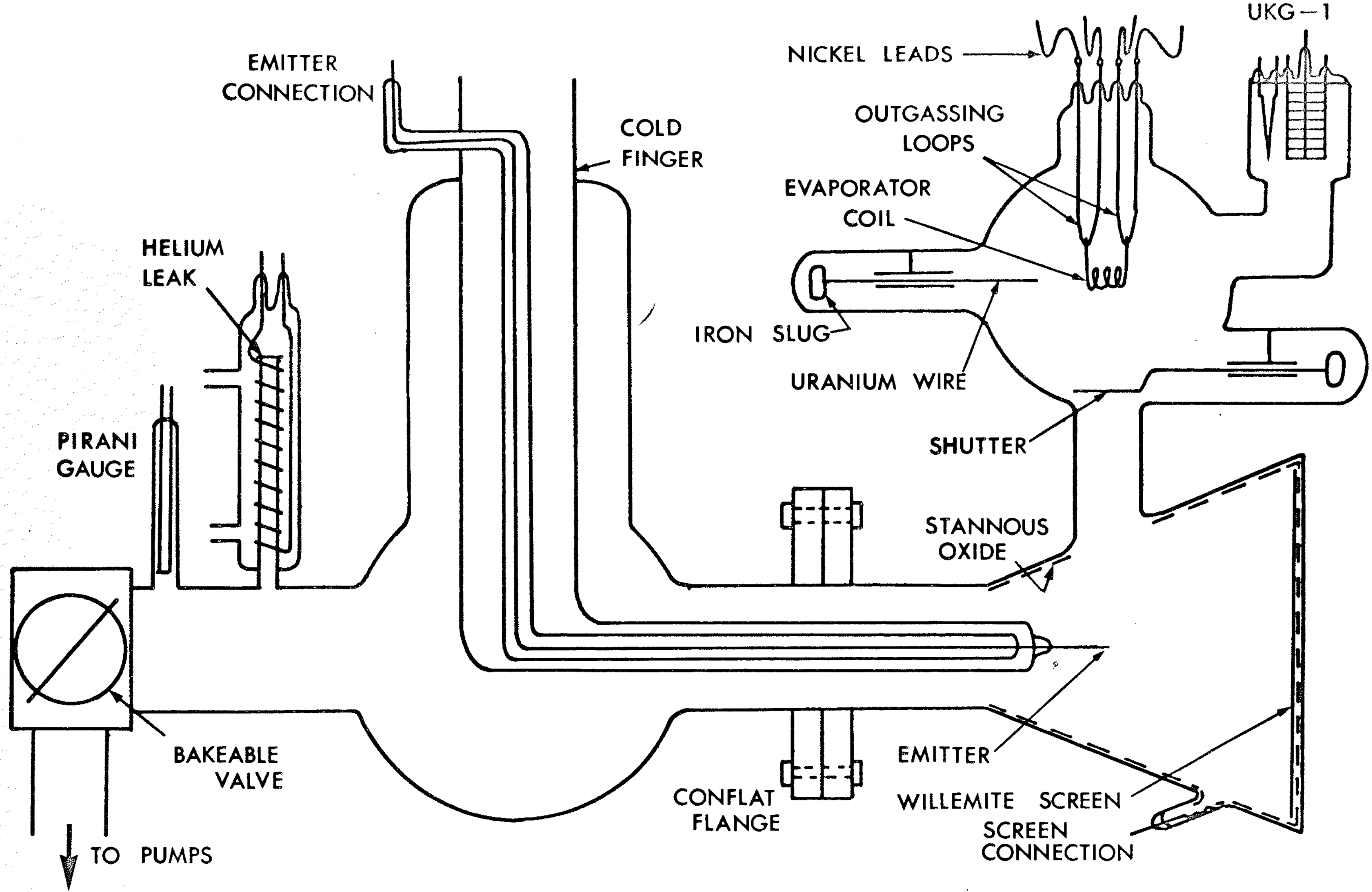

Fig. 23 Tube type A.

with a small evaporator coil mounted about 3 cm above the emitter and 3 cm in front of it. However, because of the rigorous outgassing procedure required for uranium it was considered impractical to use this evaporator set-up as an intricate system of shutters would be required to prevent contamination of the emitter and phosphor screen. The evaporator assembly was therefore housed in a separate bulb directly above the emitter, as shown in Fig. 23.

Using three tubes of this design, preliminary measurements were made on about 15 emitter tips. These measurements concerned not only the work function variations with coverage and heat-treatment, but included investigations of the effects of progressively degassing the uranium (varying the degassing period and temperature) and the effects of gas contamination, i.e. measurements taken at pressures in the 10^{-9} - 10^{-7} torr range. Experiments were also performed to observe the effects of varying the measurement techniques (e.g. by taking Fowler-Nordheim plots over several orders of magnitude of current) and the optimum photographic procedures were determined.

With regard to the actual measurements made with these tubes, a number of difficulties were encountered resulting in modifications having to be made in the following tubes. Firstly, a number of minor difficulties arose as a result of the tube design. In particular, the pumping speed through the tube was very low so that it was difficult to attain and maintain the required vacua. This was improved to some extent by replacing the initial 1" bore conflat flanges by flanges with a $1\frac{1}{2}$" bore. Furthermore, the microscope construction, which resulted in the flanges having to be tightened whilst supported only by the adjacent glass, was extremely fragile and breakages were quite common. The most serious problem however, arose from the positioning of the evaporation source. By mounting the evaporator above the emitter it meant that the tip could only be shadowed from above and half the emitter directly covered. Since overall average work function measurements would only be meaningful for a symmetrical adsorbate distribution over the emitter planes this meant that the uranium would have to be spread by heating after each deposition. Attempts to spread sub-monolayer deposits however, indicated that spreading in a sensible time ($\leq$ 60 seconds) only occurred at temperatures in excess of 1100°K. This meant that only the high temperature γ - uranium phase could be studied.

Measurements were therefore made together with the effect of heat treatment in the range 1100 - 2200°K. These preliminary results indicated that uranium deposited on tungsten at 1100°K caused a decrease in the work function to 3.19 eV followed, with increasing coverage, by a rise levelling out at 3.43 eV. No differences were observed between films deposited on the heated emitter and those deposited on a cold emitter and then heated. It was further found that on heating the deposit for 60 second periods to progressively higher temperatures, the deposition curve was approximately retraced, reaching the minimum of 3.19 eV at about 1600°K, and the clean value of 4.50 eV at 2050°K.

Measurements for variously degassed evaporation sources indicated that the outgassing procedure was critical in obtaining reproducibility. It was found that only by heating the uranium to 2500°K could cleanliness of the evaporant be ensured. This is in agreement with the observations of Ackermann et al[210] concerning the removal of oxygen from uranium metal. Measurements at higher pressures resulted in higher work function values being obtained.

Varying the measurement techniques indicated a number of factors which had to be observed during later measurements. It was found that the Fowler-Nordheim plots deviated from linearity if measurements were extended to currents as high as 10^{-6} amp, or were made over several current ranges. Plots were therefore taken subsequently over only one current range, generally 10^{-9} - 10^{-8} amp.

The photographic techniques were also simplified to those described in sec. 8.4.

9.2.2 Tube type B

The initial attempt to rectify the problems encountered with the type A tubes is illustrated in Fig. 24. In this tube the emitter was simply tilted through 90° so as to face the evaporator directly. Deposition was thus along the axis of the emitter resulting in a symmetrical adsorbate distribution and removing the necessity of heating the deposits for spreading. Also the lack of constrictions in the tube resulted in a higher pumping speed than with the type A tubes and hence easier attainment of ultra-high vacuum. The main disadvantage was that a phosphor screen was not included so that the emission patterns could not be observed. With the absence of a conducting screen the anode took the form of a 2 cm dia. tungsten loop about 2 cm above the emitter. This was mounted on two tungsten lead-throughs so that it could be degassed by direct heating. Failure to degas the loop resulted in gas desorption from the anode surface due to electron bombardment during emission and consequent contamination of the emitter.

With this tube measurements were made on the variation of work function with coverage and heat-treatment for uranium deposited at various temperatures in the range 295°K to 1300°K. In view of the fact that the adsorbate distribution could not be observed, these results were also regarded as preliminary and therefore are not given in detail. Briefly, the findings

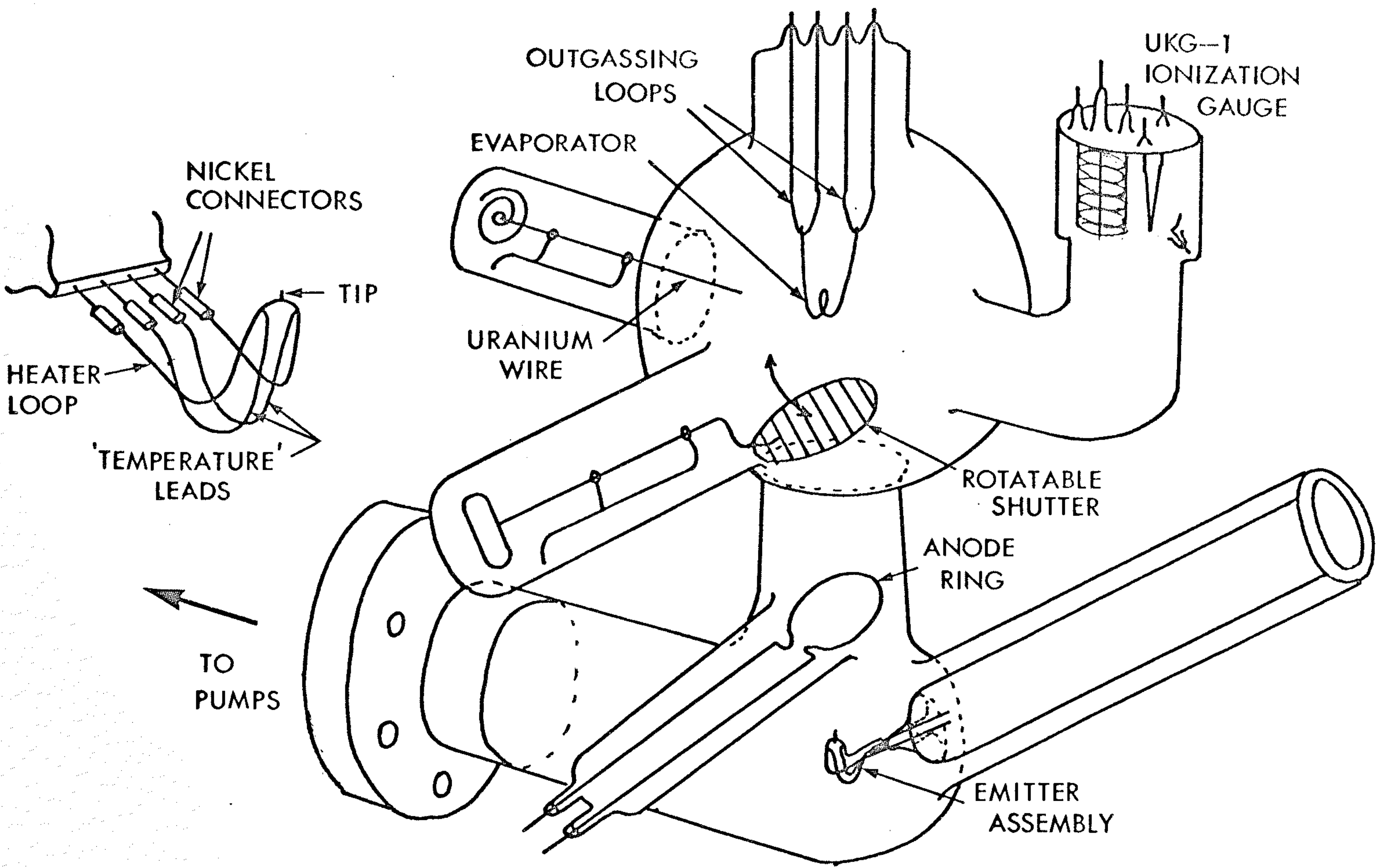

Fig. 24 Tube type B.

from the previous tube for the temperature region above 1100°K were verified. Also, work function/coverage curves were obtained for deposition at 295°K and 1000°K, the curves reaching minima of 3.37 eV and 3.31 eV, and levelling out at 3.60 eV and 3.53 eV respectively. Heat treatment of monolayer (see sec. 9.2.3.2) deposits showed decreases in the work function at the phase transition temperatures as noted by the previous workers.

Having verified these irreversible changes and having made work function/coverage measurements for the three temperature regions, it was decided to abandon this tube in order to combine the work function measurements with observations of the corresponding emission patterns.

9.2.3 Type C tubes

Two microscopes were finally constructed which allowed evaporation onto the end of the emitter and also allowed observation of the emission patterns. This microscope design is shown in Fig. 25. The emitter was mounted in the centre of a 1 litre pyrex bulb, the front surface of which was coated with conducting and phosphor screens in the usual way. However, the evaporation assembly was housed in a separate $\frac{1}{2}$ litre bulb, deposition being through a narrow tube in the centre of the phosphor screen. This avoided undue masking of the emission patterns. The emitter and evaporator filament were aligned through this thin tube. A separate larger tubulation joined

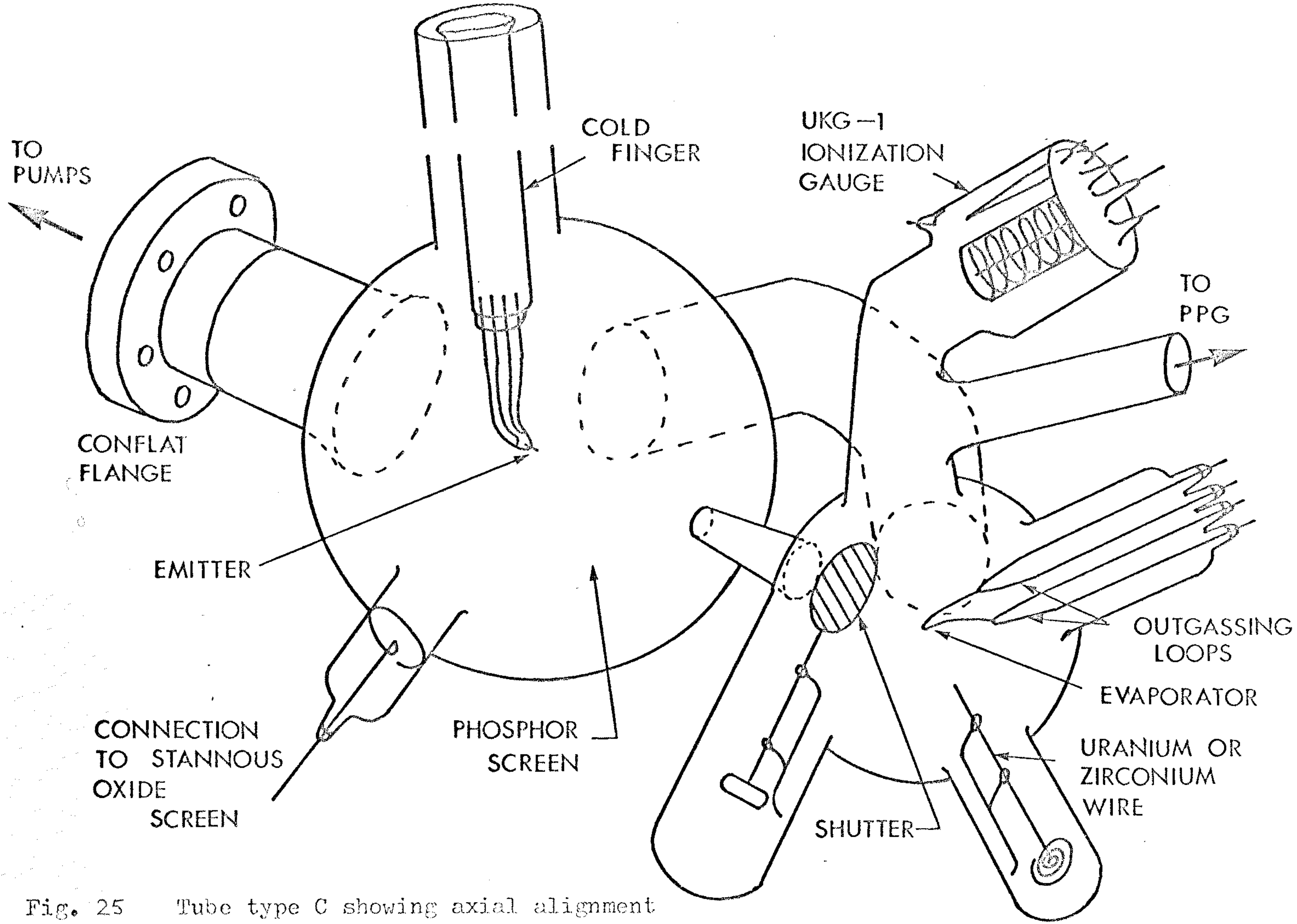

Fig. 25 Tube type C showing axial alignment of emitter and evaporator filament.

the bulbs together to increase the pumping speed from the evaporation bulb.

This type of tube was found to be suitable for all the required measurements in the temperature range from 295°K to 2200°K.

9.2.3.1 Results from the type C microscopes

The variation of work function with coverage was found to depend on the temperature of the substrate during or after deposition (in agreement with the A and B type tube results). Three distinct states were observed and typical deposition curves are shown in Fig. 26. The coverage scales have been normalised to the minimum work function points, since subsidiary experiments showed that at the minimum of the low temperature curve it was possible to transfer to the minimum of each higher temperature curvesby heating to the appropriate temperatures. The actual times of deposition to this minimum were 12.8 min., 5.8 min., and 18.3 min. for curves A, B and C respectively. Minimum and final work functions for the curves are shown in Table 2.

Although there was a reproducibly marked difference in curves A and B, no difference could be discerned in the field emission patterns. Fig. 27 (A-C) shows the patterns recorded at the work function levels 4.23 eV, 3.37 eV (minimum) and 3.60 eV (final value) in Fig. 26A. These patterns were also characteristic of Fig. 26B. Initially the deposit formed

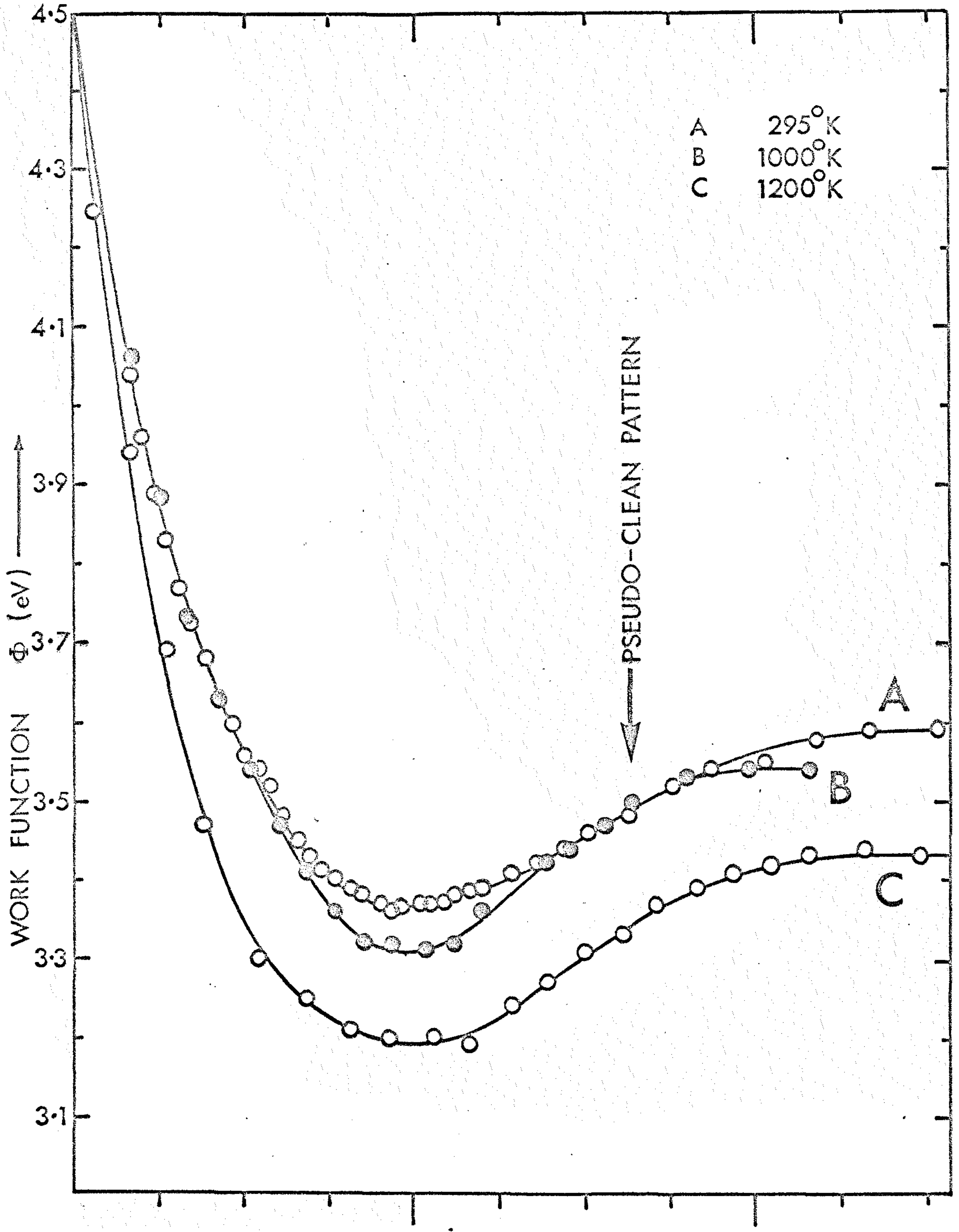

Fig. 2.6 Plots of average work function measured at room temperature against normalised deposition time for uranium deposited (A) at 295°K, (B) at 1000°K and (C) at 1200°K.

Curve (fig.26)	Substrate temp. during deposition (^{o}K)	ϕ_{min} eV	ϕ_{final} eV
A	295	3.37 (fig.27B)	3.60 (fig.27C)
B	1000	3.31 (fig.27B)	3.53 (fig.27C)
C	1200	3.19 (fig.27E)	3.43 (fig.27F)

TABLE 2

Summary of ϕ_{min} and ϕ_{final} for the three adsorption states of uranium on tungsten.

A

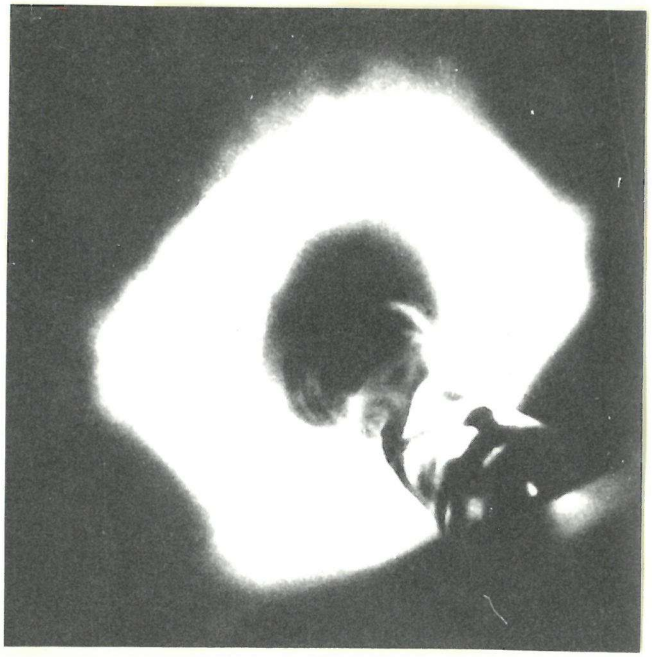

B

C

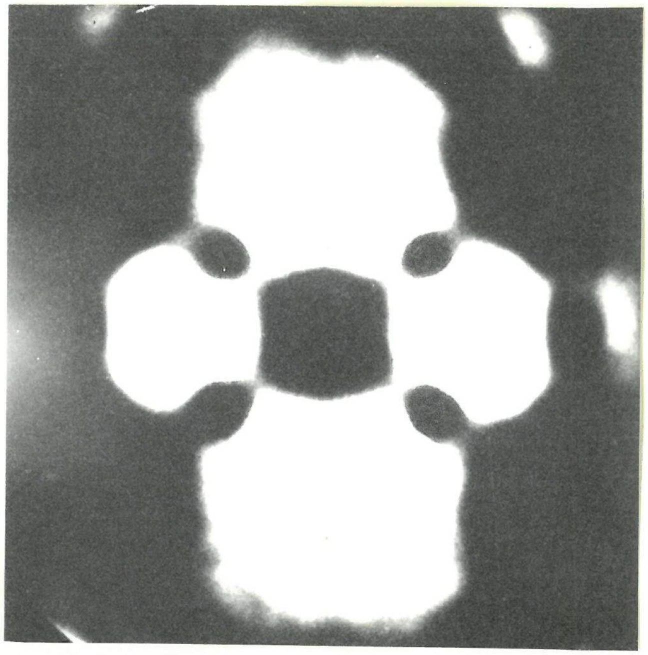

D

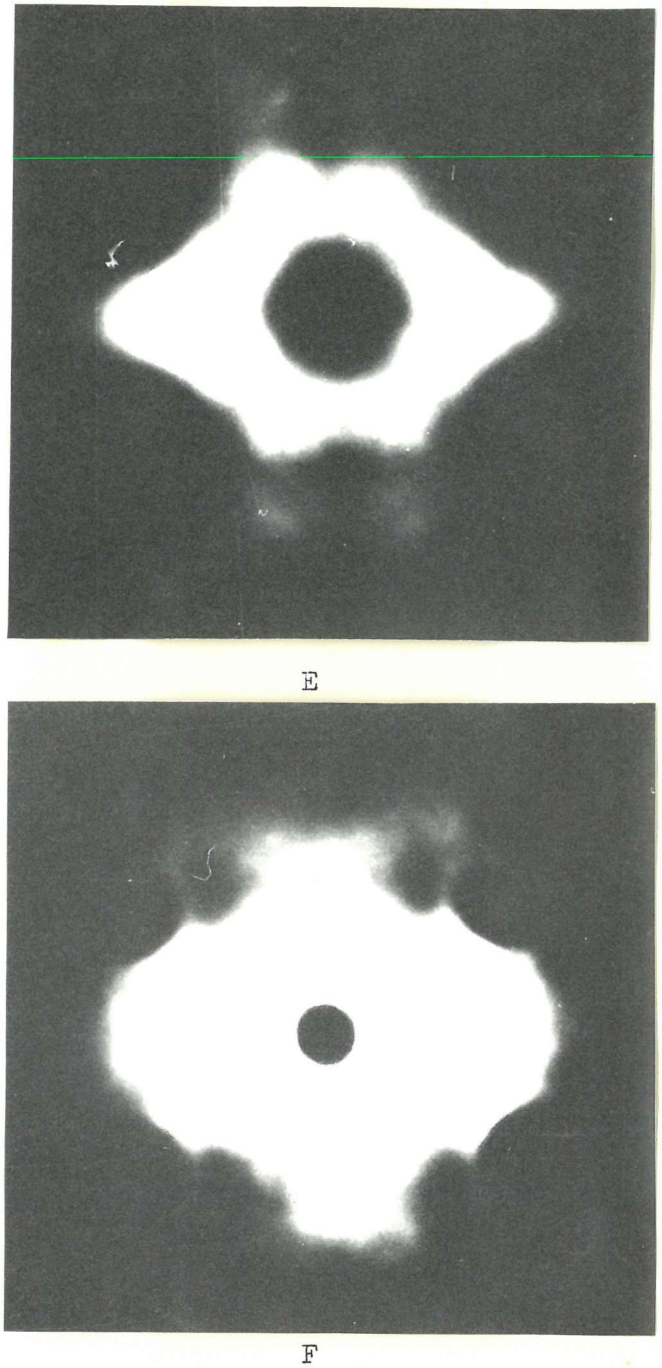

Fig. 27 Field emission patterns of uranium deposited on tungsten at 295°K (A-C) and 1200°K (D-F): (A) $\phi = 4.23$ eV; (B) $\phi = 3.37$ eV; (C) $\phi = 3.60$ eV; (D) $\phi = 3.46$ eV; (E) $\phi = 3.19$ eV; (F) $\phi = 3.43$ eV.

irregular clusters on all planes except the (110) which appeared dark and the (112)'s on which were formed a small number of aggregates, larger than those observed on other planes (Fig. 27A). Figs. 27B and 27C show the establishment of a more uniform distribution as the coverage increases.

All attempts to observe reversibility by slow or prolonged cooling were unsuccessful, it being impossible to return to curve A after the deposit had been heated above 940°K. If a number of depositions were made at, say 1100°K, then the curve would follow Fig. 26C. If then a number of depositions were made at 295°K, the work function values would lie between curves 26A and 26C becoming closer to 26A with each successive deposition at 295°K. Heating to 1100°K at any point would result in a return to curve 26C.

A few measurements gave work function values as low as 2.9 eV, although the pressure remained below 2×10^{-10} torr. Further outgassing resulted in progressively higher values until the consistent values of Fig. 26 were obtained. Presumably the lower values referred to contaminated uranium.

Fig. 26C and Table 2 show a typical set of data for curves recorded after temperature treatments in the range 1050 - 1300°K. In the lower part of the temperature range, the deposit was still somewhat granular, but above 1100°K appreciable migration had occurred and the deposit appeared smooth. Fig. 27 (D-F) shows emission patterns for points on curve 26C at 3.46 eV, 3.19 eV and 3.43 eV.

The behaviour of the uranium deposit when subjected to heat treatment for periods of 60 seconds at successively higher temperatures is shown by plots such as those in Fig.28. Fig.28A is satisfactory with regard to the vacuum conditions and the work function values agree with the deposition curves (Fig. 26), but insufficient experimental points were measured. Fig.28B clearly shows the existence of three levels, but the work function values are not in good agreement with Fig.28A presumably as a result of slight gaseous contamination. Further evidence for the part of the curve above 1100°K is supplied by many separate plots obtained after deposition of uranium at 1100°K, followed by heat treatment and thermal descrption.

It can be seen in Fig.28 that the work function remains constant up to 940°K where it drops by 0.08 eV at which value it remains until it drops again at 1040°K by about 0.1 eV. On further heating above 1200°K the work function begins to drop again, reaching a minimum of 3.19 eV at 1600°K, and then increasing until the clean tungsten value is obtained at 2050°K. Plots such as these were taken for various initial coverages, the work function changes always occurring at the same temperatures and in the same sense.

During thermal desorption the uranium is mobile on the

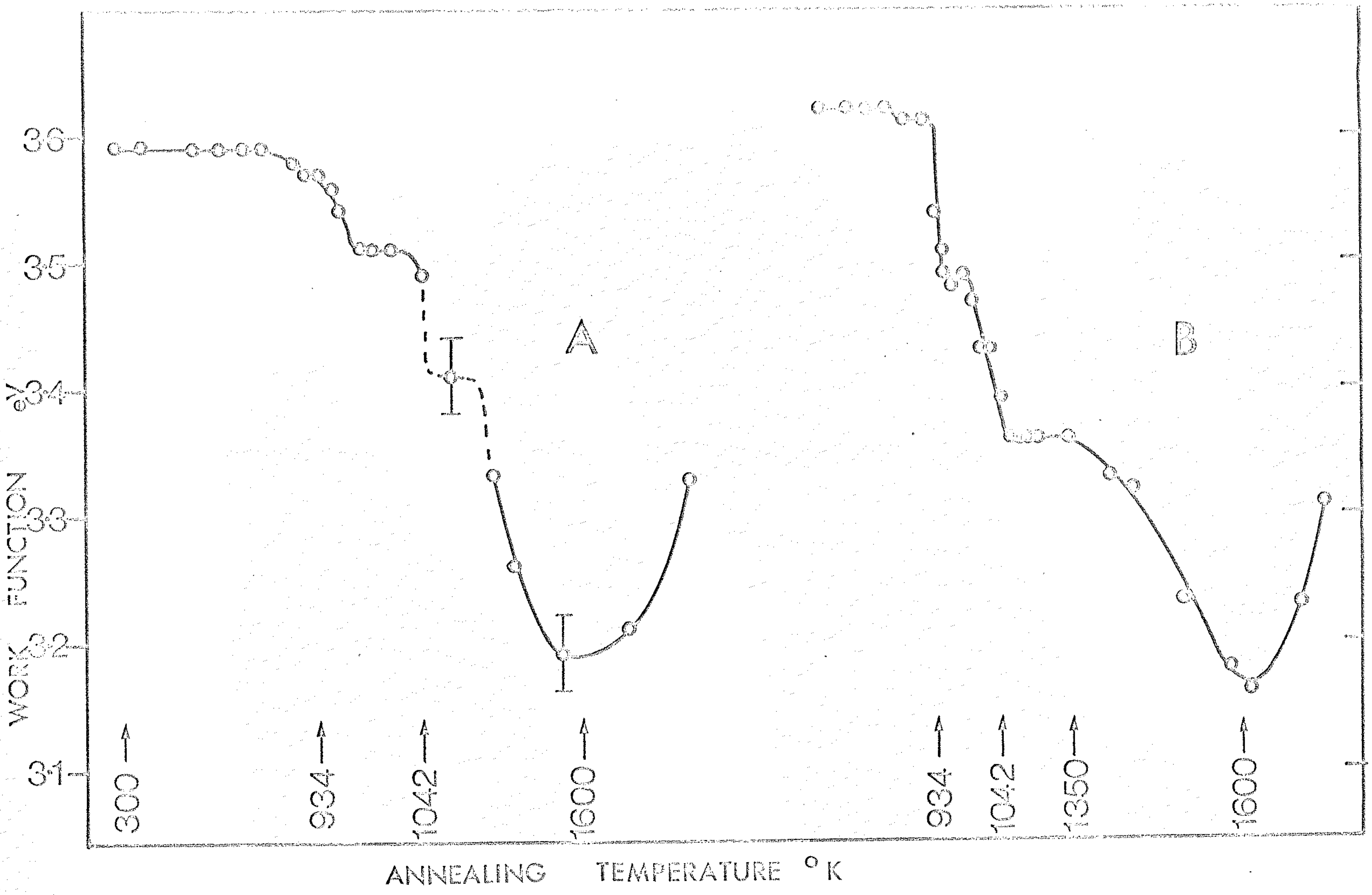

Fig. 28 Plots of work function against heat treatment temperature for monolayer deposits of uranium heated to progressively higher temperatures for periods of 60 seconds.

surface and Fig. 29 shows the distribution patterns during desorption of an initial deposit of about 0.3 of a monolayer. Fig. 29A shows the distribution after deposition at 295°K. This distribution was unchanged after heat treatment up to 1042°K. Above this temperature, surface migration became appreciable and Fig. 29B shows the onset of migration after heating to 1050°K. The (112) planes now appear darker. Fig. 29C shows the deposit after dispersion of the aggregates and migration to the higher index planes, the work function having fallen to a minimum. Fig. 29D shows the distribution after the onset of appreciable thermal desorption (1800°K) and indicates that the uranium is retained longest on the high index planes, in particular the (116)'s.

9.2.3.2 Discussion

The above results indicate that uranium adsorbed on tungsten exists in one of three clearly defined states, dependent upon the temperature to which the uranium has been heated, and further that changes to a higher temperature state are irreversible, at least for films of less than two monolayers thickness.

The final work function values given in Table 2 may be compared with the more recent of the previous measurements given in Table 1 (Chapter 6). The agreement with the contact potential difference work of Barry et al, and the photoelectric work of Lea and Mee, and Fry and Cardwell, is surprising in view of the differing assumptions made with regard to substrate geometry

A

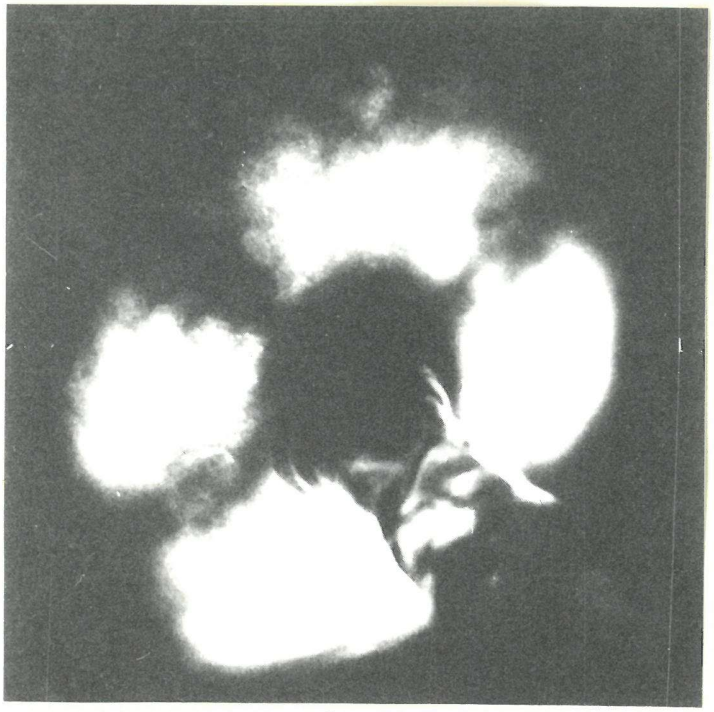

B

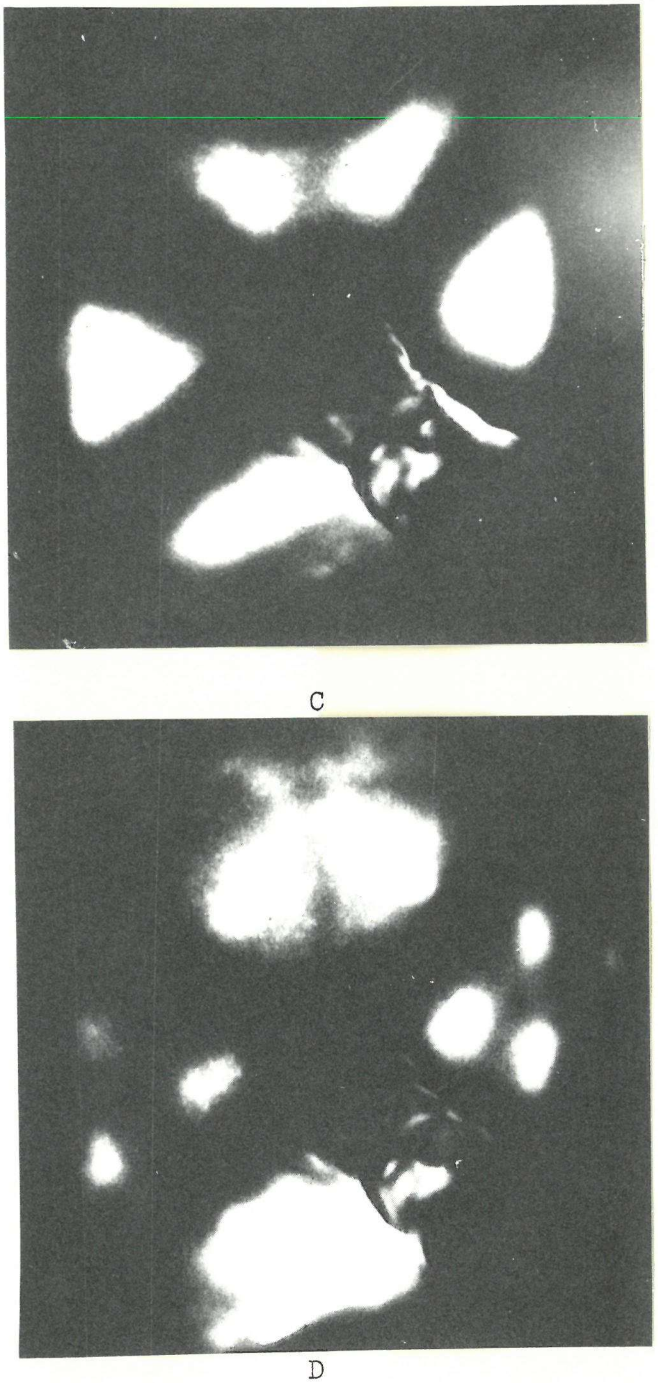

C

D

Fig. 29 Emission patterns of a 1/3 monolayer deposit of uranium heated for 60" progressively to (A)295°K,(B)1050°K,(C)1600°K and (D)1800°K.

and the weighting given to the different crystal planes.

Further, whilst the outgassing and deposition techniques adopted in the present work were similar to those adopted by Lea and Mee and Barry et al, the outgassing procedure followed by Fry and Cardwell (heating to 1250°K for 1000 hours) was not, according to Ackermann et al[210] sufficient to remove all oxide contamination.

Rauh and Thorn measured the work function at a coverage of 15 (on the scale of Fig. 26) as 3.47 eV, and at a coverage of 3 as 3.1 eV, the measurements being made at 1240°K. Correcting these values to the effective work function[112] yields, respectively 3.47 eV and 3.41 eV, in good agreement with the present work.

The present low temperature results do not agree with those of Rivière, although some difference might be expected as the latter work involved much thicker films.

Whilst there is a general agreement with the work function values obtained by other workers, it is of interest to note that even better agreement is obtained if a value of 4.54 eV is assumed for the overall average work function of the emitter, as suggested by Van Oostrom[149].

A notable difference between the present low temperature curves (Fig. 26) and the results of Barry et al is that curve 26A lies above curve 26B, i.e. heating always produces a decrease in work function. This was confirmed by heating films of varying thicknesses, the observed work function changes always being in the same direction. Barry et al, however, observed that their room temperature curve was below their 950 - 1040°K curve up to their monolayer point where the curves crossed over. At this point the work function had risen to 3.49 eV at a coverage of about 1.7 times that for the work function minimum. It is seen in Fig. 26 that curves A and B coincide at approximately this same point (ϕ = 3.49 eV and coverage = 1.7). Furthermore, the emission patterns observed at this point exhibit the pseudo-clean tungsten pattern observed with many adsorbates[70,78] and which Schmidt and Gomer have suggested may correspond to a single chemisorbed layer. This seems the most suitable, if somewhat arbitrary, point to define the monolayer position.

As pointed out by Barry et al the crossing of their curves may have been a consequence of the particular averaging over patches inherent in the Kelvin technique and thermionic or field emission would be liable to yield different results.

Examination of Fig. 27A shows clearly that uranium deposited at 295°K forms clusters or aggregates. This is consistent with Rivière's suggestion that microcrystallites are formed and with the experimental observations of Good and Muller using field emission techniques. Formation of such aggregates requires sufficient energy to allow surface migration, and since no further migration was observed when the substrate was heated to temperatures up to 900°K, it must be concluded that the kinetic energy of the incident beam was an important parameter. Such behaviour has been observed previously for copper on tungsten below 300°K [110]. Further discussion of this point is given in Chapter 10.

That the emission patterns in Figs. 27 A-C were also characteristic of uranium deposited in the range 950 - 1040°K suggests that the difference in curves 26A and 26B is not due to gross surface migration, but may result from some rearrangement of the atoms. That the differences in curves 26 A-C are not due solely to surface migration is also suggested by the abruptness of the work function changes in Fig. 28. Figs. 27 D-F show that thermal migration and smoothing of the deposit has occurred for the high temperature state, and therefore curve 26C may be expected to deviate from 26A and 26B.

From the above findings, therefore, a tentative adsorption model is suggested. The aggregates formed during deposition at room temperature may be expected to be randomly oriented orthorhombic microcrystallites as suggested by Rivière. Heating above 934°K causes an atomic rearrangement which may be related to the α - β phase transition in the bulk metal. The irreversibility, which is not characteristic of the bulk metal, indicates that the uranium-tungsten interaction is of some importance in this change, but also, the non-divergence of curve 26A from 26B at coverages of less that $\frac{1}{3}$ of a monolayer indicates a minimum uranium concentration necessary for the transformation. The transformation must therefore involve both uranium-uranium and uranium-tungsten interactions. The onset of appreciable thermal rearrangement at 1100°K, indicated by the distinct emission patterns, is sufficient to account for the deviation of curve 26C from curves 26A and 26B. However, although it cannot be inferred from the present measurements, the formation of another crystal phase, corresponding to the bulk γ phase, is not precluded and the change in work function may be due in part to this.

On the basis of the above, a number of investigations suggest themselves. Firstly, it is necessary to eliminate any uncertainty concerning gaseous contamination effects, or the effects of contaminant (tungsten or uranium oxides) in the evaporant flux. It had previously been shown by Barry et al that the predominant residual gas in vacuum systems of this type is hydrogen, and further that hydrogen is the main gas evolved during the later stages of degassing the uranium (these findings being subsequently verified in the present work). Whilst there should have been negligible contamination under the present experimental conditions, the effects of hydrogen adsorption had to be eliminated. This was done by determining the effects of hydrogen introduced through a palladium diffusion leak on the work function of up to 12 monolayers of uranium on tungsten emitter tips. The results are described in Appendix 1. It was found that under the experimental conditions of the present measurements (pressures $\leqslant 1 \times 10^{-10}$ torr) the effects of hydrogen contamination are small compared with the experimental error associated with the work function determinations (± 30 mV). The content and purity of the evaporant flux from sources of the type used were determined mass-spectrometrically, and are described in section 9.3.

The second experiment suggested by the above results was as extension of the measurements to coverages of θ 2 in order to observe the onset of the bulk (reversible phase transition) characteristics and to determine the surface properties in the transition region. These measurements are described in sec. 9.4.

Thirdly, the amount of information which can be obtained from measurements of the total emission is rather limited. Described in sec. 9.5 are the modifications made and the results obtained from measurements on individual single crystal planes of field emitters.

A fourth experiment following from the above is to determine whether irreversible behaviour in monolayer films occurs for any element other than uranium. In the present case zirconium which undergoes a phase-transition at 1135°K was chosen and the work on this is described in the following chapter.

9.3 Measurements on the evaporant flux

As the tungsten evaporator filament had burnt out in a number of the work function experiments, the possibility of migration and sublimation of the tungsten or of alloying with the uranium[195,196] and subsequent evaporation arose. According to Raoult's law there should be no more than 0.01% of tungsten in the evaporant flux since tungsten is only slightly soluble in uranium in this temperature range. However, it was not clear that tungsten was being lost by migration alone. To check this and also to determine the oxide content, if any, of the evaporant flux, a tube was constructed in which an evaporator was mounted about 10 cm above the ionizer of an EAI 250 quadrupole mass spectrometer, as shown in Fig. 30.

After thorough outgassing of the uranium (the bulk of the gas evolved being hydrogen) the effective partial pressure as a function of evaporator temperature was recorded by the mass spectrometer. This is shown in Fig. 31. It is seen that observable uranium evaporation begins below 1600°K (compared with 2700°K for sublimation of tungsten from the same filament prior to melting on the uranium); suitable evaporation rates for the work function measurements (partial pressures of 10^{-8} to 10^{-9} torr corresponding to deposition of a monolayer in 10^{2} - 10^{3} seconds) occurring for evaporator temperatures in the range

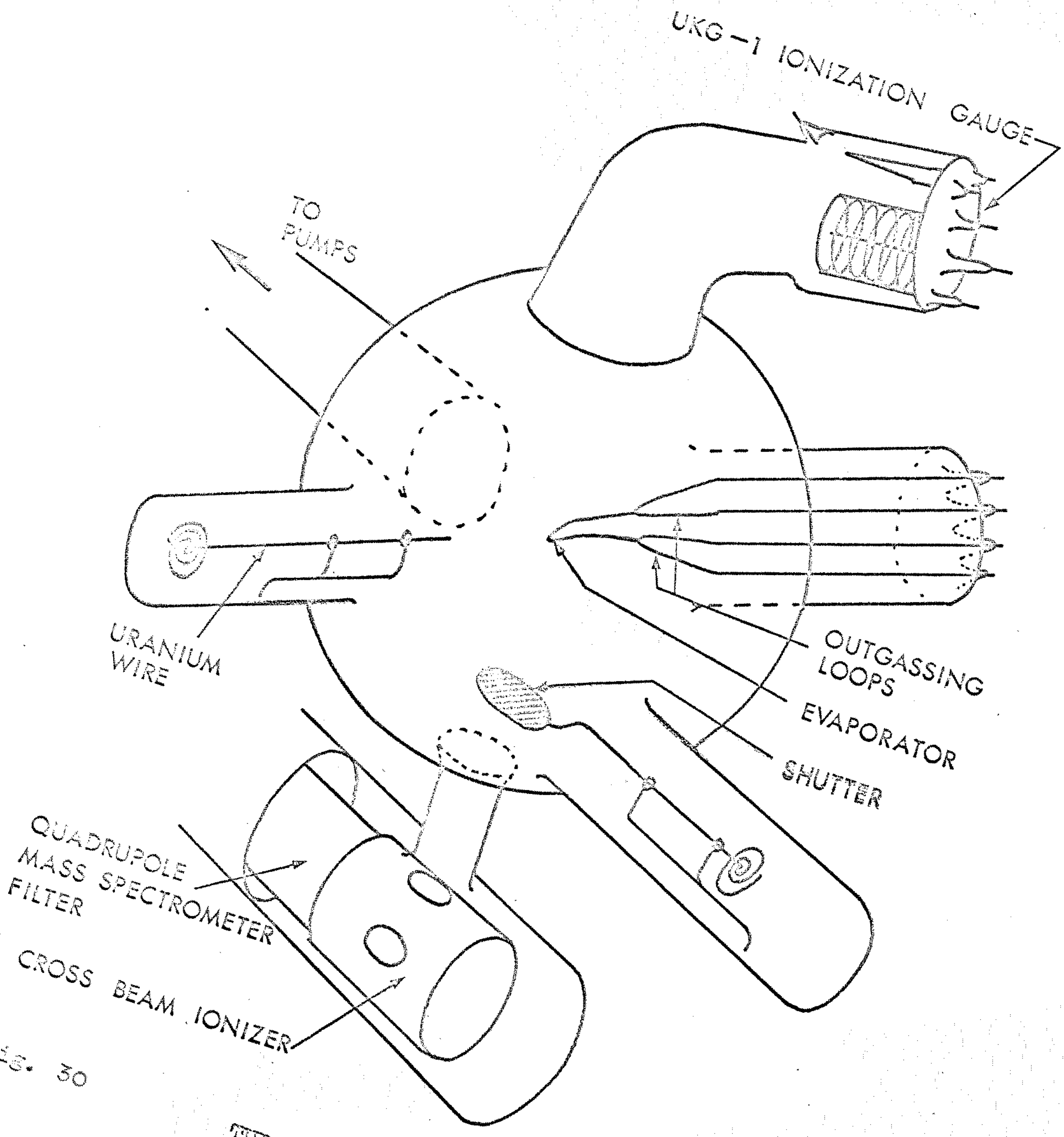

Fig. 30

TUBE DESIGN E

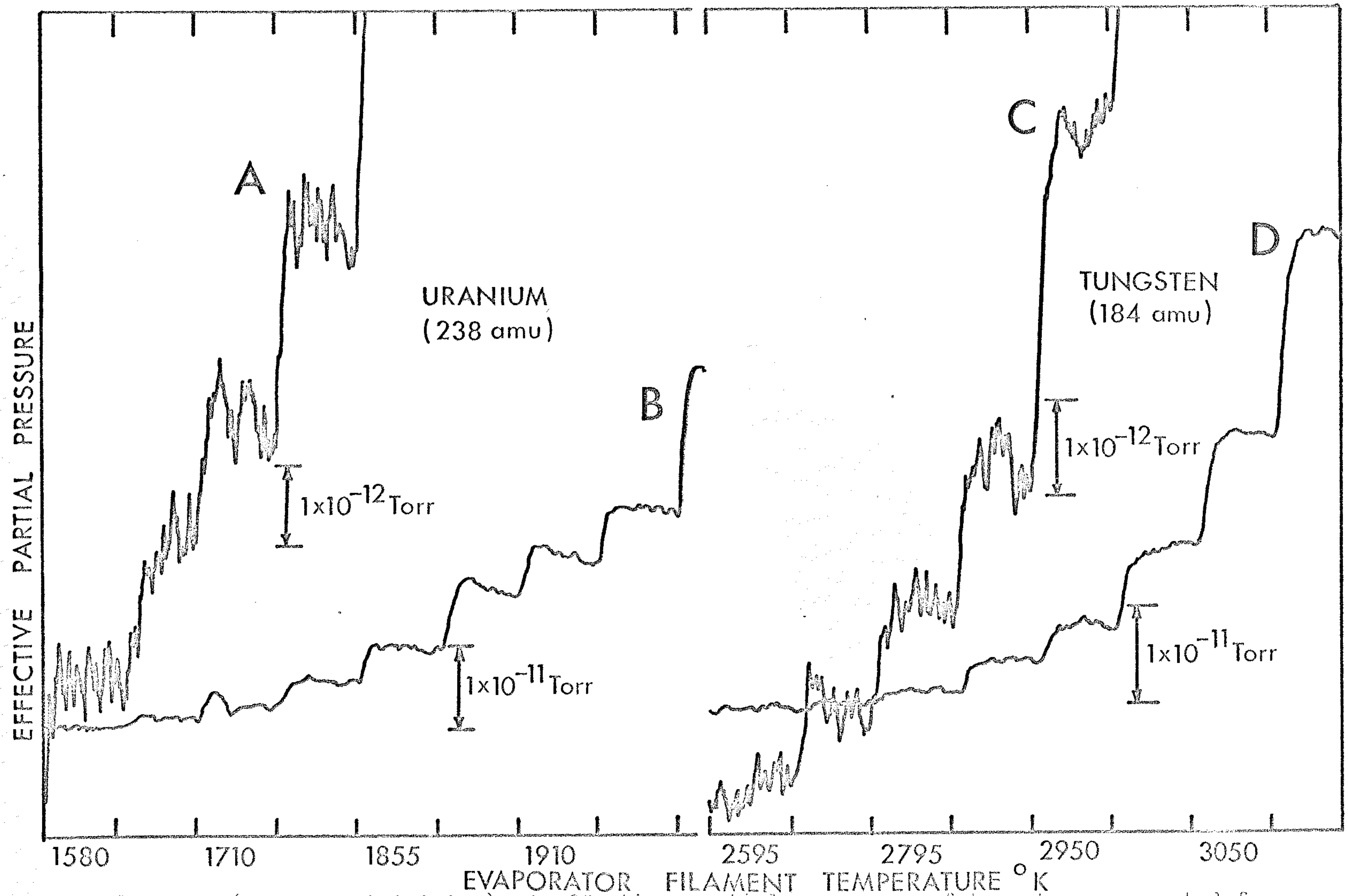

Fig. 31 Plots (at 2 sensitivities) of effective partial pressures of tungsten evaporated from a tungsten filament and uranium evaporated from the same filament as a function of temperature.

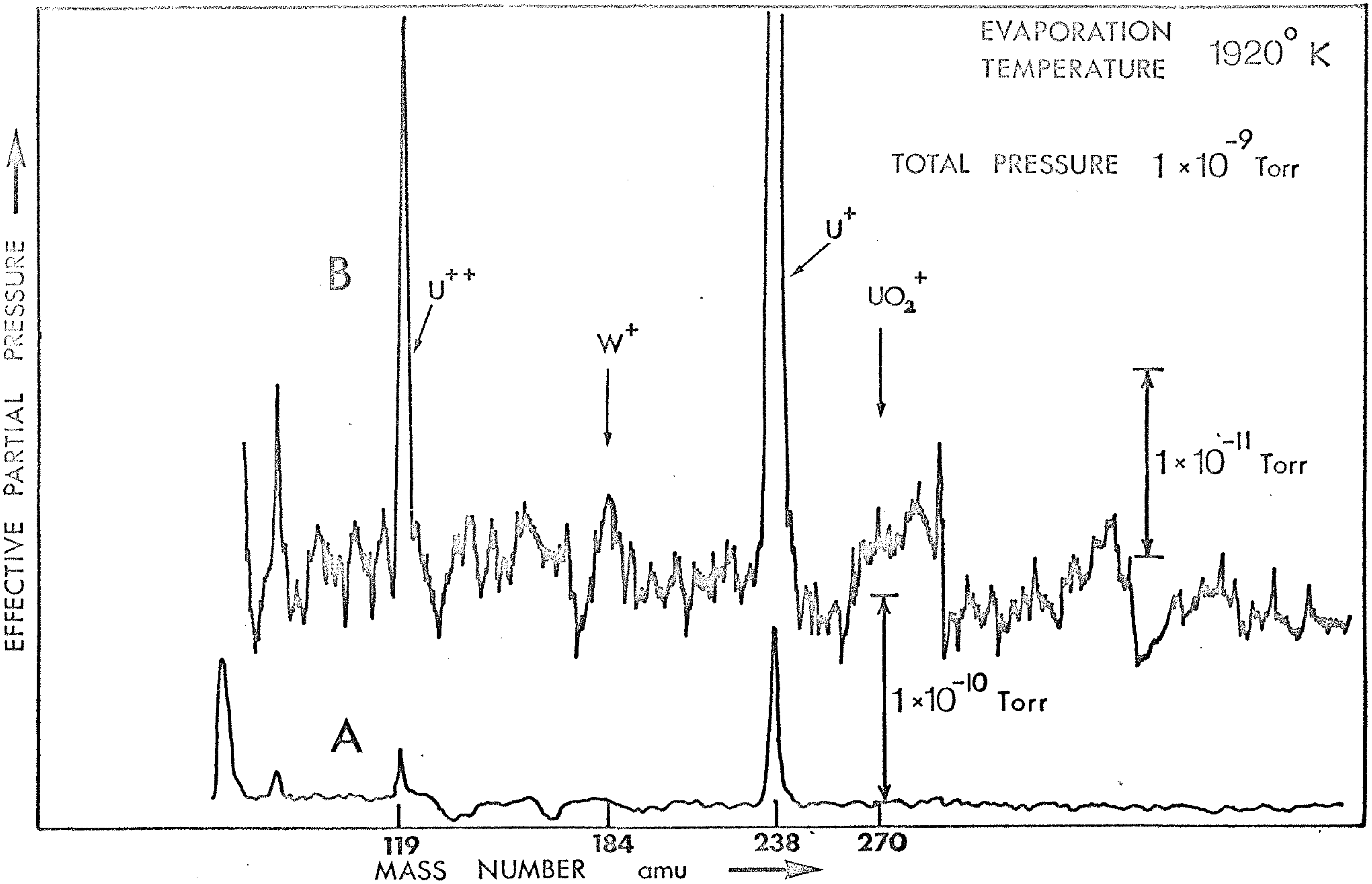

Fig. 32 Mass spectra from 0-500 a.m.u. of the evaporant flux from a uranium-coated tungsten evaporator filament at 1920°K.

1900 - 2000°K.

Mass scans from 0 - 500 a.m.u. were taken for various evaporator temperatures in the 1900 - 2000°K range. Fig. 32 shows, at two sensitivities, scans for an evaporator temperature of 1920°K. It is seen that no W, UO or UO_2 peaks appear above the noise level which is about 3% of the uranium peak.

A plot of the effective partial pressure of uranium as a function of time for an evaporator maintained at 1950°K showed no appreciable decrease in uranium flux over a period of 2 hours. The constant evaporation rate was maintained until just prior to the filament burning-out, when the evaporation rate abruptly dropped. This is further supported by the numerous evaporation rate re-calibrations performed between successive work function/heat treatment experiments, which showed no appreciable change in evaporation rate over periods of about 100 minutes (consisting of up to 20 experimental runs with each evaporator).

It is concluded therefore that the evaporation assemblies used had a constant evaporation rate over the period of experimentation, and that the evaporant flux was contaminant free, (to within the measurement limitation of the mass spectrometer).

9.4 Multilayer Adsorption

9.4.1 Tube Design

The main disadvantage with the type C tubes was that evaporation was over a distance of about 15 cms. This meant that high evaporation temperatures (> 2000°K) had to be used or that deposition of a monolayer deposit took a considerable time (~1 hour). It further meant that fewer experimental runs could be performed with a given evaporator charge. For measurements on thicker layers it was clearly necessary to reduce the evaporation distance.

It was therefore decided to place the evaporator assembly between 1½ and 5 cms in front of the emitter and between it and the phosphor screen. A double shutter shielded both the emitter and the phosphor screen during degassing. The tube design is shown in Fig. 33. During emission measurements, the screen, evaporator and shutter were all maintained at positive potential.

The presence of the evaporator between the emitter and screen, however, resulted in considerable distortion of the field lines and hence the emission patterns.

9.4.2 Work function/coverage measurements

The previous measurements had shown that with increasing coverage the work function had fallen to 3.37 eV before levelling out at 3.60 eV at $\theta = 1.5$. As more uranium was deposited, the work function remained at this value until $\theta = 2$ when it began to decrease slowly, falling to a value of 3.48 eV at $\theta = 7$. Since the initial purpose of these experiments was to observe the disappearance of the phase transition work function changes, detailed measurements were not made at higher

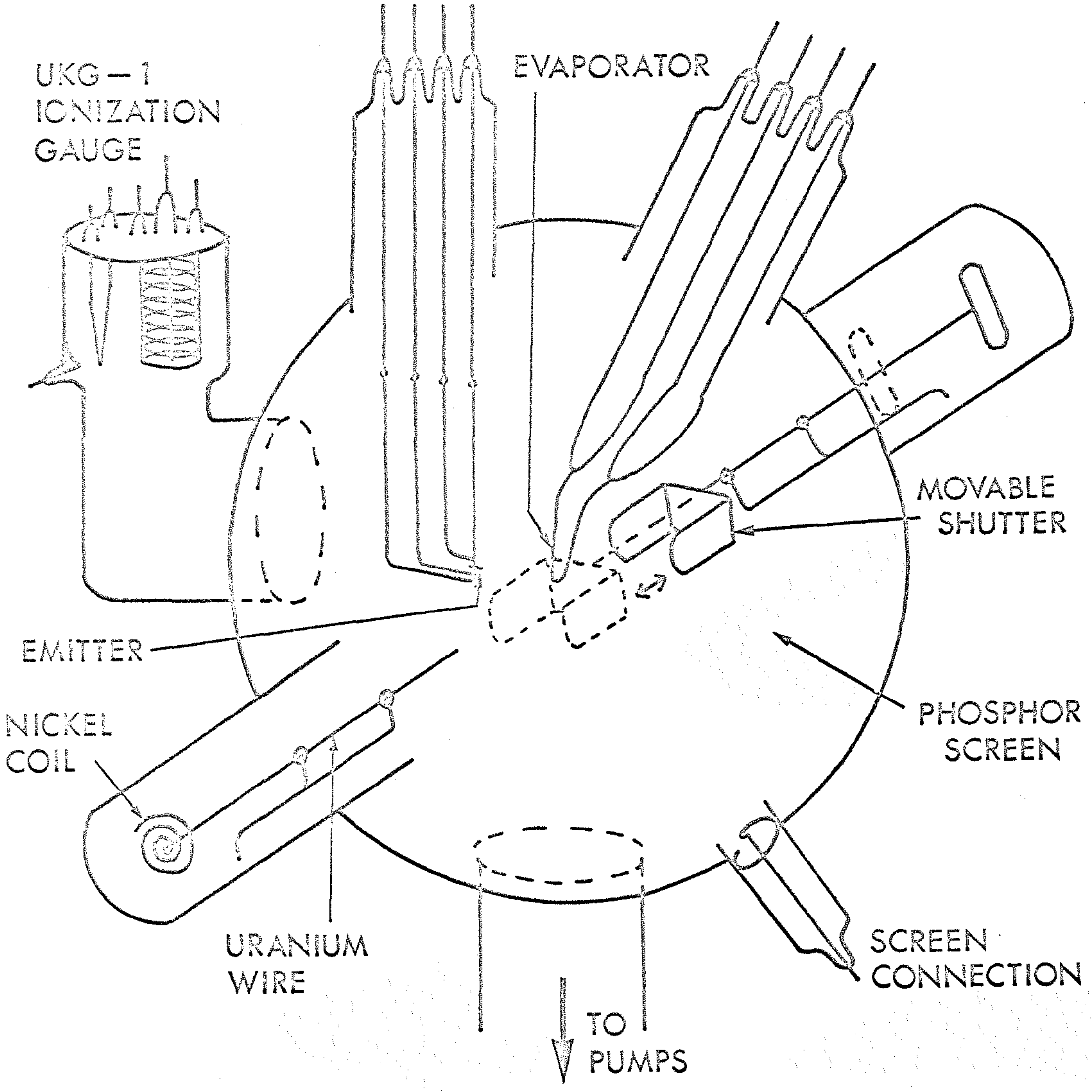

Fig. 33 TUBE DESIGN F. Later modified to incorporate a palladium hydrogen diffusion leak.

coverages than $\theta = 7$. However, a number of subsidiary experiments involved deposition of uranium up to $\theta = 12$, the work function in these cases falling as low as 3.38 eV and showing no sign of levelling out. It was noted that the work function decrease between $\theta = 2$ and 7 was not accompanied by any change in the Fowler-Nordheim pre-exponential term.

The emission patterns accompanying the deposition of thicker layers are shown in Fig. 34 (A-C) for coverages of 3, 5 and 7 monolayers respectively. Fig. 35 shows an orthographic projection of the planes on the emitter surface, distorted to correspond with the emission patterns. It is seen in Fig. 34C that there are three areas of intense demission, A) the (111) region, B) the areas between the (110) and (111) planes, i.e. the (133)'s, (122)'s and (233)'s and C) the region between the (210) and (211) planes.

The brightly emitting regions are well-defined, suggesting the existence of some growth in these areas. As the film thickness increases, the structure must become characteristic of bulk uranium[186] possibly with a high density of dislocations [225-227]. If growth occurs by monolayer addition and not by nucleation, then it is possible that regions of the substrate exhibiting a structure similar to a bulk uranium structure would be energetically most favourable for the initial formation of a monolayer. This may not be so where nucleation predominates.

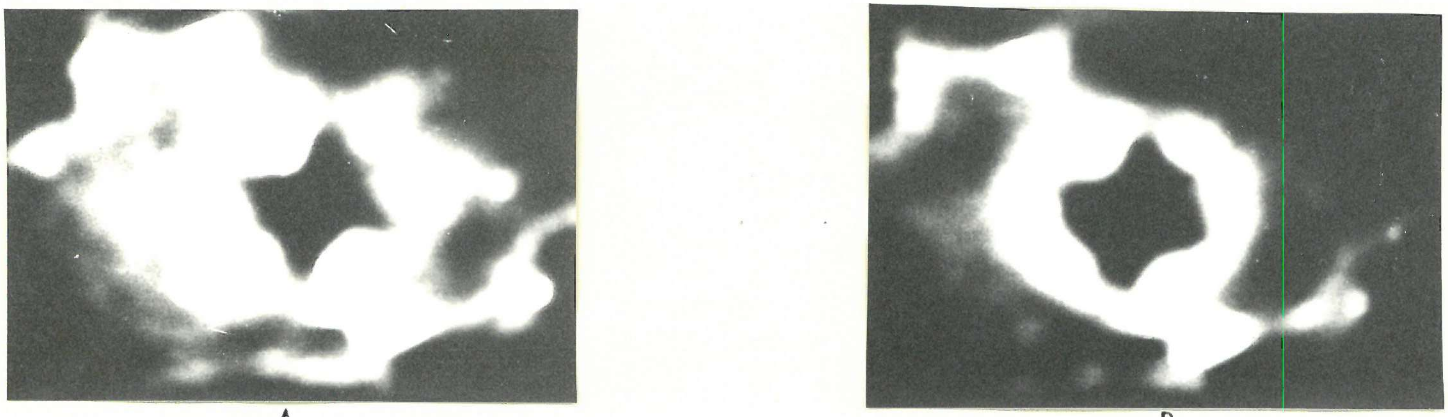

A

B

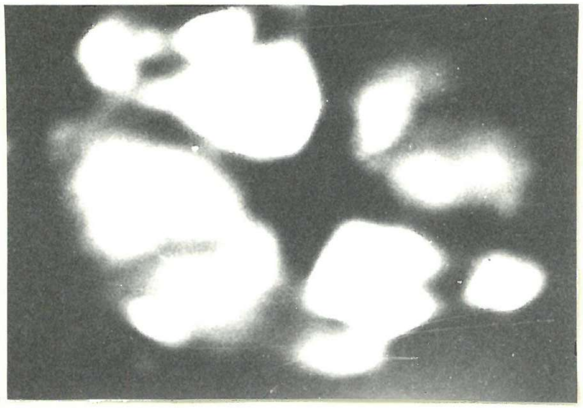

C

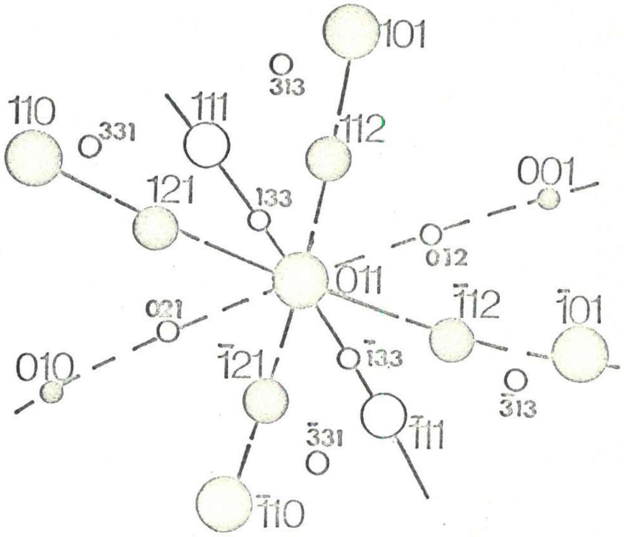

Fig.34 Emission patterns for uranium deposited at 295°K at coverages of (A)3,(B)5 and (C)7 monolayers.

Fig.35 Orthographic projection of the planes on the emitter surface distorted to correspond with figs. 34 and37.

The initial monolayer may then form a suitable substrate for formation of second and subsequent layers. It is interesting that the bright regions of Fig. 34C correspond to areas of the tungsten substrate which show a good geometrical fit to the U(010) surface structure (Fig. 17). If such areas are preferred growth regions, then under conditions of high surface migration they should grow preferentially and exhibit coverages greater than the average coverage of 7 monolayers (Fig. 34C). The emission patterns show that three crystal regions present well defined emitting areas:-

Region A The (111) planes and vicinals are geometrically favourable to a packing of the uranium atoms on the substrate in rows forming a strained alpha uranium structure. Deposition of successive layers after the first may lead to the formation of a characteristic uranium (010) structure. The (010) face of uranium is relatively loosely packed and would therefore exhibit a low work function[25] and hence the high emission intensity observed in the patterns.

Region B The (331), (221) and (332) planes consist of (110) steps of width $3\frac{1}{2}$, $2\frac{1}{2}$ and 2 atoms respectively[223]. These steps have kinked edges which appear to offer binding sites with the four nearest neighbour atoms positioned similarly to those in the trigonal bipyramid structure favoured by α-uranium in the (010) face.

Region C The (210) and (211) planes comprise (110) steps, 3 to 4 atoms across, with sites of high binding energy. Again the α - uranium (010) structure could be accommodated with very little strain and lead to the growth of this plane after deposition of several monolayers.

9.4.3 Work function/heat treatment measurements

The variation of work function with heat treatment temperature for deposits initially of 1 - 1½ monolayers has been shown in Fig. 28. Whilst there is some experimental difficulty in reproducing these plots to within the experimental precision of ± 30 mV, the changes at 934°K and 1042°K have always been observed to occur at the same temperatures and in the same direction and to be irreversible. Furthermore, both in the c.p.d.[9] work and in the measurements described in sec. 9.2 the dip at 1600°K had always been observed. However, measurements in this laboratory using photoelectric techniques[229] have yielded curves in which the work function remained approximately constant after the decrease at 1042°, until it rose again at 2300°K. There is some uncertainty in the coverage in these measurements, but it is thought to be about 2 monolayers. In the present work, a number of plots were made for initial deposits of 1½ - 2 monolayers. Whereas many of these showed the usual dip at 1600°K, several showed the work function remaining constant in the range 1050 - 2200°K. Further, whilst the discontinuities at the phase change temperatures are clearly apparent at θ_i (initial uranium coverage prior to heat treatment) = 1.5, at coverages greater than this they became less well defined and had disappeared completely at $\theta_i = 2$. Fig. 36 (A and B) shows typical plots for initial coverages of 1.7 and 2 monolayers. At the same time the curve assumes a different shape in the temperature region 900°K to 1200°K. A dip appears at 1000°K which becomes more pronounced as the initial coverage is increased. This is followed by a sharp rise and a further fall at 1200°K after which the work function remains constant until the uranium is finally desorbed. Fig. 36 (C-E) shows curves for $\theta_i = 3$, 5 and 7. As the initial coverage is increased, the first dip in the curve becomes more pronounced and the second dip reappears.

The emission patterns in Fig. 36 show characteristic differences from the corresponding patterns for $\theta_i = 1.5$. In the range $\theta_i = 1.5 - 2$, in which the phase transitions become less observable and the dip in the curve at 1000°K appears, the uranium forms apparently smooth deposits around the low index planes when heated to temperatures as low as 800°K. These areas of enhanced emission become most pronounced at 1000°K and this is followed by a smoothing of the deposit and a more uniform pattern at 1100°K. Above 1500°K the patterns are similar to those for $\theta_i < 1.5$. For higher initial concentrations these characteristic

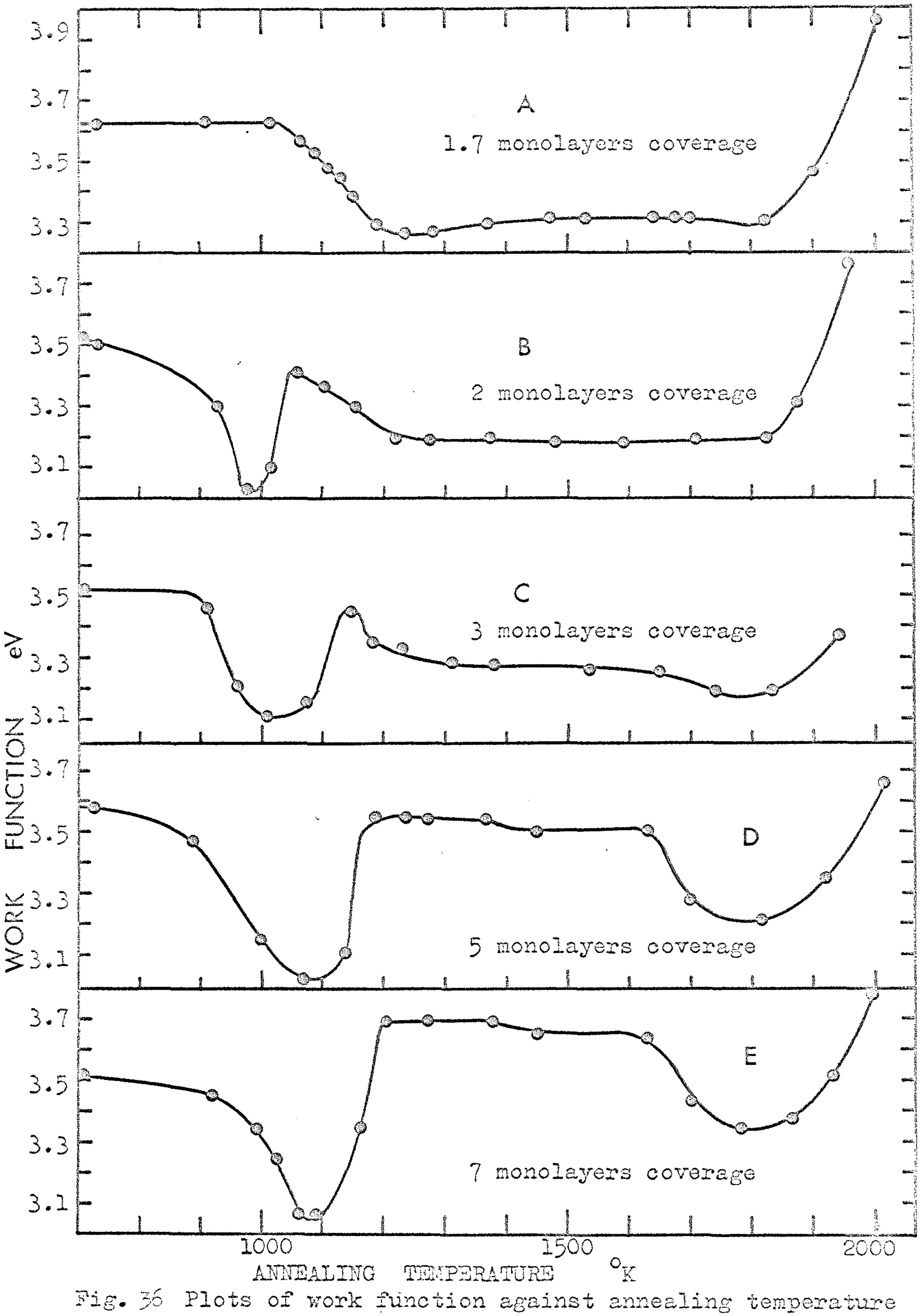

Fig. 36 Plots of work function against annealing temperature for uranium deposits of progressively greater thickness, curve E representing an initial deposit of 7 monolayers.

patterns become more pronounced.. Fig. 37 (A-D) shows the emission patterns for an initial deposit of 7 monolayers after heating to 850°K (A) 950°K (B) 1200°K (C) and 1500°K (D) respectively. Again the regions of bright emission are predominantly those labelled A, B and C in the previous section. It is seen in Fig. 37A that the uranium has become mobile on heating to 850°K with the emission from regions A and B in Fig. 34C. Region C has split into two bright patches of roughly equal intensity. This mobility is in contrast to deposits of $\theta_i < 1.5$ for which there is no change in the emission patterns below 1050°K. No gross change in the emission anisotropy occurred on heating to 850°K in the present case, the regions of greatest emission having simply intensified, suggesting that increased migration due to heating has resulted in further growth of these preferred regions and completion of the of the formation of the bulk uranium α-structure (010) surface.

A major change occurs in the emission distribution on heating above the α-β transition temperature (Fig. 37B). The (111) regions disappear and the (012) - (112) regions become much less intense. The average work function decreases by ~ 0.1 eV after the heat treatment and hence the decrease in intensity of the (111)'s does not imply that any change has taken place on these regions, but simply that emission elsewhere has increased. Region B still remains bright and a fourth region (D) spanning the 110 zone line, between the (113) and (116) planes appears

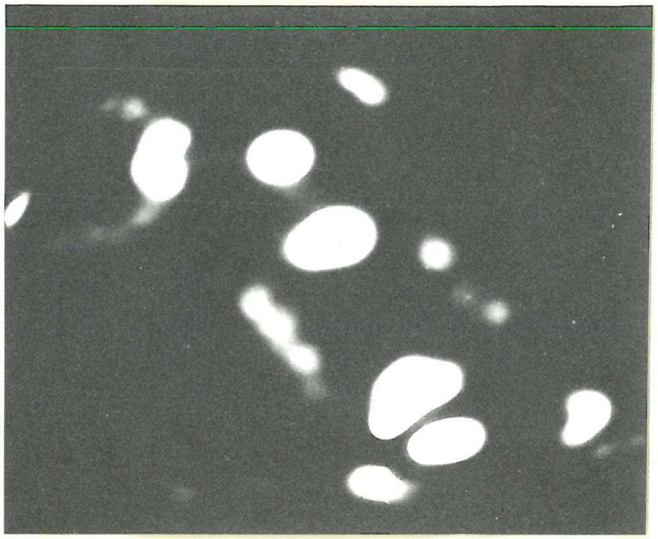

A

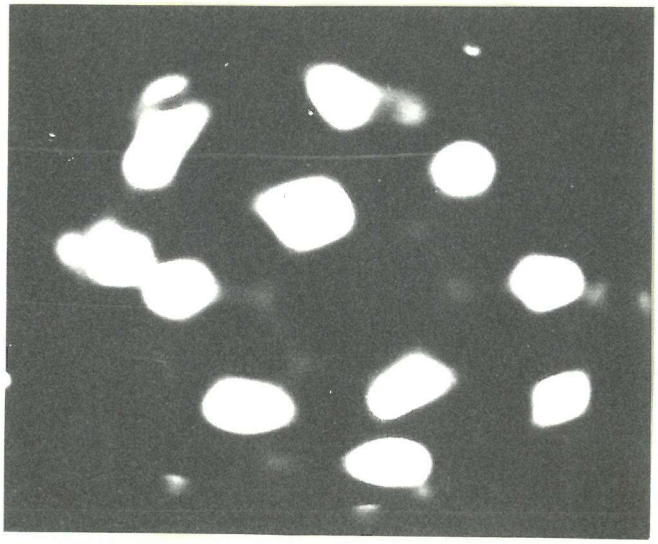

B

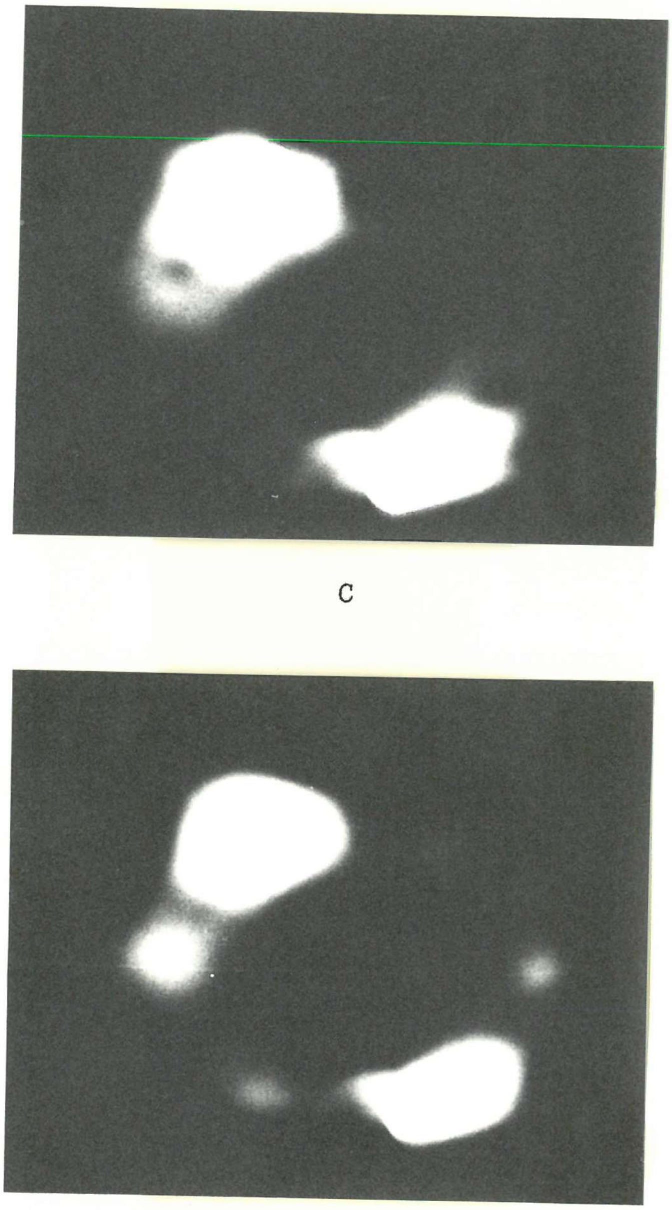

C

D

Fig. 37 Emission patterns of a 7 monolayer deposit of uranium heated for 60"periods to progressively higher temperatures ($T^{\circ}K$).(A) T = $850^{\circ}K$ (B) T = $950^{\circ}K$ (C) T = $1200^{\circ}K$ and (D) T = $1500^{\circ}K$.

bright at this stage. This may be accounted for by recrystallization on heating to the β phase. For the bulk uranium β(010) structure, a hexagonal array occurs with a nearest neighbour distance of 3.01 Å[186]. Region B thus remains bright as the α-uranium (010) structure can easily transfer to this hexagonal β structure with relatively little distortion. Presumably this is energetically more favourable for region B than for A or C. For region D the tungsten (110) steps are set at about 120° to each other, as required for accommodation of a β-uranium hexagonal structure.

Heating to higher temperatures in the β-region results in a further decrease in work function, reaching a minimum of about 3.1 eV, possibly due to further growth and relief of strain.

Heating to 1200°K (Fig. 37C) causes an overall smoothing of the deposit, the emission patterns becoming similar to those for monolayer deposits. At the same time the work function rises to a steady value of 3.7 eV for 7 monolayers coverage in the 1200 - 1600°K range. This may be accounted for by the formation of the bcc γ uranium phase above 1042°K and at 1500°K (Fig. 37D) by sublimation of the uranium and decreased thickness of the deposit due to migration from the tip along the shank of the emitter. The emission patterns at higher temperatures are similar to those for all lower coverages.

9.4.4 Conclusions

On the basis of the above results, the adsorption model suggested in sec. 9.2.3.2 may be extended to coverages in the range $\theta_i = 1.5 - 12$.

It is concluded that films of uranium deposited under the cleanest conditions grow preferentially on particular crystal planes of the substrate. No evidence has been found for growth by nucleation. For heat treatment of the deposit at temperatures below the $\alpha - \beta$ transition these planes have surface structures which correspond closely to the surface structure of (120) α-uranium. Heating in the β range results in different preferred growth regions corresponding to areas which appear to offer a better fit to the β-uranium structure. Further heating to the γ-region leads to gross surface migration and consequent smoothing of the deposit.

The irreversible transitions previously observed at the phase transition temperatures were not found at thicknesses in excess of 2 monolayers, It is concluded that the reason for the irreversible behaviour observed previously must be sought in the uranium -tungsten interaction.

The drop in work function from 3.60 to 3.38 eV in the range $\theta_i = 1.5$ to 12 suggests that the work function of bulk uranium is less than the value of 3.60 eV found for monolayer deposits, at least for uranium surfaces in which the loosely packed (110) planes appear to predominate. If this decrease in work function with coverage continues for coverages greater than $\Theta_i = 12$ then agreement may be obtained with the value of 3.19 found by Riviere.

9.5 Measurements on single-crystal planes

9.5.1 The experimental tube

The tube used for measurements on single crystal planes is shown schematically in Fig. 38. It was constructed from a 3 litre pyrex bulb. The emitter was mounted on a cold finger in a $1\frac{1}{2}$" dia. sidearm containing a 13 convolution stainless steel bellows, allowing 30° movement either way under vacuum. Movement control was by means of a multi-screw assembly mounted on the steel end-pieces, thus preventing undue strain on the glass. The emitter was mounted about 6 cm in front of the phosphor screen which was coated on a flat 70 mm dia. circular tantalum plate containing a 1 mm dia. hole at the centre. The evaporation assembly was mounted next to the screen, evaporation being from a direction at $5 - 30^\circ$ from the emitter axis. A further conducting screen of stannous oxide was coated on the inside of the bulb. The Faraday cage electron collector assembly is shown in Fig. 39. The Faraday cup was constructed of stainless steel coated successively with platinum metal and platinum black to reduce the secondary electron yield. The platinum black was deposited by passing a current of 30 mA/cm^2 with the cup as cathode and a platinum anode in an electrolyte of 2 gm

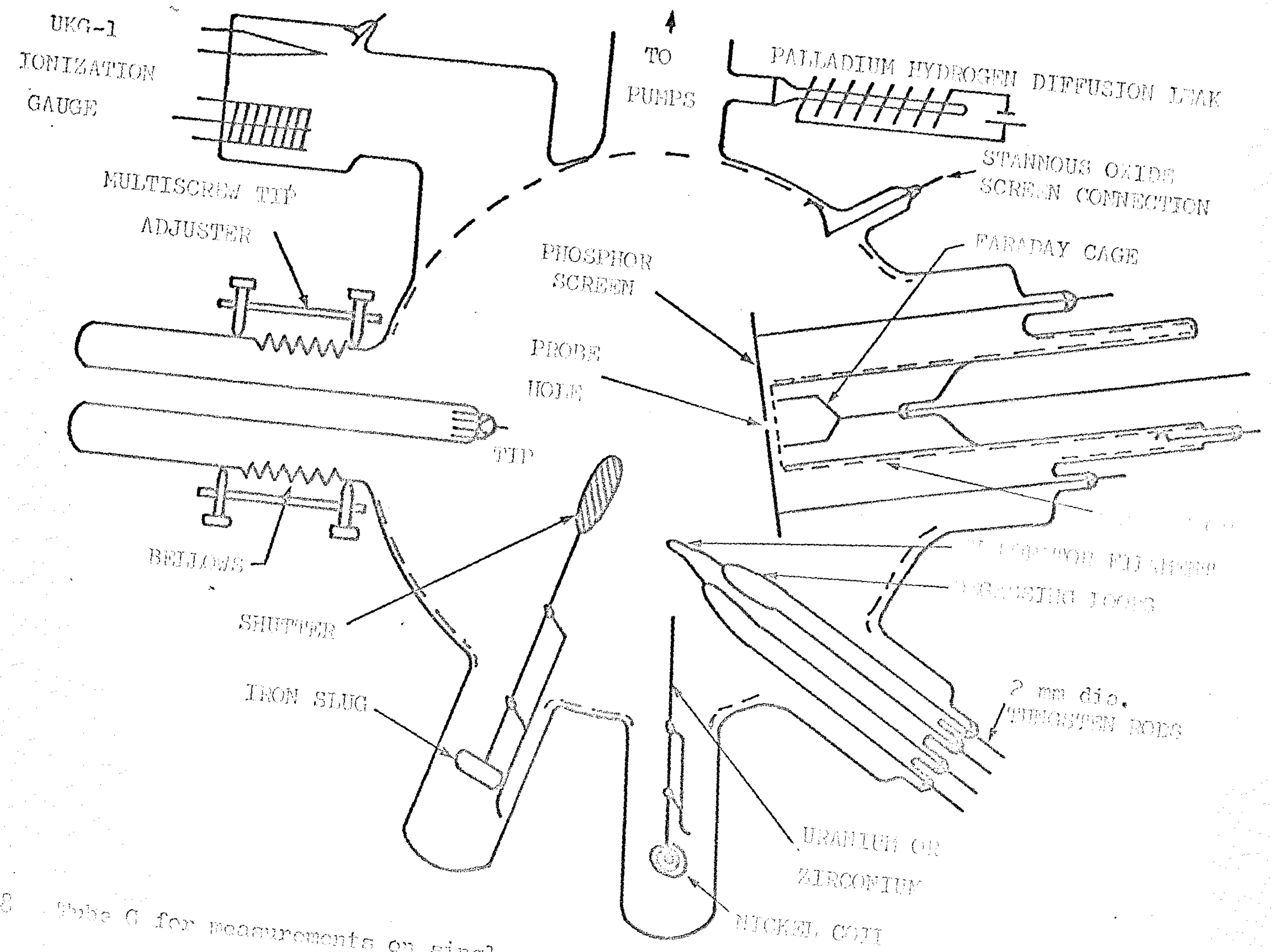

Fig. 38 Tube C for measurements on single crystal planes.

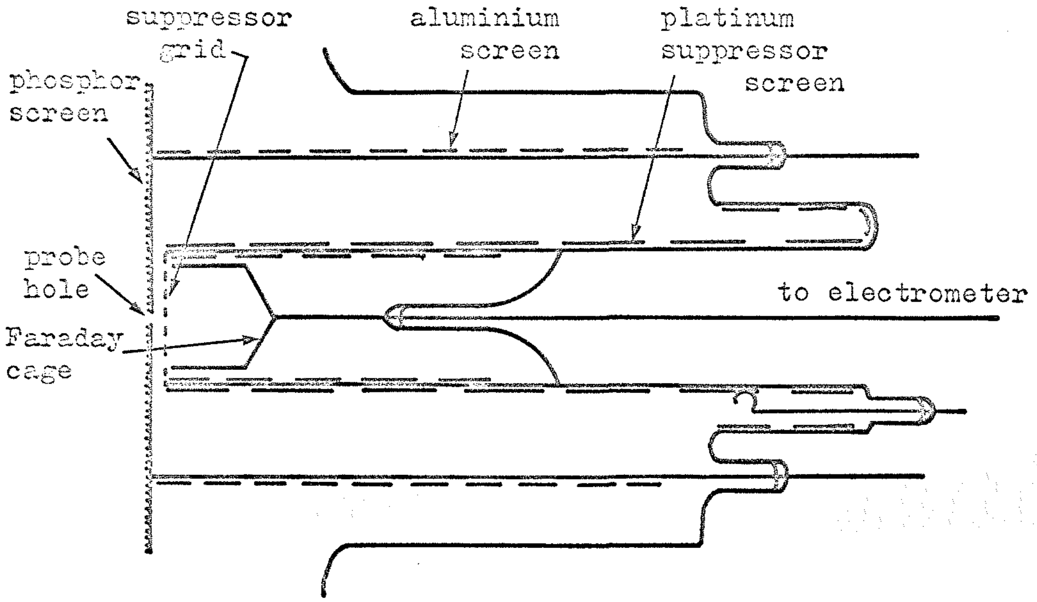

Fig. 39 Faraday cage electron collector and probe-hole assembly.

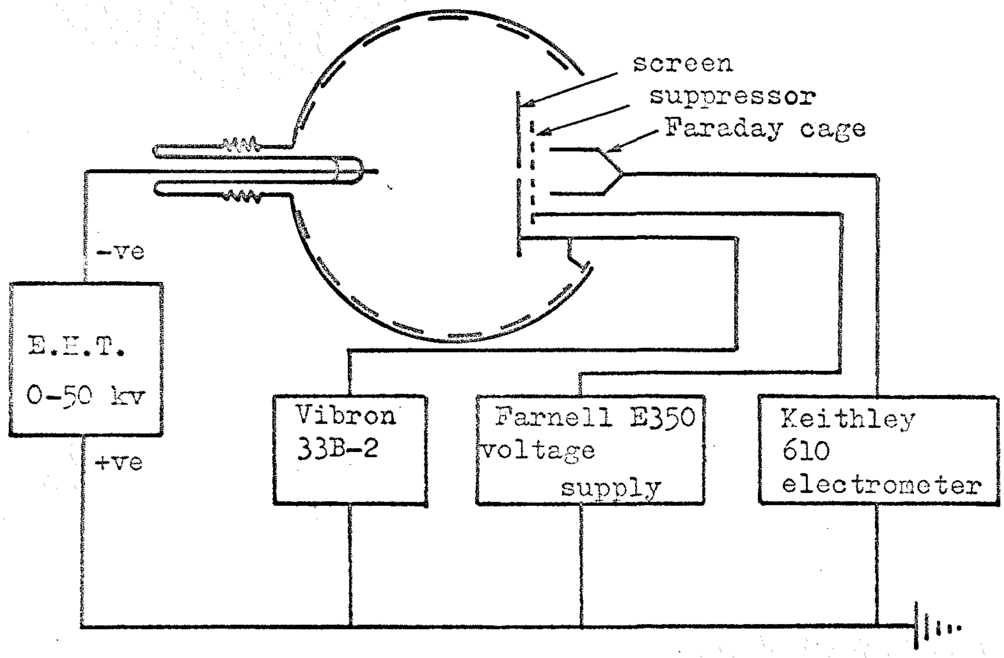

Fig. 40 Circuit for type G tube.

chloroplatinic acid in 50 gm. of water to which had been added 8 gm. of a solution of 0.4 gm. lead acetate in 200 gm. of distilled water. A thick black deposit appeared on the cathode after a few minutes. The cup was supported on a tungsten/glass lead-through. The suppressor was an 80 line/inch 70% transmittance stainless steel grid mounted on a glass tube made conducting by the application of a layer of 'bright platinum'. This grid was also coated with platinum metal and 'platinum black'. Stray electrons were prevented from reaching the suppressor around the sides of the tantalum screen by an aluminium shield.

During operation the circuit used was that shown schematically in Fig. 40, collector currents being measured with a Keithley 610 BR electrometer, the input lead being screened. Suppressor potentials were supplied by a Farnell L350 variable voltage supply. Total emission currents were measured by a Vibron 33B-2 electrometer.

During operation the screen, stannous oxide layer and evaporator assembly were all kept at the same potential. Typical emission pattern magnifications resulted in the diameters of the planes on the screen being 15 mm (110), 8 mm (112) and 4 mm (100). In order to eliminate the patch effects of electrons from surrounding planes it is necessary for the emitter area probed to be at least 30 Å from the edge of the plane, i.e. it is desirable to have a large (plane dia. on screen/probe hole dia.) ratio. This is clearly so for the above planes and possibly for the (111). However, for the other 'planes' the surface under measurement can only be described as predominantly of a given orientation, the surrounding planes contributing significantly to the emission. Thus, measurements on say, the '(116) plane' are not characteristic of a pure (116) surface but of the (116) region of the emitter.

Evacuation and degassing techniques with this tube were identical to those for previous tubes. A somewhat more prolonged degassing period was required, however, presumably due to the large metallic structures contained in the tube.

Before measurements could be made it was necessary to determine suitable voltages for the suppressor and collector. The arrangement eventually used was to earth the screen, evaporator and stannous oxide layer and to operate the emitter at negative potential. Probe-hole currents were measured by the Keithley which was also earthed. Fig. 41 shows plots of collector current (for a (111) plane) against suppressor voltage for a number of emitter voltages. It is seen that the collector voltage remains unchanged for negative suppressor voltages in the range 15 - 50V. During measurements the suppressor was maintained at -30V. Leakage currents between suppressor and collector were typically 10^{-13} amp.

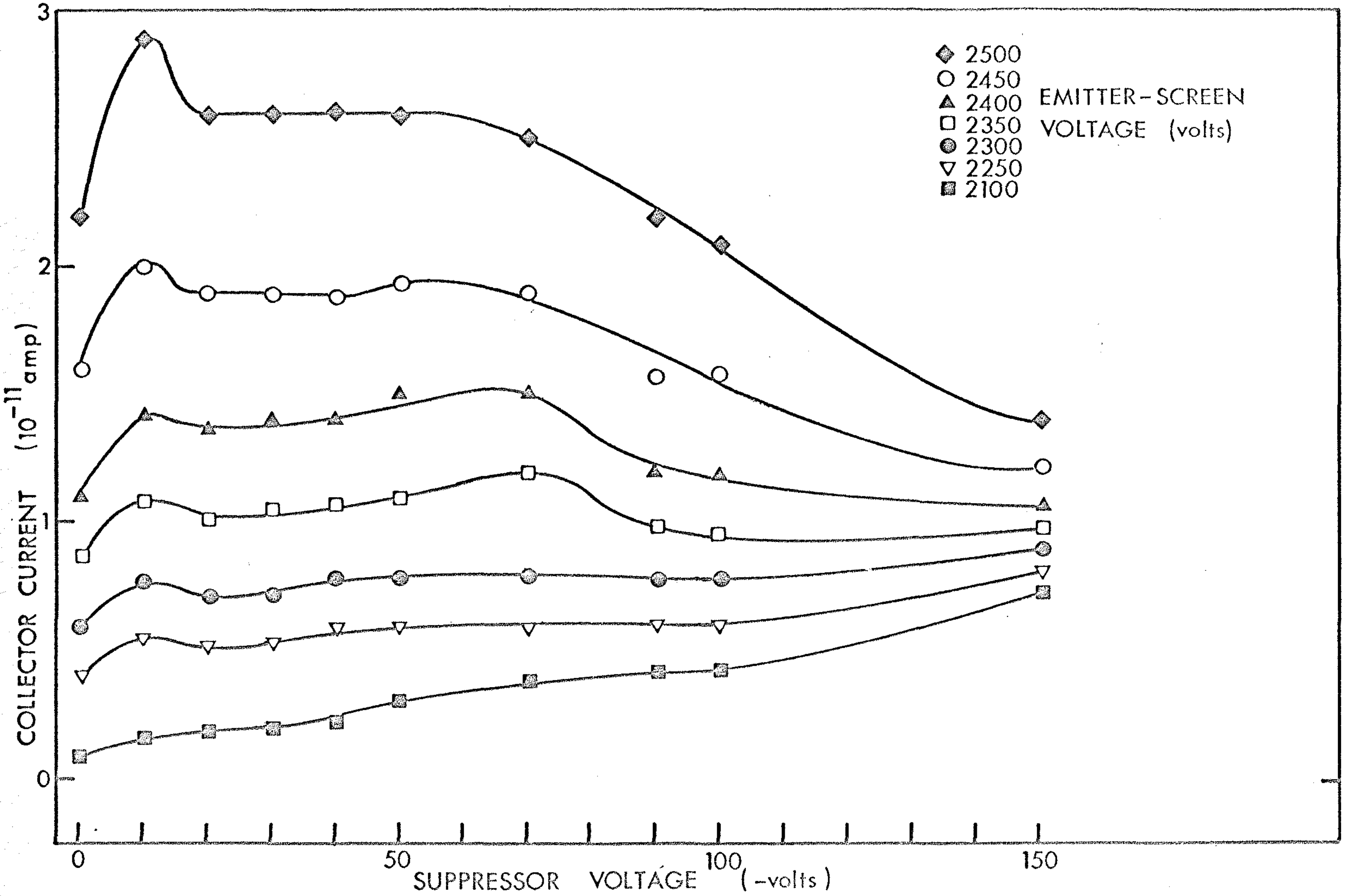

Fig. 41   Tube G : Collector current/Suppressor voltage characteristics for various emitter-screen voltages for emission from a (111) plane

The experimental procedure was to clean the emitter and then position it so that the probe hole was as near as possible to the centre of a given plane. The field was then turned off and the emitter re-cleaned. Preliminary measurements showed that when the emission current was raised to $\geqslant 10^{-6}$ amp in order to view the pattern the pressure rose to $10^{-9} - 10^{-8}$ torr within a few minutes. This was presumably due to hydrogen desorption from the metal screen as previously observed by Schmidt[158]. For this reason the emission patterns were not in general observed during the experimental runs and the measured currents were kept as low as possible. Work functions were determined by the use of both equations (48) and (51), collector currents of $10^{-11} - 10^{-10}$ amp being used for the higher index planes and $10^{-12} - 10^{-11}$ amp for the (110) and (112) planes.

As evaporation was not usually along the axis of the emitter, measurements of the emitter average work function were not generally meaningful and these were only taken in a few cases.

9.5.2 Results

For the measurements on uranium adsorption the (110), (112) (100), (111), (113) and (116) regions were studied. Whilst the emitter could be readily positioned to study the (110), (112) and (100) planes, the (111) was more difficult to locate. The (116) and (113) 'planes' were located by scanning along the (110) zone line and observing the current maxima.

Clean work function values were assumed for the individual planes after consideration of the previously published data[18]. These were 5.20 eV (110), 4.85 eV (112), 4.65 eV (100), 4.50 eV (113), 4.40 eV (111) and 4.26 eV (116).

Figs. 42 - 47 show the variation of work function against coverage for uranium deposited in all three phase regions (Figs. 42 - 45) and for the α and γ regions (Figs. 46 and 47). These graphs were constructed from work function measurements using equation (51). The principle objection to the use of this equation, namely that it assumes a constant value for the Fowler-Nordheim pre-exponential term is not as valid in the case of single plane measurements as for measurements of total emission. Fig. 48 shows the change in the pre-exponential term during adsorption on the (110), (112), (100) and (111) planes for the three temperature regions. With a few exceptions (discussed below), the pre-exponential term remained fairly constant with increasing coverage.

Figs. 42 - 47 show a number of interesting features. In Fig. 42 ((112) plane) it is seen that the room temperature curve shows an abrupt dip at low coverage, this curve lying below both the higher temperature curves before rising above them and levelling out at 3.7 eV. This is almost certainly a consequence of the nucleation observed on the (112) planes at low coverage (Fig. 27), the apparently low work function arising

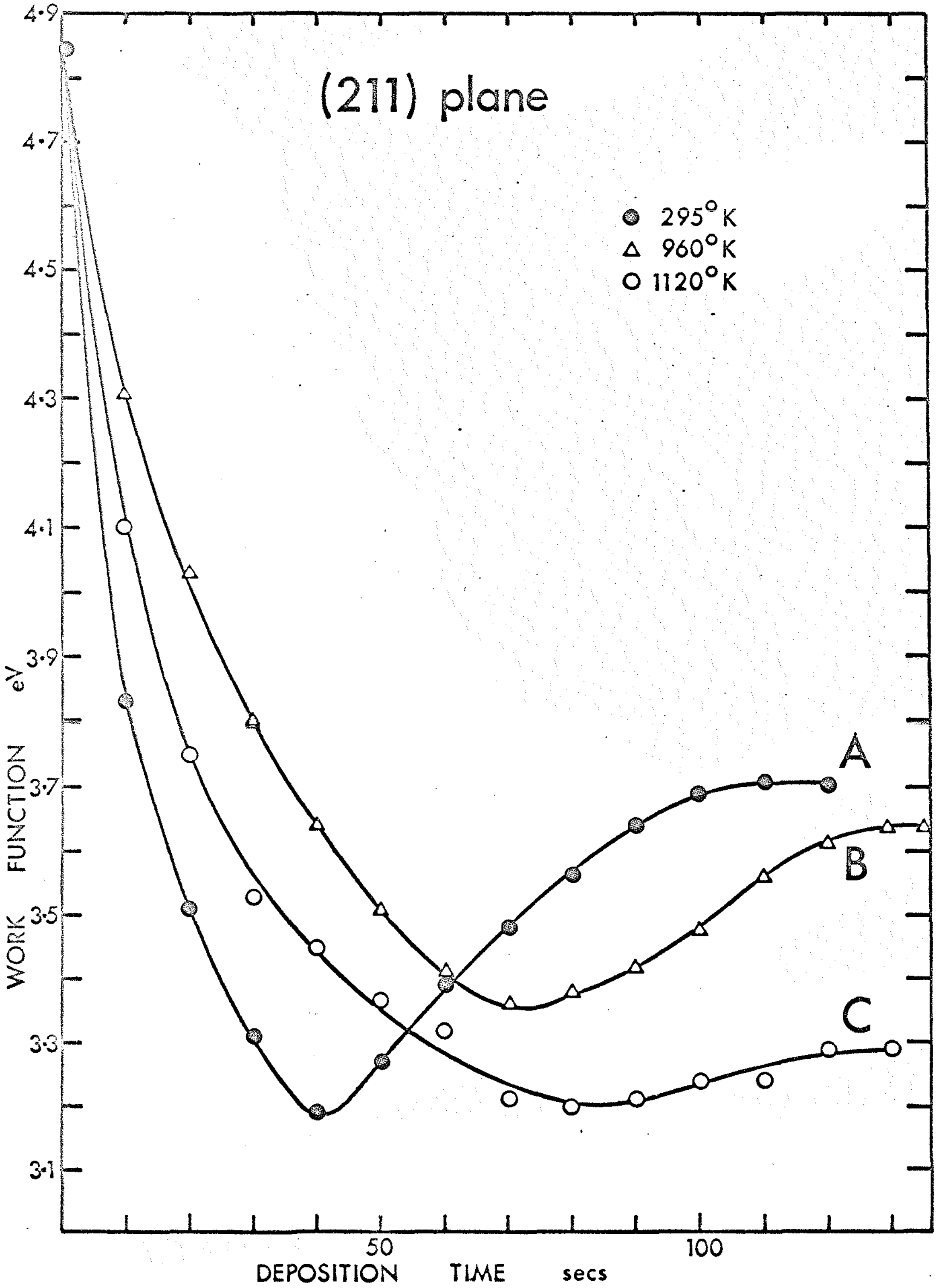

Fig. 42 Plots of work function against coverage for uranium deposited on the (211) plane (A) at 295°K, (B) at 960°K and (C) at 1120°K.

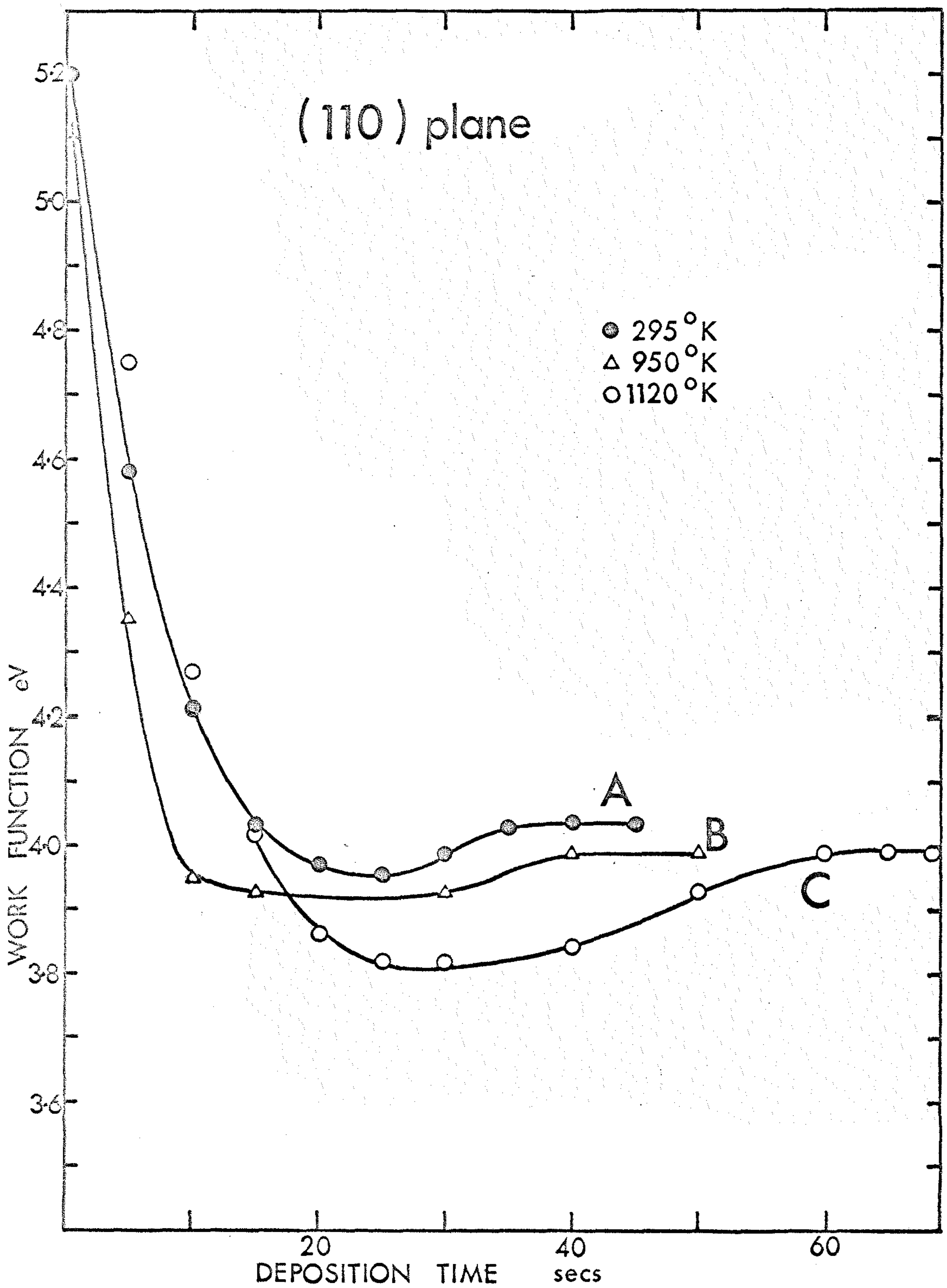

Fig. 43 Plots of work function against coverage for uranium deposited on the (110) plane (A) at 295°K, (B) at 950°K and (C) at 1120°K.

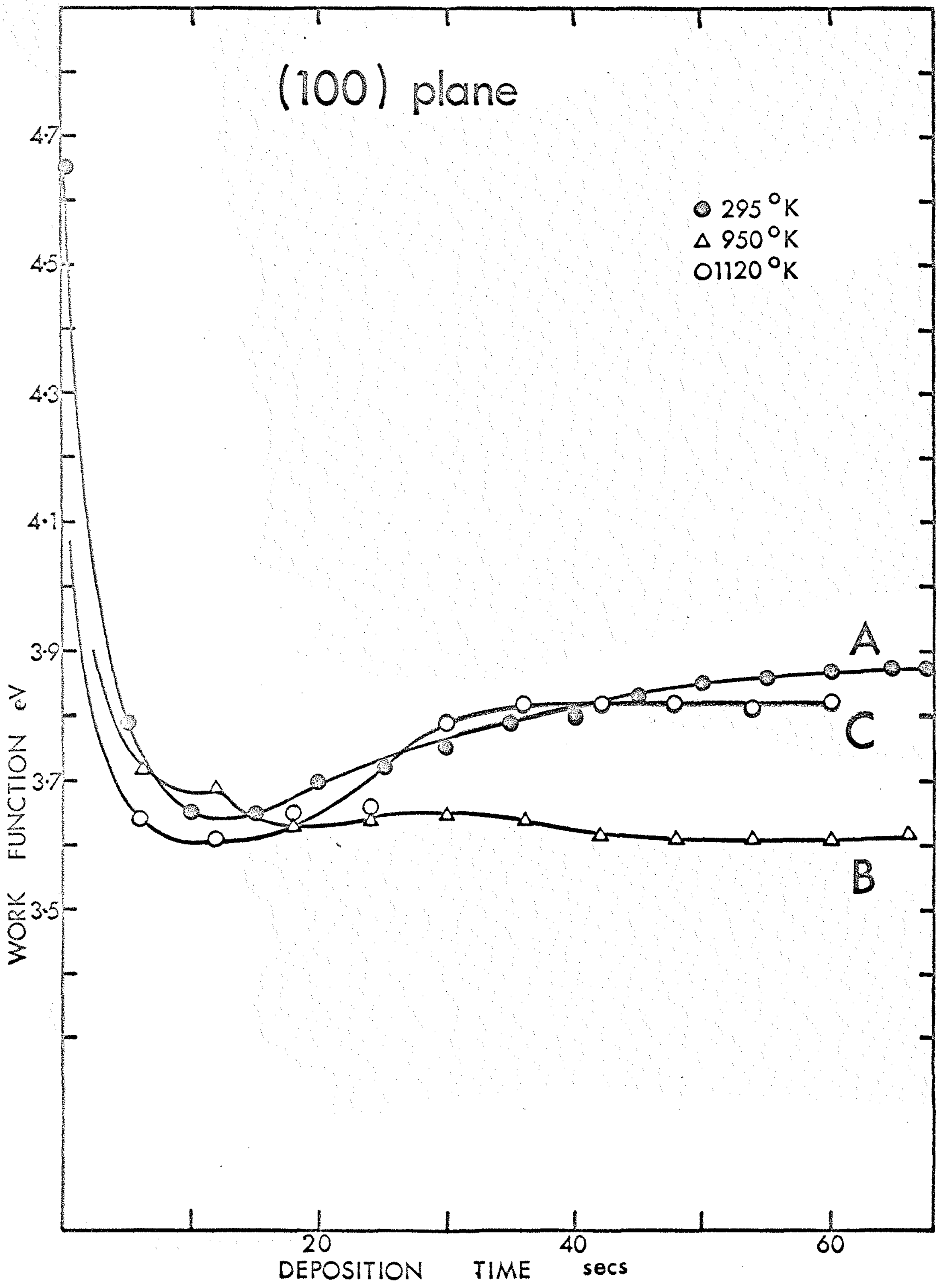

Fig.44 Plots of work function against coverage for uranium deposited on the (100) plane (A) at 295°K,(B) at 950°K and (C) at 1120°K.

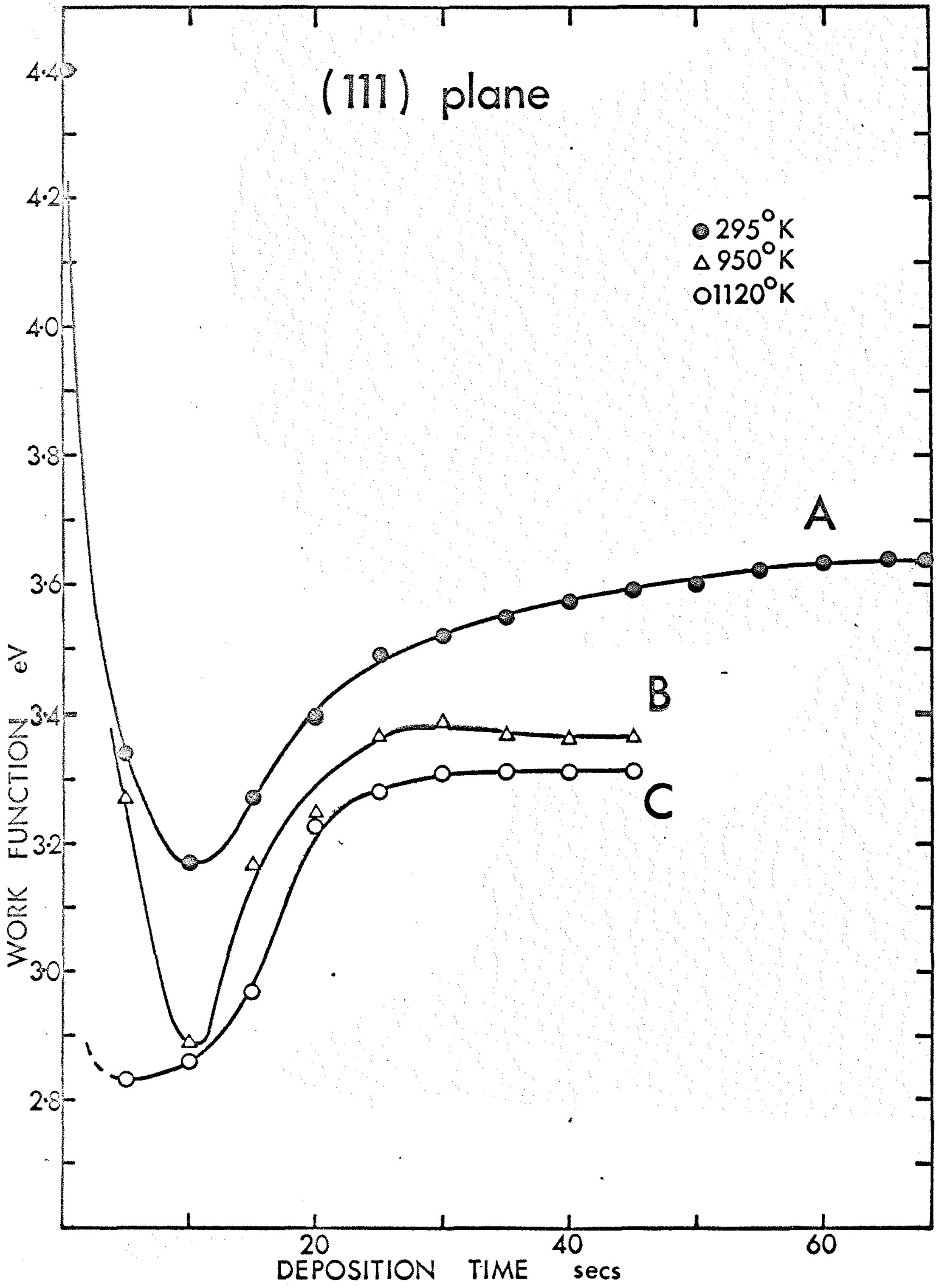

Fig.4·5 Plots of work function against coverage for uranium deposited on the (111) plane (A) at 295°K, (B) at 950°K and (C) at 1120°K.

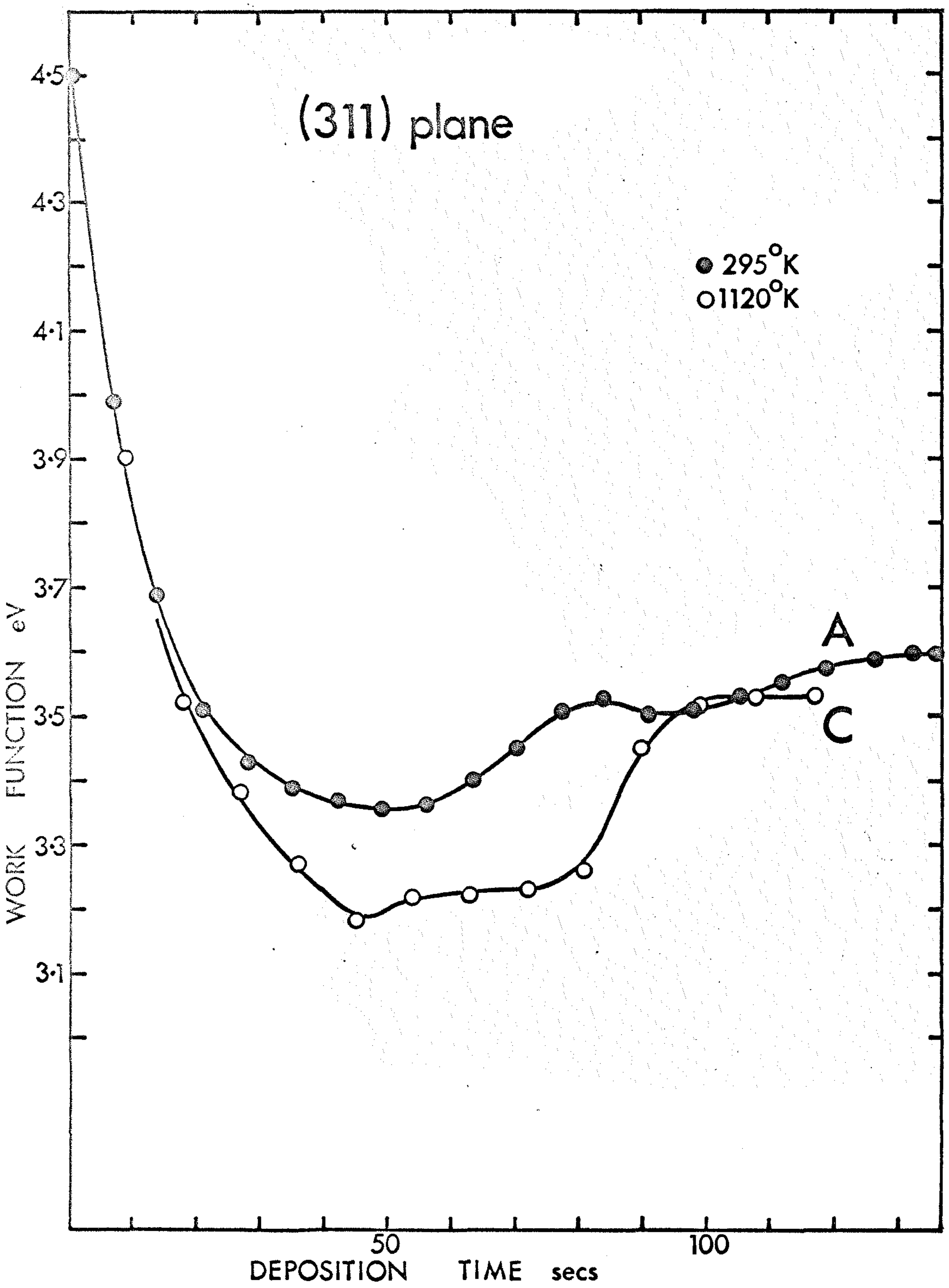

Fig. 4-6 Plots of work function against coverage for uranium deposited on the (311) plane (A) at 295°K and (C) at 1120°K.

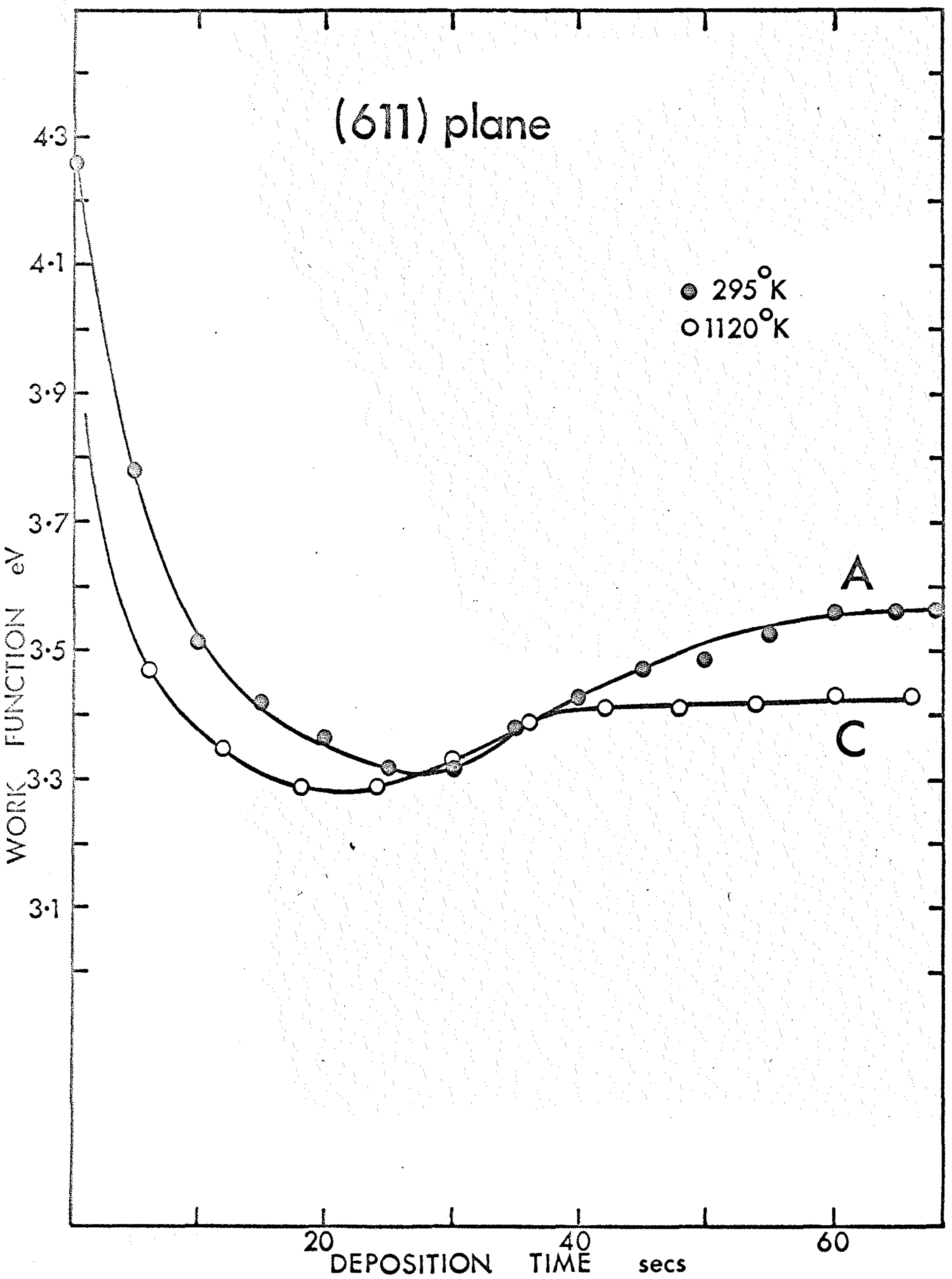

Fig. 47 Plots of work function against coverage for uranium deposited on the (611) plane (A) at 295°K and (C) at 1120°K.

from the increased local field (and hence increased emission) at the points of decreased local radius of curvature[167]. It is interesting, however, that whilst the emission patterns for deposition at 295°K and 960°K (Fig. 27) show no discernible differences, the dip in Fig. 42B is much less pronounced than in 42A. Consideration of the respective pre-exponential terms (Fig. 48) however, shows that whereas at room temperature the pre-exponential term varies about its original value during deposition at 960°K it shows a fairly steady rise, reaching a peak near the minimum of the work function curve, followed by a fall. It is concluded from this, therefore, that during the α-β transition a change takes place on the (112) plane on an atomic scale, such that no change appears in the emission patterns, but a change results in the effective emitting area. Fig. 42C shows a small dip, as expected where the deposit is smoother and no nuclei are observed. The pre-exponential term, however, shows a steady rise.

The (110) and (100) curves (Figs. 43 and 44) show very small dips in all the curves. This is again to be expected as no nucleation or growth is observed on the (110)'s and nucleation is observed on the (100)'s only at low temperatures (Fig. 27). It is also noticeable that the pre-exponential terms remain fairly constant during adsorption on these planes. The (110) plane shows the greatest changes in work function

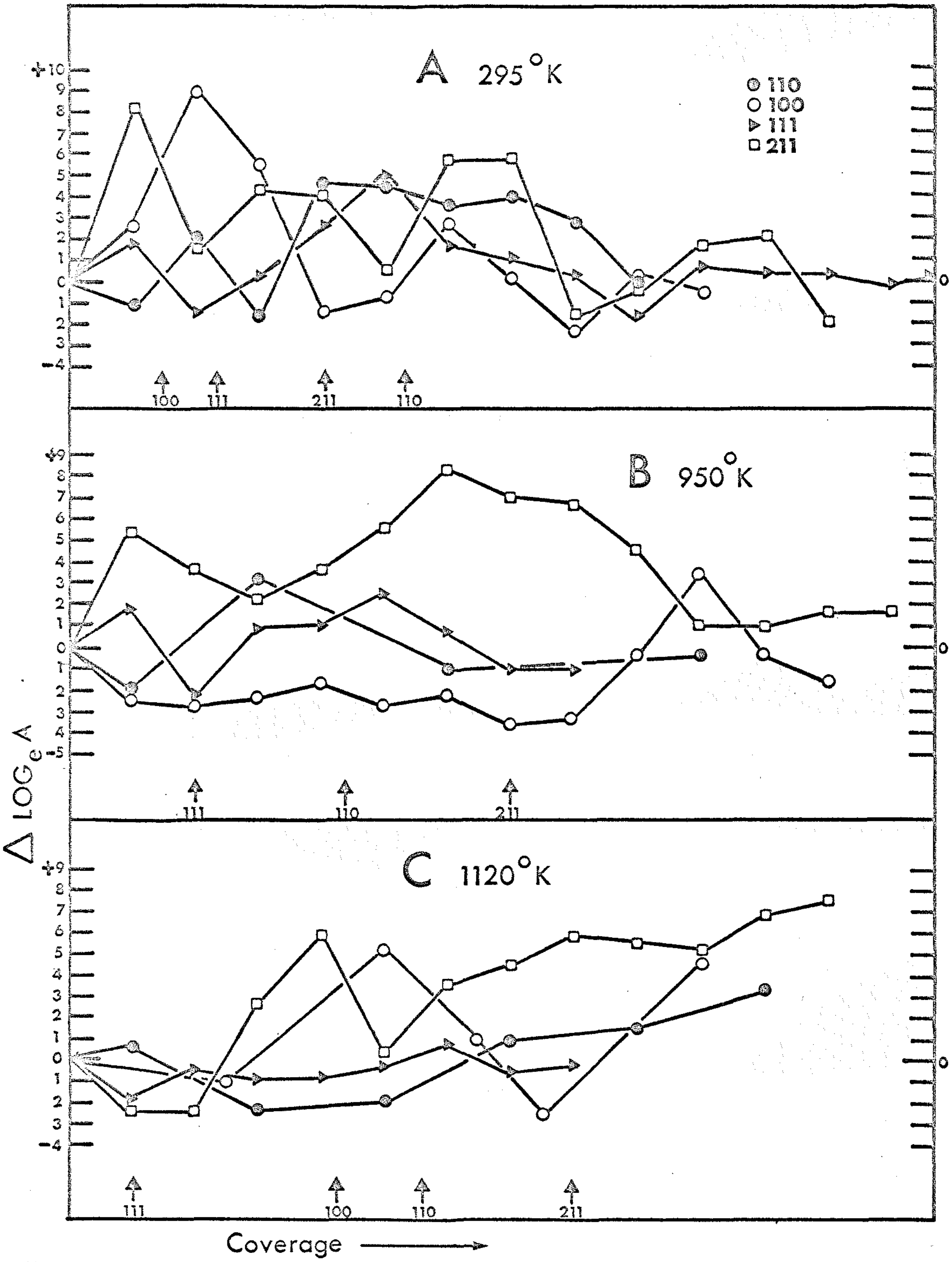

Fig. 48 Plots of the variation in the Fowler-Nordheim preexpo--nential term against coverage for uranium deposited on the 110 (●), 100 (○), 111 (▷) and 211 (□) planes (A) at 295°K, (B) at 950°K and (C) at 1120°K. The arrows indicate the positions of the minima on the respective work function/coverage curves.

of any of the planes (~ 1.2 eV) and this is consistent with previous work using other adsorbates[156,157,230]. In contrast to the other planes, with the possible exception of the (112)'s, the high temperature curve for the (110) takes longer to level out than the lower temperature curves. A possible explanation for this may be in terms of surface migration from this plane, and trapping in neighbouring sites. This implies that the activation energy for migration from the (110) plane is lower than for other planes, in contrast to the measurements of Rhodin[85]. These measurements underline the need for further work on migration parameters to clarify these points.

It should be noted at this point that due to the non-uniform distribution of the adsorbate on the emitter (evaporation not along the tip axis) it was difficult to relate the single plane curves to the total emission curves. However, the curves shown in any one of figures 42 - 47 were for consecutive runs using identical evaporation times. Thus the curves in any one figure are positioned correctly with respect to one another. As a rough approximation measurements above 1100°K showed the minima of the total emission curves to correspond with the minima of the single plane curves (curves C in Figs. 42-47). An exception to this was the (111) plane.

The (111) curves (Fig. 45) show very pronounced dips, suggesting nucleation or growth on these planes at all temperatures. The corresponding pre-exponential terms however, show very little variation.

The curves for the remaining planes, the (113) (Fig. 46) and the (116) (Fig. 47) show remarkable similarities to the total emission characteristics (Fig. 26) both in the shapes of the curves and in the actual work function values. In fact, apart from the (quite reproducible) kink in the (113) room temperature plot, the (113) curve (Fig. 46A) is identical to the corresponding total emission curve (Fig. 26A). This is rather to be expected as the average work function defined by equations (48) and (51) is weighted heavily in favour of these low work function planes.

The kink in curve 46A occurs at the point defined (see sec.9.2.3) as the monolayer position. It is therefore tempting to suggest that this point marks the completion of the first chemisorbed layer, and the kink in the curve is associated with the formation of the beginning of the second layer.

As in the total emission work measurements were made on the variation of work function with heat treatment temperature. A difficulty was encountered due to the uneven deposit thickness over the whole emitter in that the onset of migration often resulted in a marked change in the coverage of the plane being observed, due to migration from neighbouring more-densely populated planes. However, where measurements were made they were in good agreement with the variations expected from Figs. 42 - 47.

For the (112) plane the irreversible phase changes were well marked. The change at 934°K resulted in a drop of about 50 mV in the work function, and at 1042°K a drop of 70 - 200 mV (the wide variation probably being associated with the statistical fluctuations in the dispersion of the nuclei).

On the (100) planes a small dip occurred in the work function at 934°K followed by a larger rise, the work function then remaining steady until thermal desorption began.

Little change was found for the (110) planes, but this again was to be expected from Fig. 43.

As in the deposition curves, the (113) and (116) planes showed a marked correspondence with the total emission curve, the phase changes being fairly well defined. A dip occurred in the curve during desorption, but in both cases at 1750°K compared with 1600°K in Fig. 28. This may have been due to the uranium being retained longest on these high index planes.

Measurements of the adsorption of uranium on massive tungsten single crystals have recently begun in this laboratory. To date the only result available is for adsorption at 295°K on the (110) plane[231]. A final value of 3.9 eV is obtained in reasonable agreement with the present work.

Attempts have been made by previous workers to determine dipole moments and adsorbate polarizabilities from plots of field emission work function/coverage on single crystal planes [70,158,232].

For example Schmidt[158], studying barium on tungsten, has fitted data for adsorption on the (112) plane to the Topping[56] point dipole depolarization model

$$\Delta\emptyset = \frac{n\,\mu o}{\varepsilon o(1+\frac{9\alpha n}{4\pi\varepsilon_0}^{3/2})} \qquad (52)$$

where μo is the dipole moment at zero coverage, α is the effective polarizability and n is the adsorbate surface atom density. From this he calculated μo_{112} and α_{112}. He then applied the Helmholtz equation

$$\Delta\emptyset_i = \frac{\mu_i n_i}{\varepsilon_o} \qquad \text{(equation 19)}$$

to a given plane i, and assuming the value μo_{112} for all planes, calculated the values of n_i (atom density after thermally equilibrating the deposit) from the observed values of $\Delta\emptyset_i$. Binding energies were then calculated as, (in the absence of entropy effects), the ratio of equilibrated atom densities on planes i and j is given by the Boltzmann factor

$$\frac{n_i}{n_j} = \exp(-(H_i - H_j)/KT) \qquad (53)$$

where the H's are the binding energies and T is the temperature below which surface diffusion cannot maintain equilibrium between planes.

The assumptions and limitations of this type of analysis should be kept in mind. Firstly, equation (52) may be modified to include a field polarization term[233]

$$\Delta\phi = \frac{n(Mo - \alpha F)}{\varepsilon_o(1 + \frac{9\alpha n}{4\pi\varepsilon_o}^{3/2})} \qquad (54)$$

where Mo is the zero coverage dipole moment and F is the polarizing field. Secondly, the dipole moment μo_{112} calculated for the (112) plane was used by Schmidt on all the other planes, although there is no justification for doing this. Thirdly, values for n in equation (52) have to be assumed for each plane.

Calculations of this type in the present work are restricted to the (100), (110) and (113) planes, as these are the only planes for which reliable adsorbate atom density values are available. Lea[214] has determined the location of the adsorbed uranium atoms for these planes, finding values for the monolayer coverage densities of 10.0×10^{18} m^{-2} for the (100) plane, 7.1×10^{18} m^{-2} for the (110) and 12.7×10^{18} m^{-2} for the (113) plane.

From equation (54)

$$\left(\frac{d\Delta\phi}{dn}\right)_{n \to o} = \frac{Mo - \alpha F}{\varepsilon_o} \qquad (55)$$

Inserting the initial slopes of curves 43A, 44A and 46A in equation (55) the following values are obtained

$$(Mo - \alpha F)_{100} = 24.8 \times 10^{-30} \text{ cb.m.}$$

$$(Mo - \alpha F)_{110} = 12.4 \times 10^{-30} \text{ cb.m.}$$

$$(Mo - \alpha F)_{113} = 9.5 \times 10^{-30} \text{ cb.m.}$$

Substituting these values in equation (54) and taking $\Delta\phi$ from Figs. 43A, 44A and 46A, the following effective polarizability values are obtained

$$\alpha_{100} = 62 \times 10^{-40} \text{ f.m.}^2$$

$$\alpha_{110} = 21.7 \times 10^{-40} \text{ f.m.}^2$$

$$\alpha_{113} = 14.6 \times 10^{-40} \text{ f.m.}^2$$

These compare with values of about 5×10^{-40} f.m.^{2} obtained by Lea[234]. Using these values for α and taking $F = -3.5 \times 10^9$ v.m.$^{-1}$ the above values for $(Mo - \alpha F)$ give the following values for the zero field dipole moments.

$$Mo_{100} = 3.20 \times 10^{-30} \text{ cb.m}^2$$

$$Mo_{110} = 4.84 \times 10^{-30} \text{ cb.m}^2$$

$$Mo_{113} = 4.40 \times 10^{-30} \text{ cb.m}^2$$

Assuming that $Mo = 2qr_o$ where $2r_o$ is the dipole length, then for the (100) plane taking $2r_o$ as 2.8 Å, $q < \frac{1}{10}$ electron/atom.

In view of the assumptions made with regard to n (Lea assumed a uniform adsorbate distribution with no nucleation) and r_o (which will depend upon the position of the adsorbed atom in the surface) the values given above may not be regarded as accurate to better than ± 50%. Further, in view of the variation found in Mo for the different planes it does not appear to be justified to attempt to use Schmidts method for calculating relative binding energies by the use of equations (19) and (53).

It is interesting, however, that the largest value of Mo is for the (110) plane, for which there is the largest work function change, and that the smallest Mo value is for the (100) plane for which $\Delta\phi$ is the smallest.

Further, both the (100) and (110) curves show marked minima although nucleation (and hence field enhancement) is most noticeable on the higher index planes. These dips, in the absence of nucleation, may be accounted for by the higher effective polarizability values obtained for the (110) and (100)'s compared with the (113)'s.

It does not appear justifiable however, to draw further conclusions from these Mo and α determinations without an improved knowledge of the adsorbate distributions on the various planes, and after treatment at different temperatures.

9.6 Summary

The adsorption model suggested by the above results has already been described. Briefly, adsorption at 295°K occurs with the formation of microcrystallites on all planes except the (110), these being particularly predominant on the (112)'s. (This is discussed more fully in Chapter 10). The migration energy required is the kinetic energy of the incident atoms. Heating to above 934°K results in a change in the adsorbate structure on an atomic scale, no gross migration or rearrangement occurring. Heating above 1042°K is accompanied by a further change, and gross thermal rearrangement occurs at about 1100°K. The irreversible behaviour observed on heating a monolayer deposit through the phase transition temperatures is a property of the first two atomic layers, both uranium-uranium and uranium-tungsten interactions being involved. It has been shown that the observed behaviour is not due to hydrogen, oxide or tungsten contamination. It has further been shown that with increasing coverage, growth occurs preferentially on those crystal planes on which the bulk uranium structure can most easily be accommodated, and a model has been put forward suggesting the formation of alpha uranium (010) faces on the surface. It has further been shown that the work function decreases with increasing deposit thickness for the region $2 < \theta < 12$. This serves to explain the discrepencies in the previous determinations of the work function of uranium on tungsten.

On the next page is summarised the work function data obtained.

Work function (eV)

Plane		$T < 934^{\circ}K$	$934^{\circ}K < T < 1042^{\circ}K$	$T > 1042^{\circ}K$
Whole tip	minimum	3.37	3.31	3.19
	final	3.60	3.53	3.43
(110)	minimum	3.95	3.92	3.81
	final	4.04	3.99	4.00
(112)	minimum	3.19	3.35	3.20
	final	3.70	3.64	3.29
(100)	minimum	3.64	-	3.60
	final	3.88	3.61	3.82
(111)	minimum	3.17	2.89	2.83
	final	3.64	3.36	3.31
(113)	minimum	3.36	-	3.19
	final	3.60	-	3.53
(116)	minimum	3.31	-	3.28
	final	3.57	-	3.43

All values ± 0.03 eV.

TABLE 3

A comparison of the uranium results with those found for zirconium is given in Chapter 11.

CHAPTER 10

Results and Discussion - Zirconium

10.1 Introduction

As previously discussed the initial experiments on zirconium were essentially to determine whether irreversible behaviour, as observed with uranium occurred at the phase transition at 1135°K. This initial work was also intended to determine the variation of work function with coverage as the work function of zirconium was not well-established from previous measurements.

As described below, any phase transition work function changes were masked by the unusual nucleation and growth kinetics observed with zirconium. A study was therefore made of various aspects of the nucleation and growth processes. As with the uranium work, mass spectrometric measurements were also made, together with measurements on single crystal planes.

10.2 Total emission measurements

10.2.1 General

The emission tubes used during this work were of two designs. The first was the type C tube (Fig. 25) already described, with a Varian partial pressure gauge mounted near the evaporation source. The second design, shown in Fig, 49, did not incorporate a

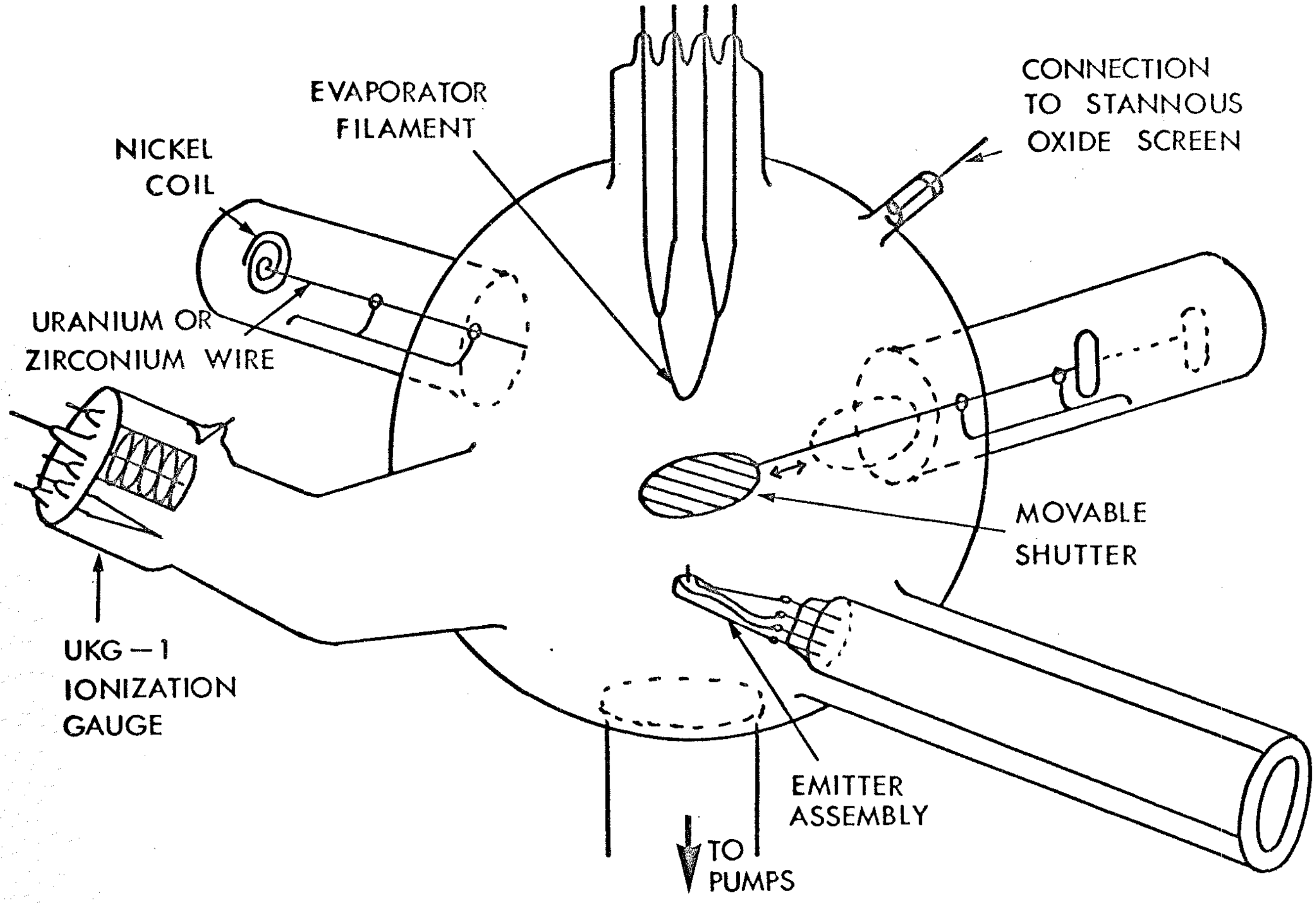

Fig. 49 Tube type D.
Evaporation is directly onto the end of the emitter but no phosphor screen is included.

phosphor screen but allowed evaporation directly onto the end of the emitter. The evaporation source was a tungsten filament mounted 5 cm away from the tip on two degassing loops. A movable tungsten shield screened the tip during outgassing of the source.

As in the uranium experiments work functions were determined by the use of equations (48) and (51). Work function against coverage was plotted at various stages during the outgassing of the source by successively depositing equal doses of zirconium onto the tip at 295°K and measuring the work function after each dose. It was found to be possible to keep the pressure during evaporation below 10^{-10} torr, even after only briefly outgassing the source. Therefore the differences in the clean and contaminated work function/coverage curves (Fig. 50 below) must primarily be due to the removal of contamination from the source rather than an improvement in the background pressure during the experiments. The source was assumed to be clean when reproducible plots were obtained for successive curves.

Migration and nucleation properties were observed by heating deposits of up to $1\frac{1}{2}$ monolayers to progressively higher temperatures for periods of 60 seconds.

10.2.2 Deposition of zirconium on tungsten at 295°K

Fig. 50 (A-C) shows how the work function/coverage curves at 295°K changed as the zirconium source was progressively

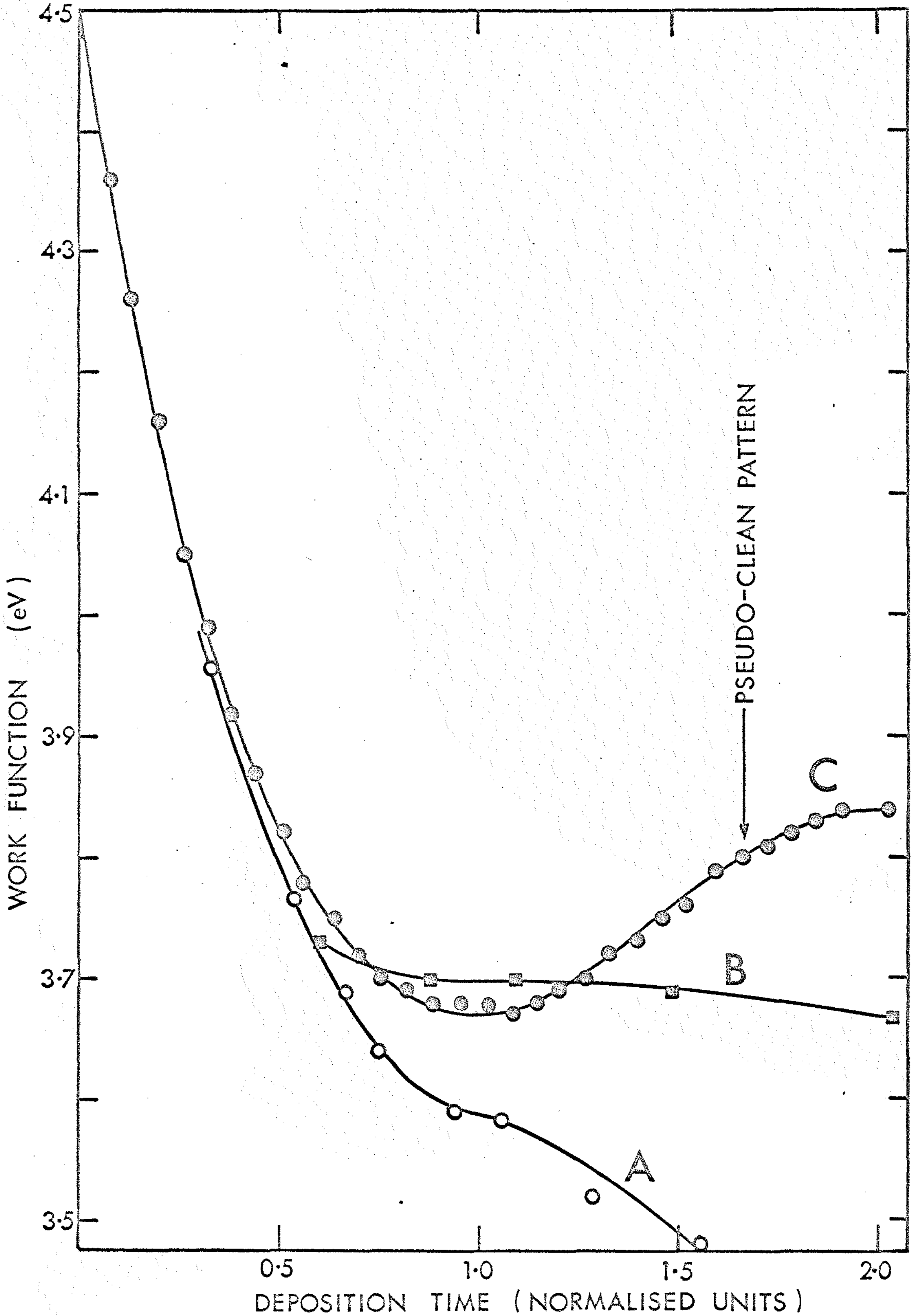

Fig. 50 Plots of work function against coverage for zirconium deposited at 295°K (A) from a briefly degassed source, (B) after further degassing and (C) for clean zirconium.

outgassed. Curve C was for clean zirconium. These curves are typical of the results from three experimental tubes. It is apparent that the work function drops more slowly in the case of contaminated deposits and then levels off followed by a further drop, whereas in the clean case the work function rises again to a final steady value of 3.84 ± 0.03 eV. This value compares well with the contact potential difference value of 3.87 ± 0.05 eV[119].

Fig. 51 shows the emission patterns observed at coverages of 0.56 and 1.0 (on the scale of Fig. 50) and after the work function has reached a steady value (coverage 2.0). It is seen that at low coverage the zirconium forms irregular clusters or microcrystallites[115] on all planes except the (110) , and in particular on the (211) planes, the patterns being identical with those for uranium (Fig. 27). The distributions at the minimum and final work function points are also similar to those for uranium on tungsten. The distribution at the point where the work function has risen to 3.8 eV shows the pseudo-clean tungsten pattern, and as in the uranium case, this is defined as the monolayer point.

The aggregates observed at low coverage at 295°K (Fig. 51A) are interpreted as randomly oriented nuclei similar to those of uranium on tungsten. That the (110) plane appears dark does not, of course, imply that it is free of zirconium, but that

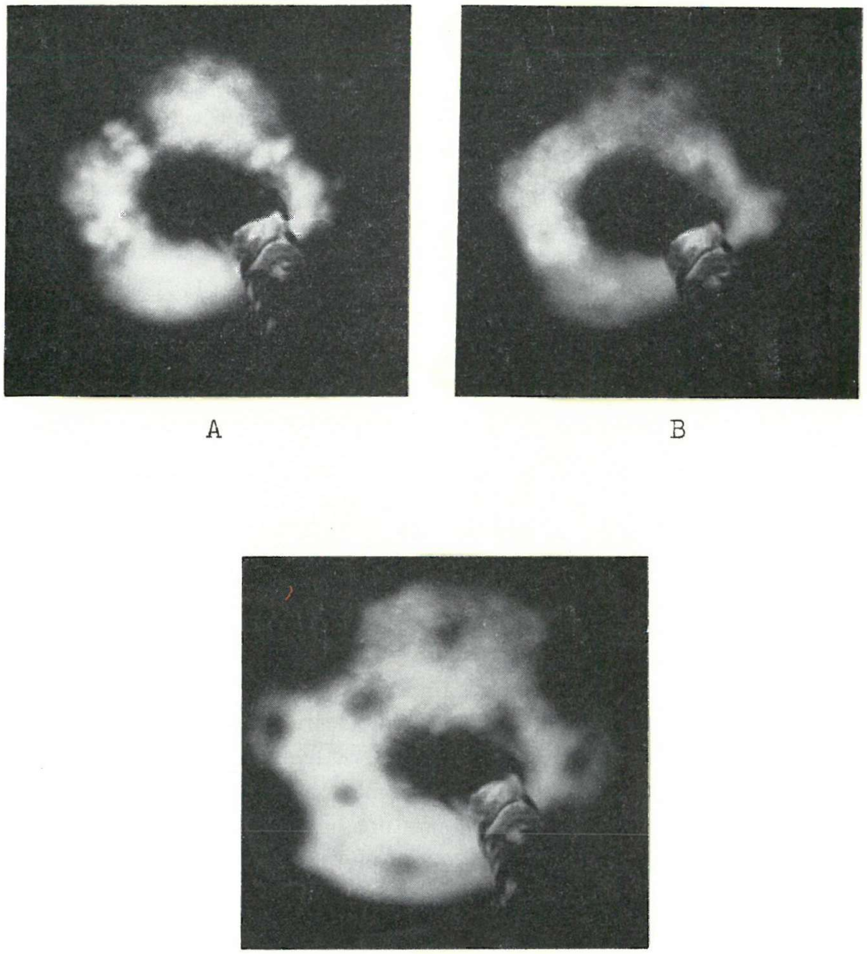

A

B

C

Fig. 51 Emission patterns for zirconium deposited on a tungsten field emitter at 295°K. (A) $\phi = 3.76$ eV, (B) $\phi = 3.67$ eV and (C) $\phi = 3.84$ eV.

if the zirconium is adsorbed, then the work function has not been significantly reduced; previous measurements however, indicate that electropositive adsorption on (110) planes yields the greatest work function change[156,157,230]. Alternatively, if nucleation has taken place then the nuclei are smaller than the minimum diameter (5.5 Å)[167] which would allow them to be seen as a result of local field enhancement. The third alternative is that the (110) planes are clean due to total surface diffusion of the adsorbed atoms from this plane. In the present experiments the greatest flux was incident upon the (110) plane in contrast with previous studies[94,235]; thus the observations cannot be due to lack of adsorbate on the (110) plane

Modern theories of nucleation[90,92,236] involve a surface migration mechanism of addition of atoms to the nuclei, and require sites of high binding energy to catalyse the nucleation process (Chapter 3). The (211) planes appear to present optimum conditions for nucleation at room temperature. For the bcc structure, these planes consist of rows of close packed atoms which will allow migration to occur fairly easily in one dimension along the valleys. If binding energies are higher for atomically rough planes (see Chapter 3) then the (112) structure presents sites of higher binding energy than may be found on the smooth (110) planes. Higher index planes would also, therefore, display much higher activation energies for migration. The experimental

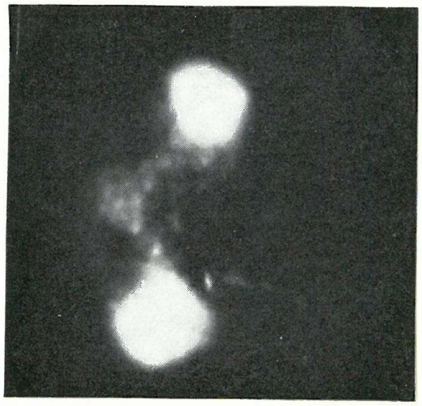

Fig. 52 Emission pattern of zirconium evaporated onto a tungsten field emitter from a briefly degassed source: $\phi=3.60$ eV.

observations of nucleation on the (211) regions appears to confirm this model. The effect of temperature on the initial nucleation is difficult to determine, since some account must be taken of the incident flux which exhibits the temperature of the evaporator (2050°K). As mentioned in Chapter 9, Melmed[110] has suggested that the energy of the incident flux contributes significantly to migration over the substrate surface.

Evaporation of zirconium from a source which had not been fully outgassed yielded work function values which were lower than for clean zirconium; these values increasing with increasing cleanliness of the evaporant. Fig. 52 shows the distribution after evaporation of 0.5 monolayers from a source which had been only briefly outgassed. The (111) regions appear very bright and there is a ring of adsorbate around the central (110) plane, probably indicating co-adsorption of contaminant with the zirconium.

10.2.3 Heat treatment of monolayer quantities of zirconium on tungsten

Zirconium evaporated onto tungsten was found to exhibit unusual migration properties dependent on the purity of the evaporant. Fig. 53 shows the variation of work function with annealing temperature for four deposits of zirconium, each of initially about $1\frac{1}{2}$ monolayers, at stages during the outgassing of the source. Curve D is typical of clean deposits of zirconium for which the corresponding emission patterns are shown in Fig. 54.

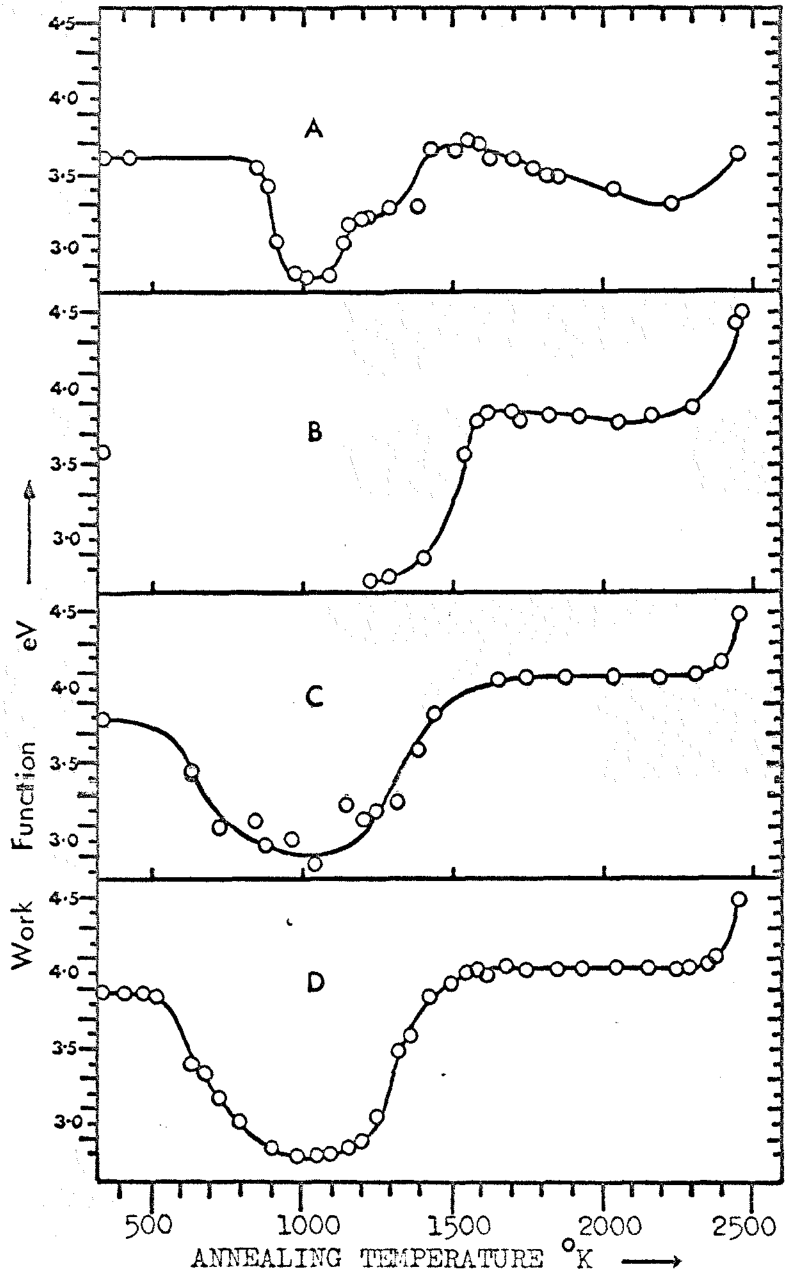

Fig. 53 Plots of work function against treatment temperature for four deposits of zirconium, each of initially about one monolayer, heated for periods of sixty seconds to progressively higher temperatures. The plots are for deposits from a source at various stages of degassing, curve D being typical of clean zirconium. The dip at 1000°K is associated with nucleation and coalescence of the deposit.

Fig. 54A shows the distribution at 300°K, the pattern appearing somewhat granular. In view of the nucleation observed at low coverages during deposition, it may be that the adsorbate in Fig. 54A exists in the form of nuclei, possibly with some coalescence, but these are not observable individually since the resolution of the field emission microscope is only about 20-30 Å. After heating to 450°K, Fig. 54B shows the onset of the formation of larger nuclei on the regions around the (110) and (100) planes. Further heating to 680°K results in the appearance of larger, well defined nuclei (Fig. 54C) which correspond to a sudden drop in the average work function of the emitter to 3.34 eV. These nuclei become larger and better defined (Fig. 54 D-G) and occur on all planes except the (110).

The nucleation growth process on heating in the range 500°K to 1000°K appears to be a consequence of the increased mobility of the zirconium atoms with increasing temperature. From their circular appearance and relative lack of radial growth it is concluded that they are three-dimensional. The work function reaches a minimum of 2.8 eV after heating to 1050°K, and from the emission pattern (Fig. 54G) the effective emitting area appears to have been reduced by a factor of about 20. If local increases in magnification are taken into account, this factor would be even larger. Substituting this ratio into equation (50) shows that the apparent work function of the

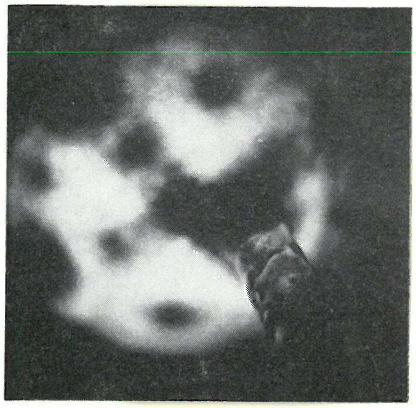

A

B

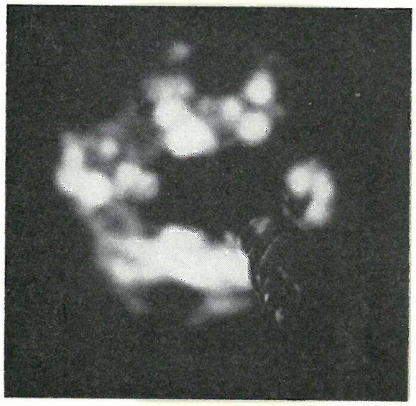

C

D

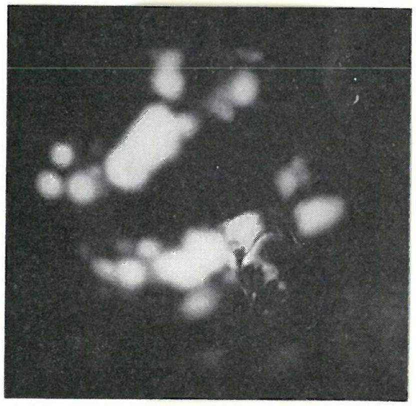

E

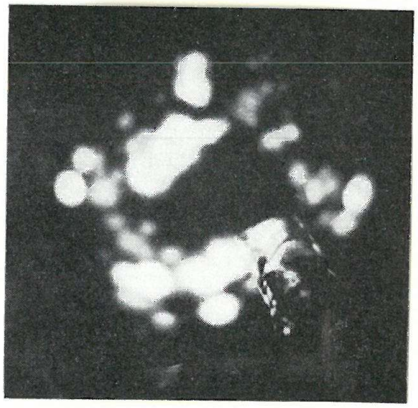

F

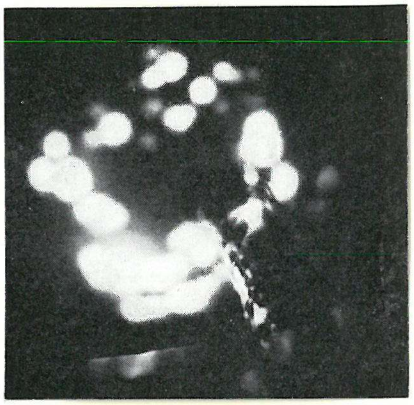

G

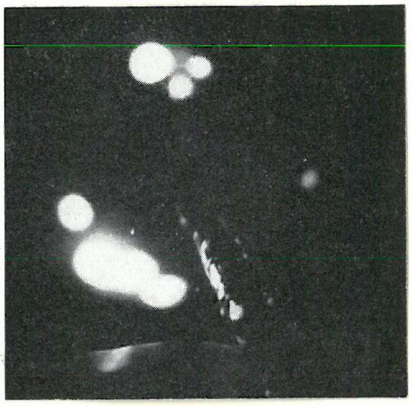

H

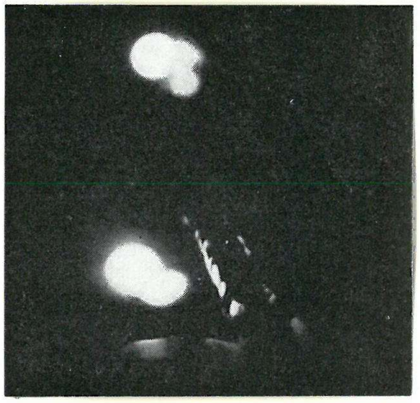

I

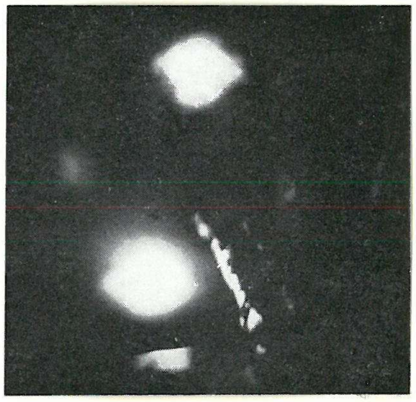

J

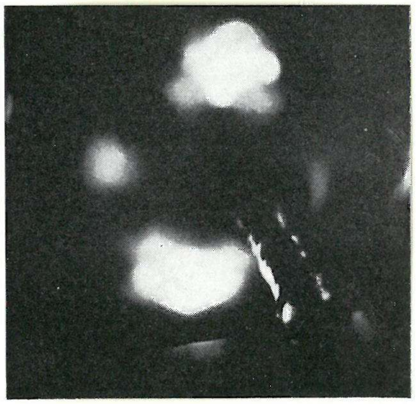

K

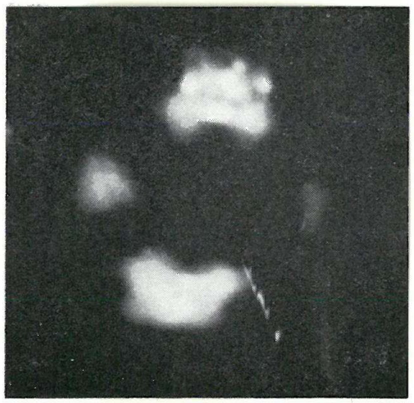

L

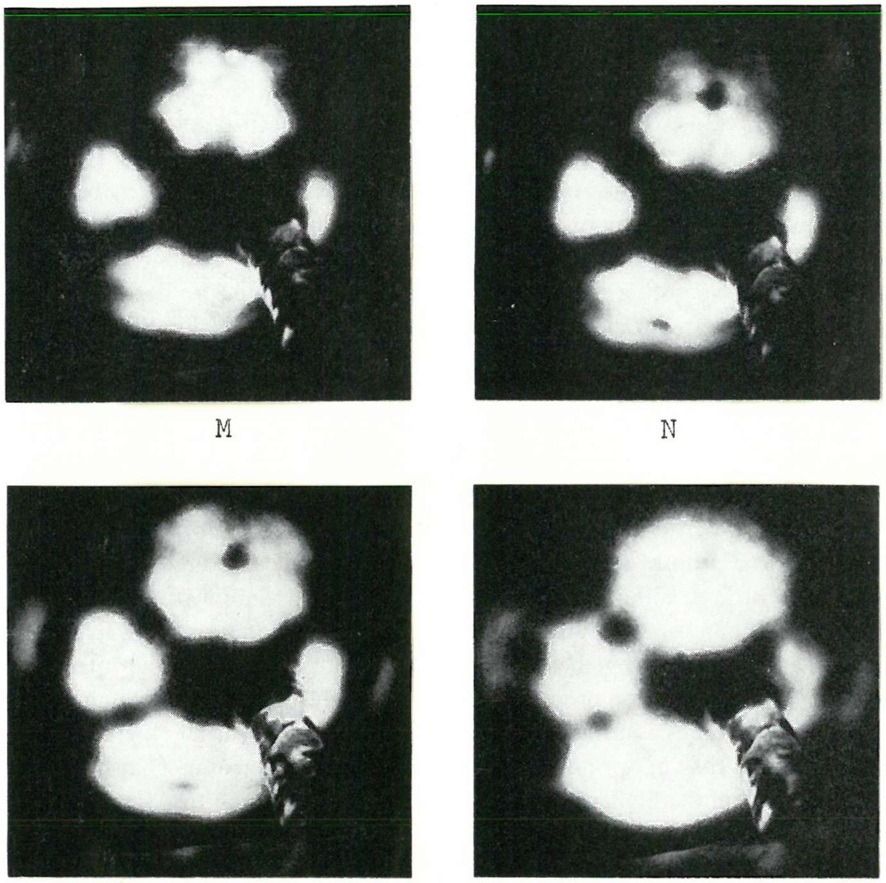

M N

O P

Fig. 54 Emission patterns of a monolayer deposit of zirconium heated for 60" periods at progressively higher temperatures. (A)295°K,Ø=3.84 eV;(B)460°K,Ø=3.84 eV;(C)615°K,Ø=3.39 eV;(D) 685°K,Ø=3.34 eV;(E)730°K,Ø=3.15 eV;(F)790°K,Ø=3.04 eV;(G)900°K Ø=2.83 eV;(H)1150°K,Ø=2.83 eV;(I)1200°K,Ø=2.89 eV;(J)1220°K, Ø=3.03 eV;(K)1260°K,Ø=3.49 eV;(L)1415°K,Ø=3.85 eV;(M)1445°K, Ø=3.92 eV;(N)1580°K,Ø=4.00 eV;(O)1800°K,Ø=4.04 eV;(P)2450°K, Ø=4.50 eV. All measurements were taken at 295°K.

emitter may be as low as 2.3 eV in the presence of these nuclei. Since three-dimensional nuclei would be expected to exhibit the work function of bulk zirconium, this anomalously low value is clearly a consequence of localised field enhancement[167]. Putting the expected values of work function into equation (50) shows a field enhancement factor of 1.5. This is half the factor predicted for hemispherical protrusions as calculated by Rose[167] and it is therefore concluded that the nuclei are cap-shaped.

The work function begins to rise after heating to 1150°K at which temperature there is an allotropic modification in the bulk metal from hexagonal close packed α-zirconium to body-centred cubic β-zirconium; the distribution of emission at this temperature is shown in Fig. 54H. After heating to 1190°K, Fig. 54I clearly shows that coagulation and bridging of the nuclei has occurred, only five distinct nuclei appearing on the cube faces, and further heating to 1250°K produces a smooth localised area of emission on the (100) planes, (Fig. 54J). Finally a 'double cross' is formed on the (100) vicinals; bright regions extending to the four (310) planes and less intense areas are observed on the (611) regions. Gretz[94] has noted that the (310) planes represent the boundary between the (100) plane and the (110) planes where the steps of (100) orientation cease to predominate. The emission pattern becomes more uniform, on heating further, as the zirconium begins to desorb (Fig. 53), but it is notable that there is some evidence of nuclei in the deposit (Fig. 54L), which become smoother as the final traces of zirconium are desorbed (Figs. 54M-O); the pattern for clean tungsten appears at 2450°K, Fig. 54P.

On the basis of these results, the following tentative model for the adsorption of zirconium on tungsten is proposed. For temperatures below 1135°K (the α-β transition), it is energetically favourable for the zirconium to form cap-shaped nuclei, presumably of the α-phase. Initially, on deposition at room temperature, this nucleation is most pronounced on the (211) planes (Fig. 51A), where the surface topography consists of rows of close packed atoms separated by about 1.62 atomic diameters[228]. The valleys between these rows clearly form sites of high binding energy, but since the zirconium (α) atom is 1.12 times larger than tungsten atoms, it is possible only for groups of five or so atoms to be adsorbed together along one valley. Therefore enough sites exist to catalyse the nucleation process and it is assumed that enough atoms can migrate over the surface to allow growth of the nuclei (there was no addition from the vapour phase during these measurements). That no nuclei are observed on the higher index planes may be attributed to a lower probability of migration over these planes[86]. As the deposit is heated to higher temperatures, the zirconium atoms become more mobile, forming nuclei on nearly all the higher index planes:

also the smaller nuclei appear to coalesce and bridge. The result is a number of large cap-shaped nuclei, possibly of the hcp bulk metal structure which presumably has a lower surface energy than the tungsten substrate.

After heating the substrate to above 1135°K, the nuclei appear to disperse and form a smooth continuous deposit on the (100) regions. The zirconium changes phase from α to β at this temperature, and this may account for the less favourable energy requirements for nuclei formation. The atomic diameter of β-zirconium is 3.22 Å [211] which is 2% too large to fit exactly in a square array on W (100); however a slight displacement towards the Zr (110) structure may occur (Fig. 55). This would permit registration with the substrate in one dimension, of similar structure to the Th-W (100) arrangement proposed by Anderson et al[237]. On cooling to the α-phase a close-packed square arrangement is possible (Fig.55) since the α-Zr atomic diameter is 3.16 Å which is exactly the lattice constant of tungsten, as noted by Shrednik[16]. It is concluded that such a smooth layer on the (100) may therefore exist below 1135°K but that the emission pattern would probably have been obscured by the enhanced field emission from the nuclei.

Emission patterns for insufficiently outgassed zirconium deposits are shown in Fig. 56. Previous studies have shown that contamination either enhances[238,239] or impedes[240,241]

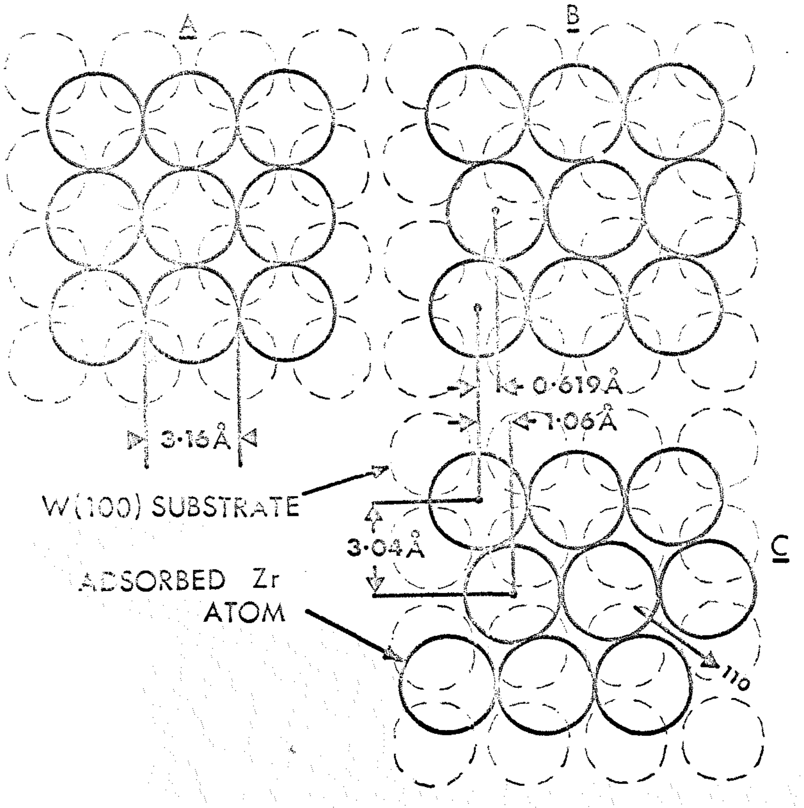

Fig. 55 Diagram of zirconium atoms adsorbed on a tungsten (100) plane; (A) alpha-zirconium (diameter 3.16 Å) in a close-packed square array; (B) beta-zirconium (diameter 3.22 Å) registered with the W(100) lattice in one direction; (C) the beta-zirconium (110) crystal face.

surface migration: the present measurements show a low nucleation rate which implies that migration is reduced. Heating to 1000°K produces little appreciable nucleation but a general migration to the atomically rougher planes around the (100), the work function falling to 2.8 eV. Fig. 56A shows the adsorbate distribution after heating to 1210°K, the work function having risen to 3.38 eV and Fig. 56B, after heating to 1350°K shows the formation of small circular clusters around the (100) planes and on the (111) vicinals, this being accompanied by a fall in the work function. The large nuclei formed with clean zirconium are not observed in the contaminated case, migration to the cube faces beginning (at 1520°K) before appreciable nucleus growth occurs. It is notable that higher temperatures are involved here than for the contaminant-free case suggesting that a major part of the adsorbed material may be zirconium dioxide. The ring structure on the (100) regions (Fig. 56D, 1780°K), previously noted by Shrednik[16] and by Fursei and Shakirova[117] were never observed with clean deposits.

For the contaminated deposits, a second dip in the work function versus temperature curve was observed at 2200°K, this dip becoming less pronounced as the source was progressively outgassed. This second dip may well be associated with oxide contamination since it is known that zirconium dioxide can be reduced by tungsten, the tungsten oxide either being desorbed or dissociating and the oxygen desorbed[242]. The emission patterns

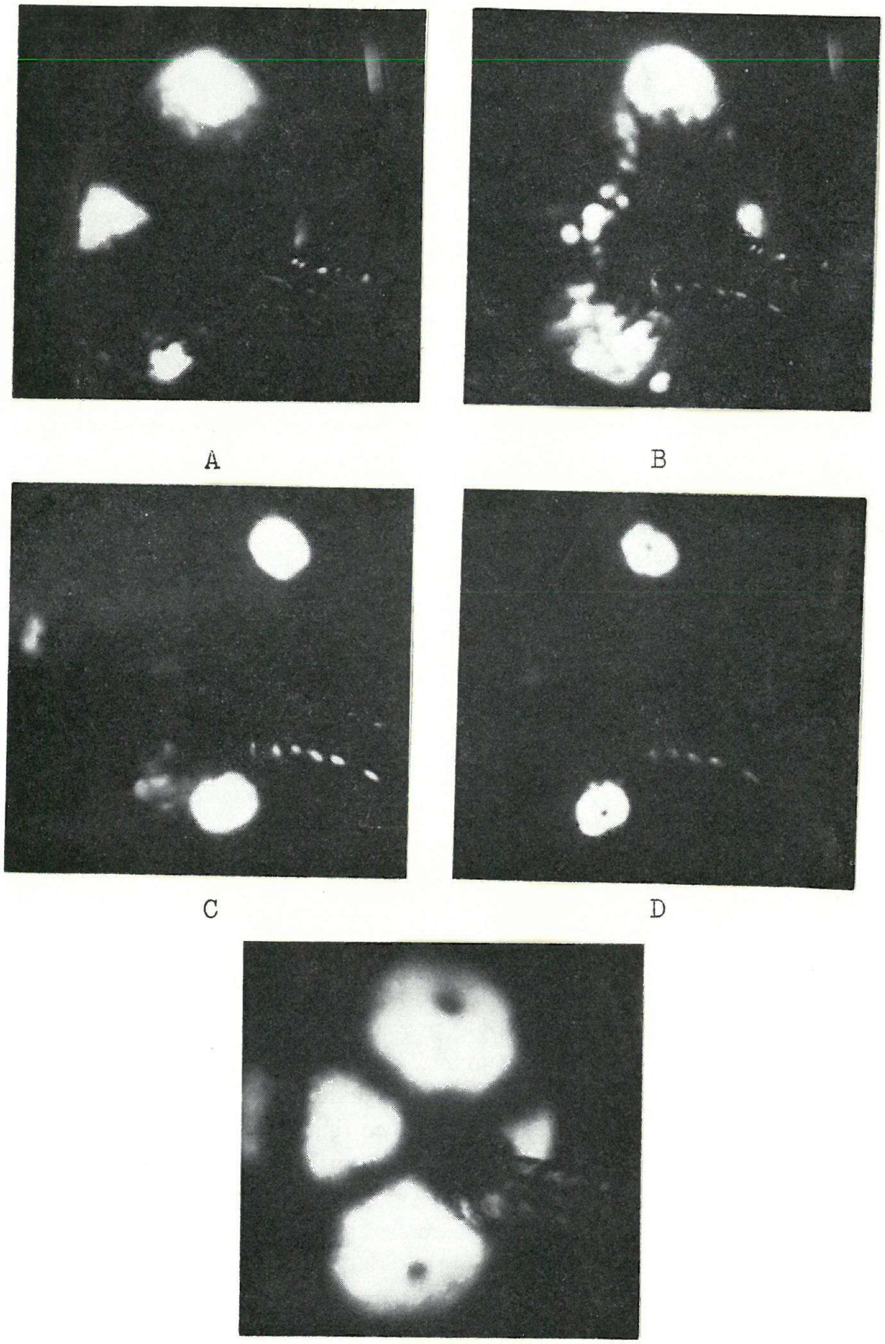

A

B

C

D

E

Fig . 56 Emission patterns of a contaminated monolayer deposit of zirconium heated for 60" periods to (A)1210°K,(B)1350°K,(C)1520°K,(D) 1800°K and (E) 2020°K.

above 2200°K are similar to those for clean deposits.

10.3 Mass spectrometric measurements

The residual gases present during all stages of experimentation with the type C tubes, were monitored with the Varian partial pressure gauge. Further measurements were made with the type E tubes (Fig 30) as with uranium to determine the vapour products of the source during outgassing and experimentation.

After bakeout and outgassing of all the metal parts of the tube, the residual gases were found to be H_2 and CO (30% each), CO_2 (10%), O_2 ($<$ 10%) together with H_2O and N_2, as shown in Fig. 57 (scan A). The zirconium was then melted onto the tungsten evaporator coil causing an initial pressure rise to 10^{-6} torr: Fig. 57 (scan B) shows the spectrum of gases evolved. Using the cracking patterns suppled by Varian Associates Ltd. the gases were identified as CH_4 (50%), H_2 (25%), H_2O (12%) and CO (10%) together with CO_2, SO_2 and N_2. This evolution of large quantities of methane has recently been observed by Jackson and Haas[243] for zirconium as well as for molybdenum, tantalum, titanium and niobium; they suggest this is due to the reaction of hydrogen with carbon diffusing from the bulk of the metal. After briefly degassing the zirconium (pressure reduced to 2×10^{-10} torr with the zirconium at 2100°K) the gases present during evaporation were as shown in Fig. 57 (scan C). After cooling the zirconium for one minute another scan was taken,

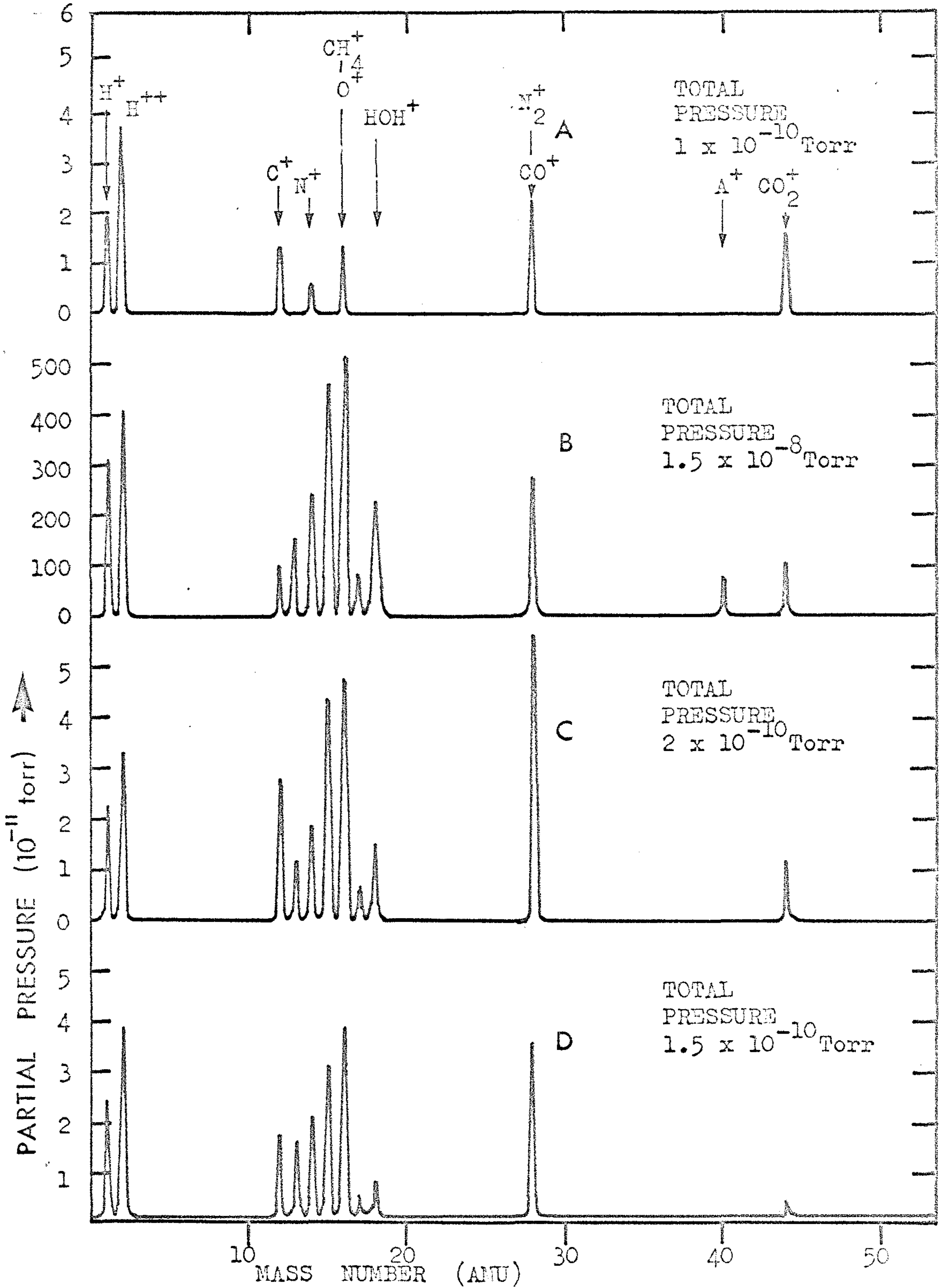

Fig.57 Mass spectra of the gaseous partial pressures (A) prior to melting on the zirconium,(B)immediately after melting on the zirconium,(C) during evaporation from a partially degassed zirconium source and (D) on cooling, one minute after scan (C).

and Fig. 57 (scan D) shows that the CO peak has fallen relative to the H_2 and CH_4 peaks, and that the CH_4 peak has fallen slightly relative to the H_2 peak. It therefore appears that the gases evolved on heating the zirconium after some outgassing are predominately CO, CH_4 and H_2 in that order. However, on cooling, the CO either pumps away or sorbs on the walls faster than either of the other two gases. Therefore the residual gas during the greater part of the experiments was H_2 with rather less CH_4, CO and H_2O. After complete outgassing of the zirconium, the pressure was reduced to below 10^{-10} torr even during evaporation and mass scans of sufficient sensitivity could not be obtained. The gases present, however, were assumed to be those in Fig. 57 (scan D).

In the subsidiary experiment to check the evaporant flux, the quadrupole mass spectrometer was mounted about 10 cm from the zirconium source. Fig. 58 (curve A) shows the effective partial pressure of clean tungsten as a function of the temperature of the fully outgassed clean evaporator loop. Fig. 58 (curve B) shows a similar plot for zirconium evaporated from the same loop. The evaporation source temperatures required to yield effective partial pressures of 10^{-8} torr (equivalent to deposition rates of about 0.005 monolayers per second) were $2040^{\circ}K$ for zirconium and $2750^{\circ}K$ for tungsten. At the usual evaporation temperatures (2000 to $2100^{\circ}K$) experiments were

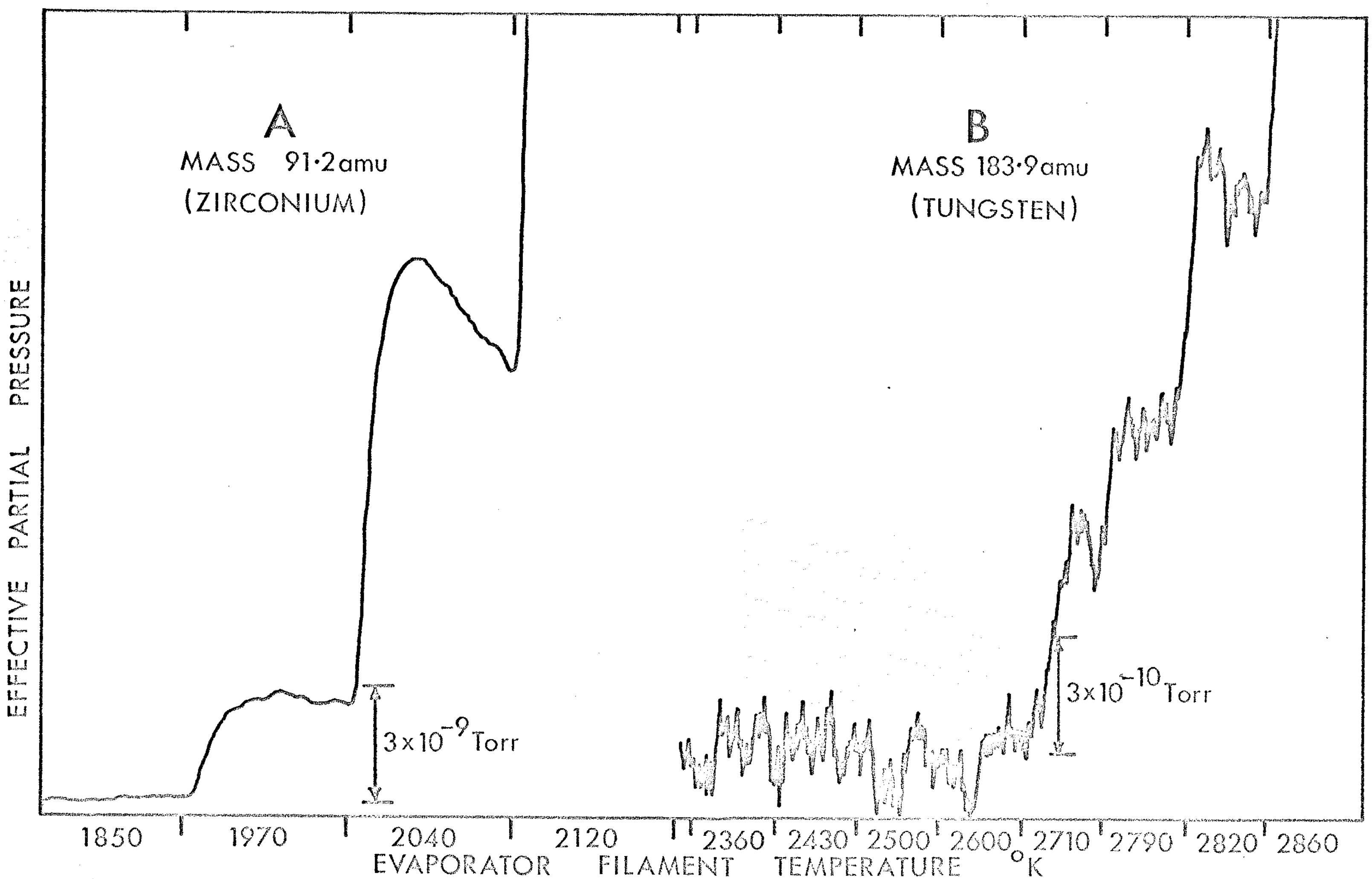

Fig. 58 Plots of effective partial pressures of tungsten evaporated from a tungsten filament and zirconium evaporated from the same filament as a function of filament temperature (measured pyrometrically).

often terminated by burning out of the source filament as also reported by Jackson and Haas[243]. To check that no tungsten vapour contributed to the zirconium flux, mass scans from 0 to 500 amu were recorded at the various evaporation temperatures. In no case was a tungsten peak observed in the mass scans, and it is therefore concluded that there was less than 1% of tungsten in the zirconium flux.

10.4 Measurements on single crystal planes

The experimental tube and techniques employed for the study of zirconium on the individual emitter planes were identical to those employed for the corresponding measurements on uranium.

The (110), (112), (100), (111) and (310) planes were studied, the clean (310) plane work function being taken as 4.31 eV.

The variation of work function with coverage for deposition of zirconium at 295°K was determined for these planes, typical plots being shown in Fig. 59. As in the uranium case (Figs 42-47), these curves show a number of interesting features, a number of these being common to both uranium and zirconium. The (112) plot shows a very pronounced dip, as in Fig. 42, associated with the formation of nuclei on this plane (Fig. 51). The (111) also shows a marked dip, as does the (310), but again (as for uranium) the (110) and (100) planes have only small dips in the curves. The most obvious difference between the uranium and

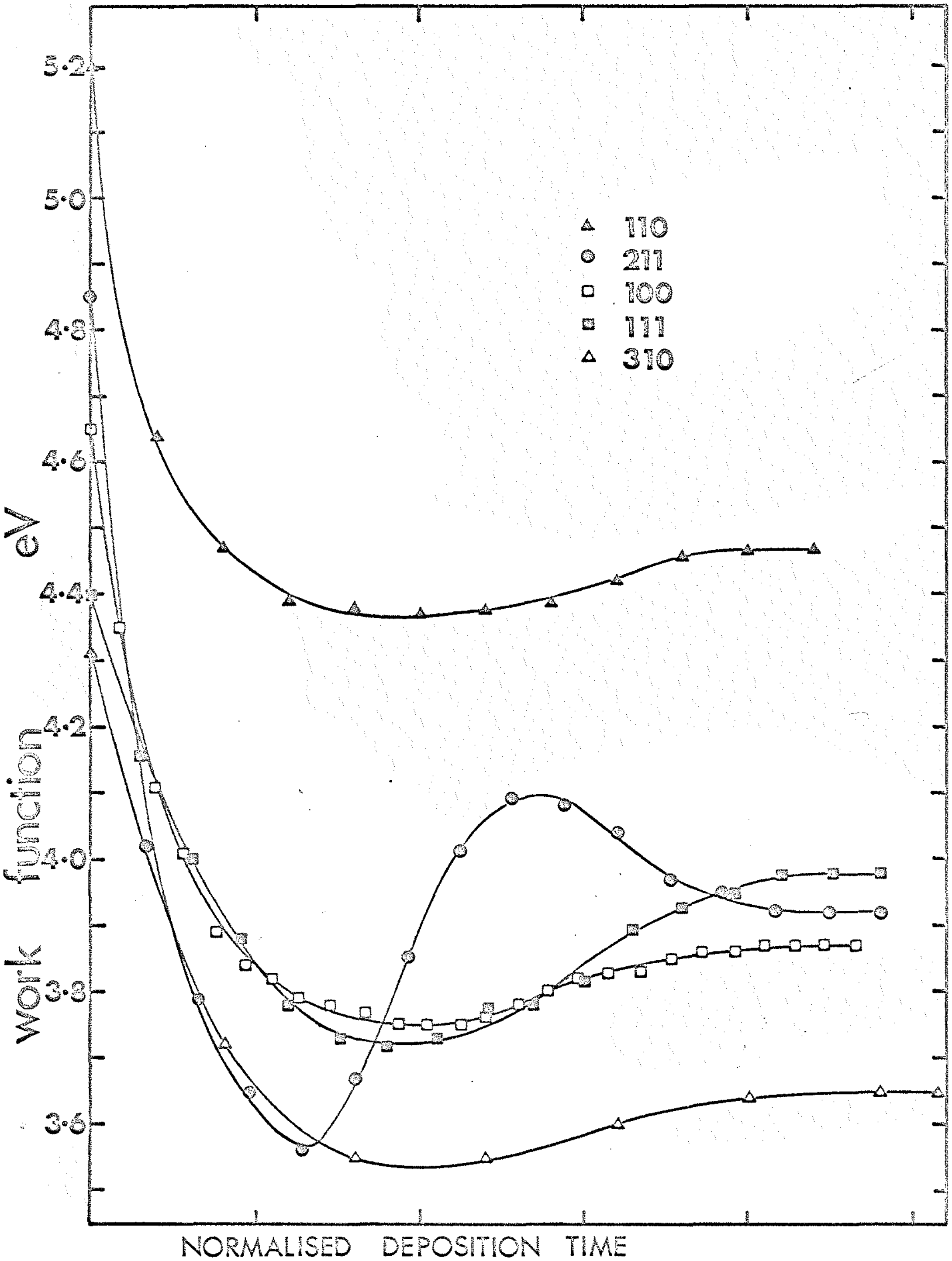

Fig. 59 Work function - coverage curves for zirconium deposited at 295°K on the (110),(211),(100),(111) and (310) planes.

zirconium curves is the peak in the (112) curve prior to levelling out. As a result of the statistical nature of the nucleus formation the curves obtained for the (112) plane showed variations of $\pm$ 100 mV in the values obtained, but the peak in the curve was consistently obtained. The reason for this peak is at present unclear.

Due to the nucleation, growth, coagulation and migration properties of zirconium when heated, plots of work function against heat treatment temperature did not give reproducible curves. However, the essential features of these plots were reproducible and yielded a certain amount of information. It was found that for measurements on the (100) plane, the work function fell noticeably in the temperature range 500-1000°K. This is the temperature range in which nucleation is occurring on all planes except the (110) and (100)'s (sec 10.2.3). The (100) plane appears dark in the emission patterns (Fig. 54) in this temperature range. However, that the work function falls suggests that growth is occurring on this plane, possibly by monolayer addition as according to the model suggested in sec. 10.2.3.

The (110) work function was also found to fall noticeably in the 500-1000°K temperature range. No changes were observed on the (110) plane in the emission patterns (Fig. 54) but the work function drop is explicable if nucleation or growth is occurring on this plane. If nuclei are forming then they would be smaller than the 5.5 Å diameter[167] above which they would be discernible in the patterns. However, it is more likely that growth by monolayer addition would occur on an atomically smooth plane such as the (110). Since an ideal packing arrangement such as on the (100)'s is not possible on the (110) the work function drop may be due to simple thermal rearrangement and partial growth.

On the higher index planes the heat treatment plots were unreproducible in the temperature range where nucleation and coagulation was occurring. In the range above 1500°K, where the deposit had smoothed, the curves were of the same form as the total emission curves in Fig. 53.

Dipole moment and effective polarizability determinations as described in sec. 9.5 may be made for the (100) plane. Assuming that the zirconium forms a close-packed square array as shown in Fig. 55, then the monolayer adsorbate atom density is $10 \times 10^{18} m^{-2}$. Following the procedure described in sec. 9.5 the initial slope of the (100) curve in Fig. 59 gives a value of $(Mo - \alpha F)_{100} = 8.9 \times 10^{-30}$ cb.m. Substituting this and the value of $\Delta\phi_{100}$ (1 monolayer) from Fig. 59 into equation (54) gives $\alpha_{100} = 19.6 \times 10^{-40}$ f.m.^{2}. Taking $F = -3.5 \times 10^9 v.m.^{-2}$ this gives $Mo_{100} = 2.1 \times 10^{-30}$ cb.m. Substituting in the expression $Mo = 2qr_o$ with $2r_o = 3.16$ Å gives $q < 0.1$ electron/atom.

As in the uranium case, the assumptions made in the calculations lead to possible errors of ± 50% in the Mo and α values.

10.5 Summary

The results described in this chapter are summarised below.

1. Zirconium deposited on tungsten at 295°K forms nuclei predominantly on the (211) planes. The work function falls to 3.67 ± 0.03 eV at about ½ monolayer coverage rising to a final steady value of 3.84 ± 0.03 eV. This is probably the work function of bulk zirconium.
2. Heating the deposits to 1050°K results in a drop in work function to 2.8 ± 0.1 eV associated with the formation of larger nuclei. Above 1050°K, the deposit smooths out, the emission being predominantly from the (100) planes, and the work function rises to 4.04 ± 0.03 eV.
3. In the temperature range 500-1000°K nucleation occurs predominantly on the high index planes.
4. The nuclei grow by diffusion and are cap-shaped.
5. The work function,diffusion and nucleation properties are strongly dependent upon the cleanliness of the evaporant.
6. Contamination impedes migration and nucleation.
7. Oxide contamination lowers the work function.
8. In the temperature range above 500°K growth on the (100)

planes occurs by monolayer addition.

9. The predominant gases evolved during degassing and evaporation of the zirconium are CO, CH_4 and H_2.

10. The evaporant flux from a source of the type used contains no oxide or tungsten contaminant after thorough outgassing.

Listed below are the minimum and final work function values obtained in the adsorption measurements.

	Work function (eV)	
Plane	Minimum	Final
Whole tip	3.67	3.84
(110)	4.37	4.46
(112)	3.56	3.92
(100)	3.75	3.87
(111)	3.72	3.88
(310)	3.55	3.65

Table 4

All values ± 0.03 eV.

A comparison of the uranium and zirconium results is given in Chapter 11.

CHAPTER 11

General Summary, Comparison of Results and Future Work

The results presented in the two previous chapters indicate that the adsorption properties of uranium and zirconium show marked similarities under certain conditions. In particular, at room temperature the emission patterns show identical adsorbate distributions for both metals. Nucleation occurs on the higher index planes, in particular on the (112)'s which appear to present the optimum surface topography for nucleation. Further, in the temperature range above 1500°K, where both adsorbates are completely mobile on the surface, growth is by monolayer addition with no preferred adsorption regions. Both metals show a strong dependence in their surface properties on the cleanliness of the deposit, oxide contamination tending to lower the work function and impede the adsorption kinetics.

In the temperature region 500-1500°K, the two metals show markedly different properties. Uranium becomes progressively more mobile with increasing temperature, but gross rearrangement does not occur below 1100°K. For this reason the variation in the work function clearly indicates the existence of irreversible changes at the phase transition temperatures. The mechanism of these changes is still not clear, but it has been established that they are not hydrogen, oxide or uranium-tungsten alloy contamination effects and further that they do not involve gross thermal rearrangement of the adsorbate. The irreversibility appears to be a consequence of the uranium-tungsten interactions in the first two monolayers. Above the phase transition temperature region the uranium deposit smooths out and thermal desorption begins at about 1500°K, the uranium being retained longest on the higher index planes.

The growth properties of zirconium are more complex. In the range 500-1000°K nucleation occurs on the higher index planes and growth by monolayer addition on the (100)'s. In the range 1000-1200°K coalescence and bridging of the nuclei occur accompanied by increased mobility of the zirconium. This results in further growth on the (100) regions at the expense of the nuclei, and above 1500°K the emission patterns resemble those for uranium.

No discontinuities were observed in the work function/heat treatment curves for zirconium at the phase transition temperature.

At no stage did heating result in the formation of large uranium nuclei comparable with those observed with zirconium. However, preferential growth regions were observed during multilayer adsorption of uranium.

A number of lines of research suggest themselves as suitable for future work on these adsorption systems. For uranium, electron diffraction studies of adsorption on the preferred growth planes (sec. 9.4) should yield information concerning the growth mechanisms, recrystallization and structural features of successively thicker deposits. Measurements on (112) and higher index **single** crystals may also yield information concerning the formation of nuclei at low coverage at room temperature, and during heat treatment may lead to a clearer understanding of the irreversible behaviour at the phase transitions. If these transitions involve rearrangement of individual atoms, then field-ion microscopy would be the appropriate technique for such a study. The experimental problems described in sec. 4.3 would, however, have to be overcome. Two further lines of research, using field emission, would firstly be to repeat the low-coverage uranium adsorption measurements using say, molybdenum of platinum field emitters in order to observe the effects of varying the substrate on the phase transition changes. Secondly, surface migration activation energy measurements for uranium or zirconium on tungsten, as described in sec. 3.2, would lead to an improved knowledge of the binding and surface kinetics on the various planes.

The most obvious research programme with zirconium would appear to be by the use of low-energy electron diffaction, to study both monolayer growth on the (100) surface, and nucleation on the higher index planes.

It is clearly apparent from the present work that the field emission microscope has the great advantage of allowing measurements to be made on a number of different single crystal planes simultaneously. However, the information which can be obtained from field emission measurements is strictly limited, particularly with regard to the structural features of the adsorbed layer. The ideal programme is therefore to use the emission microscope to make preliminary measurements and then, having determined the properties and crystal planes of interest, to use electron diffraction and field ion microscopy to study the structural features of the adsorbate-covered surfaces.

APPENDIX ONE

Effects of Hydrogen Contamination on the Work Function of Uranium on Tungsten

Discrepencies in the work function values of uranium on tungsten from different laboratories[6-10] have led to investigations on the adsorption of hydrogen on uranium-coated tungsten substrates. These investigations have arisen as hydrogen has been found to comprise the bulk of the residual gas in mercury-diffusion pumped systems in the 10^{-10} torr range and further, hydrogen is the predominant gas evolved during degassing and evaporation of uranium. The previously reported results, in both cases using the Zisman modification of the Kelvin contact potential technique, show negative surface potentials of -0.17 ± 0.05 volts (Hopkins and Sargood[208]) and -I.06 volts (maximum, Rivière[207]). Rivière has accounted for his unusually large value of the surface potential on the basis of the ionic nature of the U-H bond, other metal-hydrogen bonds being predominantly covalent and yielding surface potentials of less than 0.5 eV.

The difference in the two values above clearly warranted further investigation of the effects of hydrogen contamination and this was performed by the addition of a palladium diffusion leak attached to tube F (Fig. 33). An analysis of the gases diffusing through the palladium tube was made using the EAI 250 quadrupole residual gas analyser by mounting the diffusion leak on tube E (Fig. 30). A hydrogen purity of about 99.9% was observed after only briefly degassing the palladium tube, the main impurities being water vapour and carbon monoxide.

Measurements were performed by depositing up to 12 monolayers of uranium and leaking in hydrogen by heating the palladium tube in an atmosphere of 99.9% Ar or N_2 and 0.1% H_2. The leak rate could be controlled by the temperature of the palladium tube, leak rates of 10^{-9} torr l.sec^{-1} to 10^{-2} torr l.sec^{-1} being used. After leaking in hydrogen to maximum pressures of from 10^{-9} torr to as high as 10^{-3} torr (in about 10 seconds), the diffusion leak was immediately turned off and the pressure reduced to 1×10^{-10} torr (after about 12 hours of pumping from 10^{-3} torr). A number of measurements were made on the adsorption of hydrogen on clean tungsten field emitters, saturation work function values of the order of 5.2 eV being obtained, in reasonable agreement with the literature values[244-246].

The measurements of Rivière and of Hopkins and Sargood were performed under different experimental conditions. The latter used uranium deposits of only 2-3 monolayers thickness and hydrogen pressures not exceeding 10^{-5} torr, whereas Rivière used up to several hundred monolayers and pressures as high as 7 torr. Field emission microscopy is not suitable for deposition of thick (~100 monolayer) deposits, nor for measurements at pressures in excess of 10^{-7} torr so that the range of measurements taken was necessarily limited.

For deposits of 1 or 2 monolayers of uranium a maximum increase in work function of about 100 mV was observed after an exposure of 1L (1 Langmuir = 10^{-6} torr sec.). On leaving overnight during which time the pressure was reduced from 5×10^{-7} torr to 1×10^{-10} torr, the work function returned to the clean uranium value of 3.60 eV. A larger change became apparent with increasing uranium thickness, Fig. 60 A showing a plot for 8 monolayers of uranium. The maximum uranium coverage used in the present measurements was 12 monolayers, and the work function variation on adsorption of hydrogen is shown in Fig. 60 B. It is clearly seen that the work function rises initially, levelling out at 3.89 eV after a total exposure of about 3-4 L. This is followed by a slight fall in work function, followed by a further rise levelling out at 3.94 eV.

According to Rivière, hydrogen does not appear to penetrate the uranium surface in the same way as does oxygen[209] but forms ionic U-H bonds for the first monolayer, resulting in the intial increase in the work function. The curve levels out at about 3L, in agreement with Rivière who interprets this point as the completion of the first monolayer of hydrogen. The slight decrease in the work function in Fig. 60 B, which initially

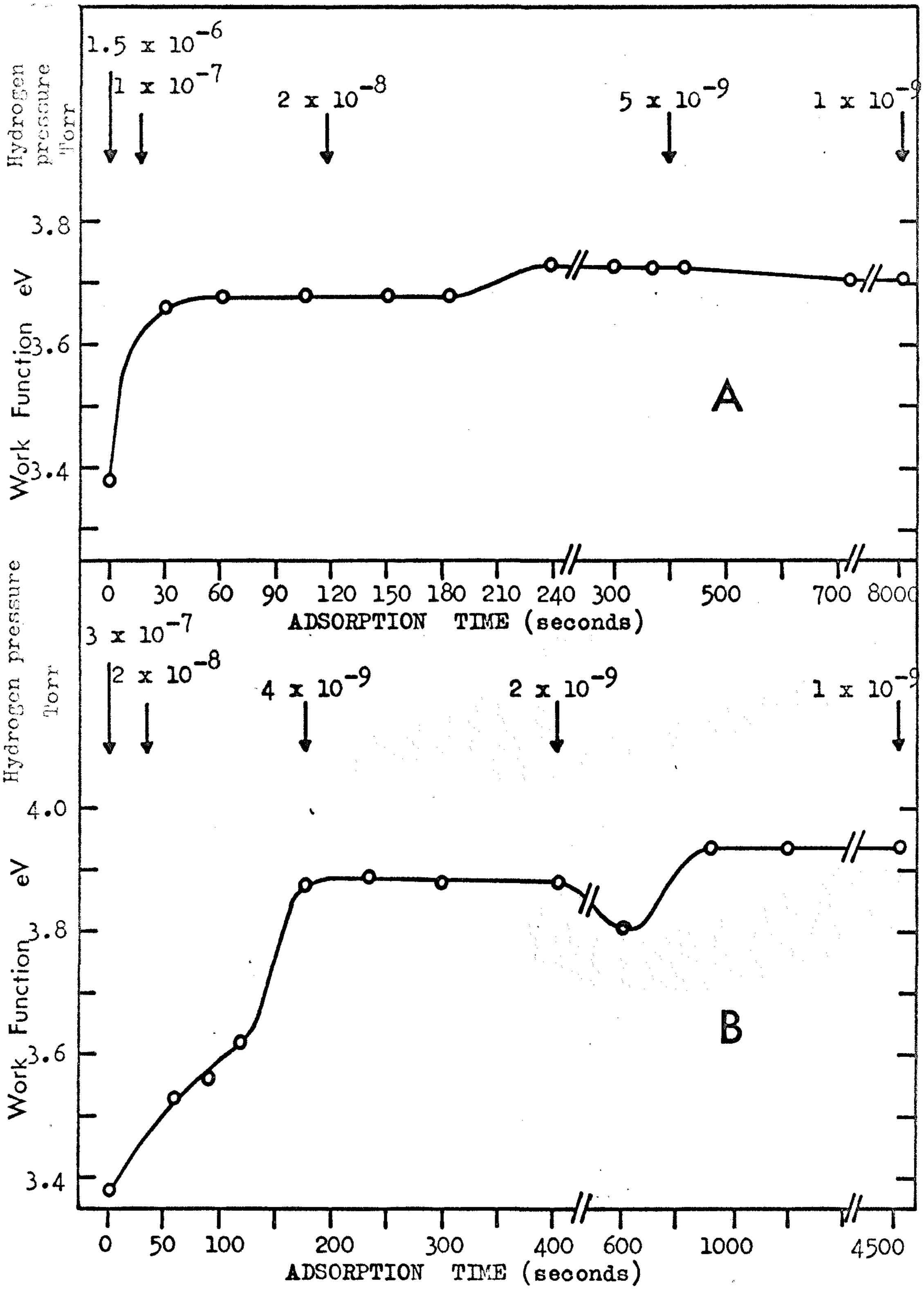

Fig. 60 Plots of average work function variation of uranium-coated field emitters on adsorption of hydrogen (A) for 8 monolayers of uranium and (B) for 12 monolayers.

appears at between 8 and 12 monolayers has also been observed by Riviere, but the reason for its existence is not clear. It is interesting to note that this thickness corresponds to the coverage at which Rauh and Thorn[6] found the thermionic work function of uranium on tungsten to reach a plateau. Further increase in the work function after this dip has been attributed by Rivière to hydride formation[184,247-249].

It is clear from the present results that the thickness of the uranium layer is critical in determining the surface potential and this could account for the differing values obtained by the previous workers. According to Rivière, penetration of the hydrogen into the uranium does not occur as the hydrogen atoms can find sites on the surface at which the degree of ionicity of the U-H bonds is optimized. As the surface structure of 1 or 2 monolayers of uranium on tungsten differs from the surface structure of bulk (or thick layers of) uranium, this condition may no longer apply with the resulting bonding being predominantly covalent. This may account for the smaller observed surface potential (~0.1 eV) at low coverage in the present work, and the value of -0.17 eV found by Hopkins and Sargood. Following the interpretation of the surface structure of uranium deposits of 2-7 monolayers thickness (sec. 9.4) as showing the development of the bulk uranium alpha structure, with a preponderance of (010) uranium faces in the surface, it would appear that there is a greater correspondence with the experimental conditions of Riviere at higher coverage. It is therefore expected that an adsorption process similar to that described by Rivière involving ionic bonding and subsequent hydride formation will occur as the coverage increases and the uranium surface tends toward the bulk metal structure.

It thus appears that the surface potential of hydrogen on uranium is dependent upon the thickness of the evaporated uranium layer, and that the structure of the uranium surface determines the state of binding of the hydrogen on the surface, ionic bonding and higher surface potentials occurring for uranium deposits of more than a few monolayers.

With regard to the uranium work function measurements described previously (Chapter 9) the effects of hydrogen contamination would appear to be negligible. For a typical work function/coverage plot, with the hydrogen partial pressure $\sim 10^{-10}$ torr, and the total time for the run being 2000 secs., the maximum exposure of the surface to hydrogen is 0.2 L, which, even at a coverage of 12 monolayers would not cause a work function increase of more than 30 mV (Fig. 60B). This is comparable with the experimental error, and in any event represents the greatest change in work function to be expected, the majority of experimental runs being performed at lower coverage and often in $<$ 1000 seconds.

It is concluded that hydrogen contamination had a negligible effect on the uranium work function values obtained in the present work, and further that hydrogen adsorption could not account for the descrepencies in the values obtained in this laboratory[9,10] and by Rivière[8] for the work function of uranium on tungsten.

APPENDIX TWO

Computer program for calculation of field emission work functions and Fowler-Nordheim preexponentials

Determination of Fowler-Nordheim parameters was made by means of 'least squares' fits programmed in ALGOL for an ICT 1907 computer. The same program (given below) also calculated the work functions defined by $\phi_2 = \phi_1(\frac{V_2}{V_1})^{\frac{2}{3}}$ using the same input data.

```
'PROGRAM' (P13AP13)

'BEGIN'

'REAL' SIGX, SIGY, SIGXY, SIGX2, SIGDEVY, M, C, SM, SC, K,CWF, SMSC,

SY, R, MC, PHI, FNPHI, RMSPHI;

'INTEGER' TOT, N, Z;

SELECT  OUTPUT (O);

WRITETEXT ('("('PC')' RICHARD%% COLLINS %%%% SURFACE %%% PHYSICS

%%%% P13'('4C')' FIELD %% EMISSION %% WORK %% FUNCTION %% AND %%

FOWLER-NORDHEIM %% PRE-EXPONENTIAL %% DETERMINATIONS '('8C')'

DATA % SET %%%%%%%% TOT * PHI %%%%% RMSPHI %%%% FNPHI %%%%

PREEXPONENTIAL %% SLOPE '('C')'

ERRORS:- %%%% SC %%% SM %%% SMSC %%% Y - DEVIATIONS ')');

NEWLINE (1);

N: = O;

SELECT INPUT (3);

START:  TOT: = READ;

CWF: = READ;
```

```
'BEGIN'

'ARRAY' X [1 : TOT], Y [1 : TOT], I[1 : TOT], V [1 : TOT],

VC [1 : TOT];

L1 : SIGX : = SIGY : = SIGXY : = SIGX2 : = 0;

K:= READ;

'FOR' Z : = 1 'STEP' 1 'UNTIL' TOT 'DO'

'BEGIN'

R: = READ;

'IF' R > 1000000 'THEN' 'GOTO' TERMINATE;

'IF' R > 50000 'THEN' 'GOTO' START;

'IF' R > 100 'THEN' V [Z] : = R 'ELSE'

'BEGIN'

I [Z] : = R; V [Z] : = READ;

'END';

X [Z] : = 10000 /V[Z];Y[Z]:= LN (0.00000001 * I [Z] /V [Z] ↑ 2);

SIGX : = SIGX + X [Z]  ;  SIGY : = SIGY + Y [Z]  ;

SIGXY : = SIGXY + X [Z] * Y [Z] ; SIGX2 : = SIGX2 + X[Z] ↑ 2;

'END';

M: = (TOT * SIGXY - SIGX * SIGY)/(TOT * SIGX2 - SIGX ↑ 2);

C: = (SIGY * SIGX2 - SIGXY * SIGX)/(TOT * SIGX2 - SIGX ↑ 2);

SIGDEVY : = 0;

'FOR' Z : = 1 'STEP' 1 'UNTIL' TOT 'DO'

SIGDEVY : = SIGDEVY + (Y[Z] - (M *X [Z] + C)) ↑ 2;

SY: = SQRT (SIGDEVY/(TOT - 2));

SC: = SY * SQRT (SIGX2/(TOT * SIGX2 - SIGX ↑ 2));
```

```
SM: = SY * SC * SQRT (TOT);
SMSC: = SY↑2 * (SIGX/(SIGX↑2 - TOT * SIGX2));
N: = N + 1;  PRINT (N, 5, 0) ; SPACE (1) ;
PHI: = FNPHI: = CWF;
'IF' K>1 'THEN' 'GOTO' L2 'ELSE' 'GOTO' L3;
L2: PRINT (PHI, 1, 3); SPACE (1);
PRINT (FNPHI, 1, 3);SPACE (1);
'GOTO' L4;
L3: RMSPHI: = 0;
'FOR' Z: = 1 'STEP' 1 'UNTIL' TOT 'DO'
'BEGIN'
PRINT (CWF * (V[Z] /VC [Z] ) ↑ (2/3), 1, 3); SPACE (1);
RMSPHI: = RMSPHI + (CWF * (V [Z] /VC [Z] )↑(2/3)) ↑ 2;
'END';
SPACE (3);
RMSPHI: = RMSPHI / TOT;
PRINT (SQRT (RMSPHI), 1, 3); SPACE (1);
PRINT (CWF * (M/MC) ↑ (2/3), 1,3); SPACE (1);
L4; PRINT (C, 1, 4); SPACE (1); PRINT (M, 1, 4);
NEWLINE (1);
PRINT (SC, 1, 4); SPACE (1);
PRINT (SM, 1, 4); SPACE (1);
PRINT (SMSC, 1,4); SPACE (1);
'FOR' Z: = 1 'STEP' 1 'UNTIL' TOT 'DO'
'BEGIN'
```

```
PRINT ((Y[Z] - (M * X[Z]  + C )) 1, 5); SPACE (1);
'END';
PRINT (SQRT (SIGDEVY), 1, 5);
NEWLINE (1);
'IF' K > 1 'THEN'' GOTO' TUNGSTEN VALUE 'ELSE'
'GOTO' L1;
TUNGSTEN VALUE:  MC: = M;
'FOR' Z: = 1 'STEP' 1 'UNTIL' TOT 'DO'
VC[Z] : = V [Z] ;
'GOTO' L1;
TERMINATE:  FREEINPUT; PAPERTHROW; FREEOUTPUT;
'END';
'END';
```

The program uses emission current (i)/voltage (V) data to determine the slopes and intercepts of Fowler-Nordheim plots of log i/V^2 / $\frac{10^4}{V}$ by means of least-squares fits. Fowler-Nordheim work functions (FNPHI) are determined by multiplying the $2/3$ power of the ratio of the slope (M) with the clean emitter slope (MC) by the clean work function (CWF). The work functions (PHI) defined by the equation $\phi_2 = \phi_1 \left(\frac{V_2}{V_1}\right)^{2/3}$ are calculated for each point on the Fowler-Nordheim plots, together with the rms average (RMSPHI) for the points on a given plot.

The program allows any clean work function value (CWF) to be assumed and any number (TOT) of points may be used for each

Fowler-Nordheim plot. For convenience, the program is written to accept voltages in volts and currents in units of 10^{-8} amps.

Data input is on cards and any number of data sets may be input provided that the machine store is not exceeded.

Data input is in the following form:-

FIRST NUMBER (TOT) : NUMBER OF POINTS ON EACH FOWLER-NORDHEIM PLOT
SECOND NUMBER (CWF) : CLEAN WORK FUNCTION VALUE
THIRD NUMBER (K) : EITHER 2 IF A CLEAN PLOT OR 1 IF NOT
FOURTH NUMBER (R) : FIRST CURRENT READING
FIFTH NUMBER (R) : CORRESPONDING VOLTAGE.

The computer now reads in current and voltage values up to a total of TOT i.e. the points for the first Fowler-Nordheim plot.

Subsequent data sets then require only the K value and the voltages (R) to be input as long as the values of CWF, TOT and the current values do not change. Provision is made for changing any of these values by inputting the appropriate R values, i.e. $1000000 > R > 50000$ allows a new TOT and/or CWF to be read in $R < 100$ indicates a new set of current values. The program is terminated by inputting a number > 1000000.

Data output is by line printer and gives the results on a two line print-out for each data set, in the following form.

FIRST LINE. Data set number, the TOT values of PHI, the r.m.s. average of these values (RMSPHI), the Fowler-Nordheim work function (FNPHI), the Fowler-Nordheim preexponential term (C) and the Fowler-

Nordheim slope (M).

SECOND LINE. This gives the standard deviations in the pre-exponential (SC), the slope (SM) and the co-variance (SMSC) followed by the y-deviations of the points on the Fowler-Nordheim x-y plot.

The computation time is approximately 0.1 seconds per data set of 10 points.

APPENDIX 3

A Direct Comparison of the Field Emission and Retarding Field Methods of Work Function Determination

It is apparent from section 5.2.2 that the field emission work function, whether defined by equation (48) or (51) is difficult to relate directly with work functions determined by other techniques. This is due to the experimental conditions associated with, and the assumptions inherent in the calculation of work function by the field emission technique. It is therefore desirable to make a direct comparison of the work functions derived from equations (48) and (51) with those determined by a 'macroscopic' method, on the same adsorbate/adsorbent system, and under identical experimental conditions as regards pressure, impurities, degassing and evaporation procedures. Only two previous comparisons of similar techniques have been made[125,250] in both cases comparing the vibrating capacitor (Kelvin) and retarding field (Anderson) methods of determining contact potential difference. In no cases have field emission measurements been included although contact potential analogs for field emission work function increases have been calculated by Gomer[251] for polar chemisorbates.

In order to determine the correspondence between field emission and 'macroscopic' work functions the zirconium adsorption measurements described in sec. 10.2 have been compared with similar measurements made in this laboratory[119] using the Anderson retarding field technique (sec. 4.2.2). The experimental conditions were identical for both sets of measurements wherever possible. The same batch of zirconium was used and the vacuum, degassing and evaporation techniques were identical.

The respective work function/coverage curves for deposition at 295°K are shown in Fig. 61, ϕ_A being the Anderson work function, ϕ^* the work function defined by equation (51) and ϕ_{FN} the work function defined by equation (48). Also shown is the variation of the log of the Fowler-Nordheim pre-exponential term (A) with coverage.

Three observations may be immediatly made from these results. Firstly, the excellent agreement between ϕ_A and ϕ^*, and fairly good agreement with ϕ_{FN} at θ (coverage) = 1. Secondly, the much larger dip in the field emission curves, and thirdly the increase in log A with coverage.

The agreement in the final values is not surprising in view of the generally good agreement obtained by comparing field emission and macroscopic values for various other adsorption systems found by other workers.

Few complete coverage curves have been published however, so little comparison can be obtained with other systems as regards the size of the dip obtained in the curves.

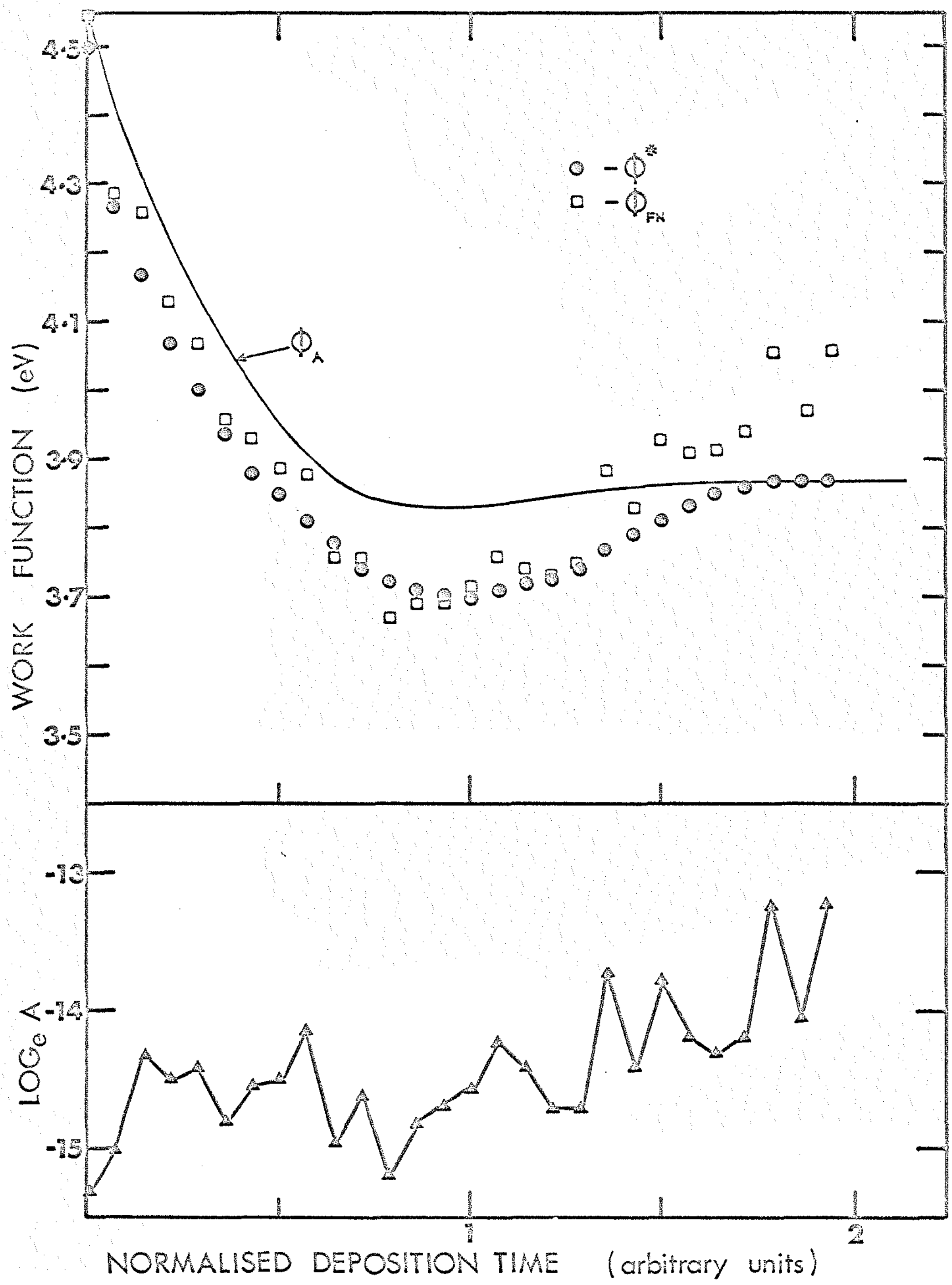

Fig. 61 Comparison of work functions calculated using the Anderson method and eqtns. 48 & 51 against coverage for Zr deposited at 295°K. Also shown is the variation of $\log_e A$.

It is found, however, that a larger dip occurs in the field emission curves for both U on W and Cs on W[2,252]. This dip is not explicable in terms of depolarization but could possibly be accounted for due to an increase in the effective emitting area at $\frac{1}{2}$ monolayer coverage. However, the variation of the pre-exponential term in Fig. 61 showing a gradual increase without a maximum does not seem to support this view.

The explanation in the case of the present system would appear to lie in consideration of the adsorption processes on the different crystal planes, and also on the distribution of these planes in the respective surfaces and on the weightings given to these planes in the calculation of the work function. The Anderson measurements were made on polycrystalline foil which X-ray diffraction measurements showed to be 95-100% (100) oriented with up to 5% (112) structure in the surface. The emission tips showed all the usual planes but whereas the Anderson work function measures an area average value, the field emission work function is strongly weighted towards the highly emitting planes. Observations of the emission patterns at low ($<\frac{1}{2}$ monolayer) zirconium coverage (Fig. 50) show field enhanced emission from aggregates predominantly on the (112) planes, these aggregates disappearing from the emission patterns at monolayer coverage. As already discussed, this field enhanced emission current results in an apparent reduction in the average emitter work function at $\frac{1}{2}$ monolayer coverage. In the case of the predominantly (100) oriented polycrystalline foil however, this apparent lowering of the work function will not occur and the effect will not be observed.

Confirmation of the above reasoning is supplied by comparison of the present uranium adsorption curve for deposition at 295°K on the (110) plane (Fig. 43) with the equivalent Anderson curve[231]. Nuclei are not observed on the (110) plane in the field emission patterns (Fig. 27) and by the above reasoning a large dip would not be expected in the field emission curve. In fact both the Anderson and field emission curves show a dip ($\phi_{final} - \phi_{minimum}$) of 0.10 eV, the curves being of almost identical shape.

In the case of caesium adsorption a slightly larger dip in the field emission curves has been obtained[252,253] but the emission patterns show no field enhancement due to nucleation as in the zirconium and uranium cases. However, the emission patterns[253] do show considerable variations in the regions from which the predominant emission occurs. In particular, the (110) regions become brightly emitting at about $\frac{1}{2}$ monolayer coverage, and several workers have shown that the (110) planes undergo the greatest decrease in work function (reaching a minimum of 1.5 eV) in this region. At monolayer coverage, the emission anisotropy is again similar to that for the clean emitter. It thus seems that the variation in emission anisotropy is responsible for the larger dip in the field emission curve.

To summarise, it would appear that variations in the regions which contribute predominantly to the total emission during the adsorption process result in anomalies in the work functions measured by field emission techniques. These anomalies appear primarily for the partially covered substrates. At monolayer coverage most adsorbates have been found to exhibit so-called pseudo-clean patterns closely resembling the emission pattern for the clean substrate. Under these conditions the requirement that there should be no change in the emission anisotropy is obeyed, and the field emission work functions agree closely with those determined by other methods.

The gradual increase in the Fowler-Nordheim pre-exponential term during zirconium adsorption accounts for the deviation of ϕ_{FN} from the other curves at higher coverage. What is surprising is the excellent agreement between ϕ_A and ϕ^* since the equation defining ϕ^* assumes that there is no change in the Fowler-Nordheim pre-exponential.

It can only be concluded therefore, that ϕ^* as defined by equation (51) bears more correspondence with the macroscopic work function than does ϕ_{FN}.

REFERENCES

1 J.H.De Boer 'Electron Emission and Adsorption Phenomena'
(Cambridge University Press) 1935

2 T.J.Lee Ph.D. Thesis, University of Southampton, 1967

3 I.Langmuir Phys.Rev. 22 (1923) 357

4 G.A.Haas and J.T.Jensen J.Appl.Phys. 31 (1960) 1231

5 G.A.Haas and J.T.Jensen J.Appl.Phys. 34 (1963) 3451

6 E.G.Rauh and R.J.Thorn J.Chem.Phys. 31 (1960) 1481

7 R.K.Fry and A.B.Cardwell Phys.Rev. 125 (1962) 471

8 J.C.Rivière Proc.Phys.Soc. 80 (1962) 116

9 D.E.Barry,B.J.Hopkins and A.J.Sargood Surf.Sci. 7 (1967) 365

10 C.Lea and C.H.B.Mee Surf. Sci. 8 (1967) 417

11 W.E.Danforth and A.J.Williams J.Appl.Phys. 32 (1961) 1181

12 H.C.Rentschler,D.E.Henry and K.O.Smith
Rev. Sci. Instrum. 3 (1932) 794

13 C.Zwikker Physik Z. 30 (1929) 578

14 D.A.Wright Proc.Inst.Elec.Engrs.(London) 100 Pt3 (1953) 125

15 V.N.Shrednik Sov.Phys.Solid State 1 (1959) 1037

16 V.N.Shrednik Sov.Phys.Solid State 3 (1961) 1268

17 H.H.Lester Phil.Mag. 31 (1916) 197

18 J.C.Rivière A.E.R.E. Report 5526 (1968)

19 B.J.Hopkins and J.C.Rivière Proc.Phys.Soc. 81 (1963) 590

20 C.Herring and M.H.Nichols Rev.Mod.Phys. 21 (1949) 185

21 N.Cusack 'The Electrical and Magnetic Properties of Matter'
(Longmans) 1960

22 R.H.Fowler and E.A.Guggenheim 'Statistical Thermodynamics'
(Cambridge University Press) 1939

23 E.W.Muller Physik Z. 37 (1936) 838;Z.tech.Physik 17 (1936)
412;Z.Physik 102 (1936) 734,106 (1937) 132,541

24 S.T.Martin Phys.Rev. 56 (1939) 947

25 R.Smoluchowski Phys.Rev. 60 (1941) 661

26 M.H.Nichols Phys.Rev. 57 (1940) 297

27 I.Langmuir Trans.Am.Electrochem.Soc. 29 (1916) 125

28 F.Rother and H.Bomke Zeits.f.Physik 86 (1933) 231

29 C.G.Bedreag Comptes Rendus 223 (1946) 354
30 J.F.Chittum J.Phys.Chem. 38 (1934) 79
31 E.H.B.Bartelink Physica 3 (1936) 193
32 H.B.Michaelson J.Appl.Phys. 21 (1950) 536
33 G.Hermann and S.Wagener 'The Oxide-Coated Cathode' vol 2
(Chapman and Hall, London) 1951
34 W.M.H.Sachtler Z.Electrochem 59 (1955) 119
35 W.Gordy and W.J.Thomas J.Chem.Phys. 24 (1956) 439
36 J.H.O.Varley Phil.Mag. 5 (1960) 64
37 E.Wigner and J.Bardeen Phys.Rev. 48 (1935) 84
38 J.Bardeen Phys.Rev. 49 (1936) 653
39 H.J.Juretschke Phys.Rev. 92 (1953) 1140
40 T.L.Loucks and P.H.Cutler J.Chem.Phys.Solids 25 (1964) 105
41 J.Bardeen Surf.Sci. 2 (1964) 381
42 J.Ziman Adv.in Phys. 13 (1964) 89
43 W.J.Leivo,M.D.Bell,W.F.Wei and C.Northrop
U.S.Air Force Report AFCRL-65-489
44 F.Seitz 'Modern Theory of Solids'
(McGraw-Hill Inc. N.Y. 1940)
45 M.Kaminsky 'Atomic and Ionic Impact Phenomena'
(Springer-Verlag, Berlin) 1965
46 S.Brunauer,P.H.Emmett and E.Teller J.Am.Chem.Soc. 60 (1938)309
47 L.Pauling 'The Nature of the Chemical Bond'
(Cornell University Press) 1960
48 R.W.Gurney Phys.Rev. 47 (1956) 479
49 J.W.Gadzuk Surf.Sci. 6 (1967) 133
50 R.F.Culver and F.C.Tompkins Adv. in Catalysis 11 (1959) 67
51 J.A.Becker Phys.Rev. 34 (1929) 1323
52 I.Langmuir and J.Taylor Phys.Rev. 44 (1933) 423
53 W.Brittain and J.Becker Phys.Rev. 43 (1933) 428
54 R.C.L.Bosworth Proc.Camb.Phil.Soc. 33 (1937) 394
55 A.R.Miller Camb.Philos.Soc. 42 (1946) 292
56 J.Topping Proc.Roy.Soc.(London)A114 (1927) 67
57 M.Boudart J.Am.Chem.Soc. 74 (1952) 3556

58 J.J.Broeder,L.L.van Reijen,W.M.H.Sachtler and G.G.A.Schmit Z.Electrochem.Ber.Bunsenges Physik Chem.60(1956)838

59 R.S.Mulliken J.Chem.Phys. 2 (1934) 782

60 I.Higuchi,T.Ree and H.Eyring J.Am.Chem.Soc. 79 (1957) 1330

61 E.P.Gyftopoulos and J.D.Levine J.Appl.Phys. 33 (1962) 67

62 J.G.Malone J.Chem.Phys. 1 (1933) 197

63 J.Eisinger J.Chem.Phys. 27 (1957) 1206

64 J.Eisinger J.Chem.Phys. 28 (1958) 165

65 J.Eisinger J.Chem.Phys. 29 (1958) 1154

66 J.Eisinger J.Chem.Phys. 30 (1959) 412

67 A.D.Crowell and A.L.Norberg J.Chem.Phys. 37 (1962) 714

68 N.S.Rasor and C.Warner J.Appl.Phys. 35 (1964) 2589

69 J.R.MacDonald and C.A.Barlow J.Chem.Phys. 44 (1966) 202 and Surf.Sci. 4 (1966) 381

70 L.D.Schmidt and R.Gomer J.Chem.Phys. 42 (1965) 3573

71 J.P.Jones Proc.Roy.Soc.(London) A284 (1965) 469

72 R.Gomer and L.W.Swanson J.Chem.Phys. 38 (1963) 1613

73 L.D.Schmidt and R.Gomer J.Chem.Phys. 45 (1966) 1605

74 F.Ashworth Adv. in Electronics 3 (1951) 1

75 R.Gomer,R.Wortman and R.Lundy J.Chem.Phys. 26 (1957) 1147

76 R.Gomer and K.Hulm J.Chem.Phys. 27 (1957) 1363

77 G.Ehrlich and F.G.Hudda J.Chem.Phys. 30 (1959) 493

78 L.W.Swanson,R.W.Strayer and L.E.Davis Surf.Sci. 9 (1968) 165

79 A.J.Melmed J.Chem.Phys. 43 (1965) 3057

80 R.Gomer 'Field Emission and Field Ionization'(O.U.P.) 1961

81 G.Ehrlich Brit.J.Appl.Phys. 15 (1964) 349

82 G.Ehrlich and F.G.Hudda J.Chem.Phys. 44 (1966) 1039

83 M.Drechsler Z.Electrochem. 58 (1954) 327

84 S.Takami and T.Kuroda Jap.J.Appl.Phys. 7 (1968) 180

85 T.N.Rhodin unpublished

86 H.E.Neustadter and R.J.Bacigalupi Surf.Sci. 6 (1967) 246

87 T.N.Rhodin and D.Walton in 'Metal Surfaces' Am.Soc. for Metals (Ohio, U.S.A.) 1962 p.259

88 T.N.Rhodin in:'The Use of Thin Films in Physical Investigations'Ed.J.C.Anderson (Academic Press) 1966 p.187

89 J.H.Hollomon and D.Turnbull in'Progress in Metal Physics'p.333 (Pergamon Press, Oxford) 1953

90 J.P.Hirth and G.M.Pound 'Condensation and Evaporation, Nucleation and Growth Kinetics' in 'Progress in Materials Science' vol.2(MacMillan,N.Y. 1963) p41

91 N.Cabrera Disc.Faraday Soc. 28 (1959) 16

92 D.Walton J.Chem.Phys. 37 (1962) 2182

93 D.Walton,T.N.Rhodin and R.Rollins J.Chem.Phys. 38(1963) 2695

94 R.D.Gretz J.Phys.Chem.Solids 27 (1966) 1849

95 R.D.Gretz Surf.Sci. 6 (1967) 468

96 R.D.Gretz and G.M.Pound App.Phys.Letts. 11 (1967) 67

97 R.D.Gretz Surf.Sci. 5 (1966) 261

98 R.D.Gretz Surf.Sci. 4 (1966) 494

99 R.D.Gretz Surf.Sci. 5 (1966) 239

100 R.D.Gretz Surf.Sci. 5 (1966) 255

101 A.J.Melmed and S.C.Hardy Surf.Sci. 6 (1967) 481

102 D.W.Pashley Adv. in Physics 14 (1965) 327

103 G.A.Bassett,J.W.Menter and D.W.Pashley Symposium on Structure and Properties of Thin Films (J.Wiley N.Y. 1959) p 11

104 K.M.Greenland J.Sci.Instrum. 38 (1961) 1

105 G.A.Bassett Phil.Mag. 3 (1958) 1042

106 G.A.Bassett and D.W.Pashley J.Inst.Metals 4 (1959) 449

107 K.L.Moazed and G.M.Pound Final Report on Contract no.AF 18 (600)-1572 WashingtonA.F.Office of Scientific Research(59)

108 M.J.Duell and R.L.Moss Brit.J.Appl.Phys. 15 (1964) 157

109 R.D.Gretz Phys.Stat.Sol. 23 (1967) 453

110 A.J.Melmed J.Appl.Phys. 36 (1965) 3585

111 A.J.Melmed J.Appl.Phys. 37 (1966) 275

112 E.B.Hensley J.Appl.Phys. 32 (1961) 301

113 W.L.Hole and R.W.Wright Phys.Rev. 56 (1939) 785

114 R.H.Fowler Phys.Rev. 38 (1931) 45

115 R.H.Good Jr. and E.W.Muller in:Handbuch der Physik vol 21 (Springer Verlag,Berlin 1956) p 176

116 E.W.Muller Mod.Res.Techn.Phys.Metallurgy (Amer.Soc.for Metals,Ohio 1953) p 33

117 G.N.Fursei and S.A.Shakirova Sov.Phys.Tech.Phys. 11 (1966) 827

118 T.N.Rhodin private communication

119 A.J.Sargood and D.E.Barry private communication

120 B.H.Blott to be published

121 T.Delchar,A.Eberhagen and F.C.Tompkins J.Sci.Instrum. 40 (1963) 105

122 C.W.Oatley Proc.Roy.Soc.(London) A115 (1936) 218

123 H.Shelton Phys.Rev. 107 (1957) 1553

124 P.A.Anderson Phys.Rev. 47 (1935) 958

125 B.J.Hopkins and B.J.Smith J.Appl.Phys. 39 (1968) 213

126 O.W.Richardson and F.S.Robertson Phil.Mag. 43 (1922) 162

127 I.Langmuir and K.H.Kingdon Phys.Rev. 21 (1923) 380

128 E.Ya.Zandberg and N.I.Ionov Sov.Phys.Uspekhi 67 (1959) 255

129 J.R.Werning 'Thermal Ionization at Hot Surfaces' Thesis UCRL-8455 (1958)

130 I.N.Bakulina and N.I.Ionov Sov.Phys.JETP 9 (1959) 709

131 G.R.Hertel J.Chem.Phys. 47 (1967) 133 and 335

132 J.W.May Industrial and Engineering Chemistry 57 (1965) 19

133 A.J.Melmed,H.P.Layer and J.Kruger Surf.Sci, 9 (1968) 476

134 N.J.Taylor Surf.Sci. 4 (1966) 161

135 E.W.Muller Adv.Elect.Elec.Phys. 13 (1960) 83

136 E.W.Muller,J.A.Panitz and S.B.McLane Rev.Sci.Instrum. 39 (1968) 83

137 E.W.Muller,S.Nakamura,O.Nishikawa and S.B.McLane J.Appl.Phys. 36 (1965) 2496 and refs.therein

138 E.W.Muller Surf.Sci. 2 (1964) 484

139 D.G.Brandon Brit.J.Appl.Phys. 14 (1963) 474

140 E.W.Muller Science 149 (1965) 591

141 J.L.Boling and W.W.Dolan J.Appl.Phys. 29 (1958) 556

142 R.W.Kiser 'Introduction to Mass Spectrometry' (Prentice Hall, N.J. 1965)

143 J.Yarwood and K.J.Close Brit.J.Appl.Phys. 16 (1965) 335

144 R.W.Wood Phys.Rev. 5 (1897) 1

145 W.Schottky Z.Physik 14 (1923) 63

146 B.S.Gossling Phil.Mag. 1 (1926) 609

147 R.H.Fowler and L.Nordheim Proc.Roy.Soc.(London) A119 (1928) 173

148 L.Nordheim Proc.Roy.Soc.(London) A121 (1928) 626 and R.E.Burgess,H.Kroemer and J.M.Houston Phys.Rev. 90 (1953) 515

149 A.G.J.van Oostrom Philips Res.Rep.Suppl. no.1 (1966)

150 F.I.Itskovich Sov.Phys.JETP 23 (1966) 945

151 see,for example V.Rojansky 'Introductory Quantum Mechanics' (Prentice Hall, N.Y. 1938)

152 J.W.Little,T.E.Madey and R.Klein J.Appl.Phys. 36 (1965) 1491

153 N.A.Gorbaty and I.I.Gofman Radiotekhn.i.Elektron 8 (1963) 1927

154 R.Klein J.Chem.Phys. 21 (1953) 1177

155 K.Noga J.Phys.Soc.Japan 17 (1962) 950

156 A.P.Ovchinnikov and B.M.Tsarev Sov.Phys.Solid State 8 (1966) 1187

157 V.I.Makukha Sov.Phys.Solid State 9 (1967) 111

158 L.D.Schmidt J.Chem.Phys. 46 (1967) 3830

159 V.A.Kuznetsov and B.M.Tsarev Sov.Phys.Solid State 9 (1968) 1987

160 V.B.Voronin Sov.Phys.Solid State 9 (1968) 1758

161 G.Ehrlich and F.G.Hudda J.Chem.Phys. 35 (1961) 1421

162 C.B.Duke and M.E.Alferieff J.Chem.Phys. 46 (1967) 923

163 W.Ermrich and A.van Oostrom Solid State Comms. 5 (1967) 471

164 P.H.Cutler and D.Nagy Surf.Sci. 3 (1964) 71

165 R.Nowicki Surf.Sci. 8 (1967) 357

166 R.P.Johnson and W.Shockley Phys.Rev. 49 (1936) 436

167 D.J.Rose J.Appl.Phys. 27 (1956) 215

168 Y.Yashiro 8th Field Emission Symposium,Williamstown 1961

169 A.J.Melmed Surf.Sci. 8 (1967) 191

170 J.E.Fasth,B.Loberg and H.Norden J.Sci.Instrum. 44 (1967) 1044

171 W.P.Dyke,J.K.Trolan,W.W.Dolan and G.Barnes J.Appl.Phys. 24 (1953) 570

172 J.P.Barbour,F.M.Charbonnier,W.W.Dolan,W.P.Dyke,E.E.Martin and J.K.Trolan Phys,Rev. 117 (1960) 1452

173 J.L.Boling and W.W.Dolan J.Appl.Phys. 29 (1958) 556

174 E.W.Muller Z.Physik 108 (1938) 668

175 E.W.Muller Z.Physik 106 (1937) 132

176 A.J.Melmed and E.W.Muller J.Chem.Phys. 29 (1958) 1037 and references therein

177 R.Gomer J.Chem.Phys. 28 (1958) 458

178 A.J.Melmed and R.Gomer J.Chem.Phys. 30 (1959) 586

179 W.P.Dyke and W.W.Dolan Adv.Elect.Elec.Phys. 8 (1956) 89

180 R.Gomer and K.Hulm J.Chem.Phys. 27 (1957) 1363

181 P.C.Bettler and G.Barnes Surf.Sci. 10 (1968) 165

182 L.Marton and R.A.Schrack ref. 80 p. 63

183 A.J.Melmed App.Phys.Letts. 12 (1968) 100

184 J.J.Katz and E.Rabinowitch 'The Chemistry of Uranium' (Dover Pub.Inc. N.Y. 1951)

185 Analysis by Electronic Space Products Inc.,Los Angeles,Calif.

186 A.N.Holden 'Physical Metallurgy of Uranium' p 27 (Addison Wesley 1958)

187 J.H.Gittus 'Uranium' in:Metallurgy of The Rarer Metals (Butterworths 1963)

188 P.Duwez J.Appl.Phys. 24 (1953) 152

189 C.W.Jacob and B.E.Warren J.Am.Chem.Soc. 59 (1937) 2588

190 C.W.Tucker Trans.Am.Soc.Metals 42 (1950) 762

191 J.Friedel J.Phys.Chem.Solids 1 (1956) 175

192 C.W.Tucker and P.Senio Acta.Cryst. 5 (1952) 753

193 J.Thewlis and H.Steeple Acta.Cryst. 7 (1954) 323

194 H.H.Klepfer and P.Chiotti USAEC Rep. ISC-893(Iowa State College 1957)

195 C.H.Schramm,P.Gordon and A.R.Kaufmann Trans.Amer.Inst.Min. Met.Eng. 188 (1950) 195

196 D.Summers-Smith J.Inst.Metals 83 (1955) 383
197 S.Dushman Phys.Rev. 21 (1923) 623
198 O.Klein and E.Lange Z.Electrochem. 44 (1938) 542
199 W.L.Hole and R.W.Wright Phys.Rev. 56 (1939) 785
200 E.W.Muller ref. 116 p.
201 E.W.Muller private communication
202 L.D.Kolomiets Sov.Phys.Crystallography 12 (1967) 132
203 S.N.Chatterjee Acta.Cryst. 11 (1958) 679
204 J.Donohue Acta.Cryst. 14 (1961) 327
205 Yu.S.Vedula,V.M.Gavrilyuk and V.K.Medvedev Sov.Phys Solid State 4 (1963) 1870
206 Ya.P.Zingerman,V.A.Ischuk and V.A.Morozovskii Sov.Phys.Solid State 3 (1961) 760
207 J.C.Rivière Suppl. al Nuovo Cimento 5 (1967) 466
208 B.J.Hopkins and A.J.Sargood Suppl. al Nuovo Cimento 5 (1967) 459
209 J.C.Rivière Brit.J.Appl.Phys. 15 (1964) 1341
210 R.J.Ackermann,E.G.Rauh and R.J.Thorn J.Chem.Phys. 37 (1962) 2693
211 G.L.Miller 'Zirconium' in:Metallurgy of The Rarer Metals (Butterworths, London 1957) p 18
212 W.Espe 'Zirkonium' C.F.Winter'sche Verlaghandslung,Bayern(53)
213 J.Cauchoix and J.Lavarde Sem.Hop.Paris 26 (1950) 1335
214 R.F.Domagala,D.J.McPherson and M.Hansen J.Metals N.Y. 5 (1953) 73
215 A.J.Sargood private communication
216 V.I.Vedenyev,L.V.Gurvich,V.N.Kondrat'yev,V.K.Medvedev and Ye.L.Frankevich 'Bond Energies,Ionization Potentials and Electron Affinities' p 152 (Edward Arnold Ltd.,London 1966)
217 Bell's Asbestos and Engineering Ltd.,Slough,Bucks.
218 B.J.Hopkins Contemp.Phys. 9 (1968) 115 and refs.therein
219 J.H.Singleton and W.J.Lange J.Vac.Sci.Technol. 2 (1965) 93
220 P.H.Dawson and N.R.Whetton J.Vac.Sci.Technol. 4 (1967) 382

221 Resolution:Two peaks of equal height are said to be resolved when the valley between them is 10% of the height of either peak,e.g.the resolution is said to be 100 if the valley between two peaks corresponding to isotopic masses 100 and 101 is 10% of the peak height of either.

222 G.K.White and S.B.Woods Can.J.Phys. 35 (1957) 663

223 M.Drechsler and E.Henkel Z.angew Phys. 6 (1954) 341

224 H.M.Montagu-Pollock and T.N.Rhodin J.Sci.Inst. 43 (1967)667

225 F.C.Frank and J.H.van der Merwe Proc.Roy.Soc.(London)
A198 (1949) 205

226 U.Gradmann Phys.kondens Materie 3 (1964) 91

227 J.H.van der Merwe in'Basic Problems in Thin Film Physics'
(Vandenhoeck and Ruprecht,Gottingen 1966) p 122

228 J.F.Nicholas 'An Atlas of Models of Crystal Structures'
(Gordon and Breach, N.Y. 1965)

229 C.Lea private communication

230 V.M.Gavrilyuk and V.K.Medvedev Sov.Phys.Solid State
8 (1966) 1439

231 A.J.Sargood private communication

232 L.D.Schmidt and R.Gomer J.Chem.Phys. 45 (1966) 1605

233 J.R.MacDonald and C.A.Barlow J.Chem.Phys. 40 (1964) 412

234 C.Lea Ph.D. thesis (University of Southampton 1968)

235 R.D.Gretz and G.M.Pound in 'Condensation and Evaporation
of Solids'p 575 (Gordon and Breach N.Y. 1964)

236 J.P.Hirth Ann.N.Y.Acad.Sci. 101 (1963) 805

237 J.Anderson,P.J.Estrup and W.E.Danforth App.Phys.Letts.
7 (1965) 122

238 E.W.Muller Z.Physik 126 (1949) 642

239 S.S.Brenner 10th Field Emission Symposium,Berea,Ohio, 1963

240 A.J.Melmed J.Appl.Phys. 37 (1966) 275

241 L.D.Schmidt and R.Gomer J.Chem.Phys. 43 (1965) 95

242 J.Anderson and W.E.Danforth J.Franklin Inst. 279 (1965) 160

243 A.G.Jackson and T.W.Haas J.Vac.Sci.Technol. 4 (1967) 42

244 R.Gomer and R.Wortman J.Chem.Phys. 23 (1955) 1741

245 J.A.Becker Solid State Phys. 7 (1958) 379

246 B.J.Hopkins and K.R.Pender Surf,Sci. 5 (1966) 316

247 G.G.Libowitz and T.R.P.Gibb J.Phys.Chem. 60 (1956) 510

248 G.G.Libowitz J.Nucl.Mater. 2 (1960) 1

249 T.R.P.Gibb and D.P.Schumacher J.Phys.Chem. 64 (1960) 1407

250 P.A.Anderson Phys.Rev. 88 (1952) 655

251 R.Gomer J.Chem.Phys. 21 (1953) 1869

252 L.W.Swanson,R.W.Strayer and F.M.Charbonnier Surf.Sci. 2 (1964) 177

253 L.W.Swanson and R.W.Strayer J.Chem.Phys. 48 (1968) 2421

ACKNOWLEDGEMENTS

The author would like to take this opportunity to thank Dr.B.H.Blott for his advice and encouragement throughout the course of this work.

The author also wishes to thank the following:

Professors G.W.Hutchinson,E.W.Lee and A.M.Taylor for providing laboratory facilities.

The Science Research Council for provision of a maintenance grant.

The members of the Surface Physics group of the University of Southampton for much general assistance and useful discussions,in particular Drs.B.J.Hopkins,T.J.Lee and B.J.Smith.

A.J.Sargood for permission to reproduce his results prior to publication.

Mr.J.Lawrensen for assistance with the glassblowing.

Miss Rosalyn James for typing this thesis.